UNIVERSITÀ DEGLI STUDI DI PADOVA

Dipartimento di Fisica e Astronomia "Galileo Galilei"

Master Degree in Astrophysics and Cosmology

Final dissertation

Unraveling the SMBH and its Nuclear Environment in NVSS J163547+362930 in the Early Universe

Thesis supervisor
Prof. Eugenio Bottacini

Candidate
Jose Maria Sanchez Zaballa

Thesis co-supervisor
Dr. Andrea Tramacere

Academic Year 2022/23

How long will I love you?
As long as quasars are above you,
And longer if I can...
A mi bro, Majo

Abstract

While there is a general consensus that active galactic nuclei (AGN) derive their power from a supermassive black hole (SMBH) accreting matter, the precise origins and evolution of these SMBHs in the first billion years after the Big Bang remain unclear. Detecting AGNs in this early cosmic epoch is challenged by their weak emission due to their remote distances. However, Blazars, a specific subset of AGN, exhibit an exceptional and fluctuating jet pointing towards us, detectable from radio frequencies to $\gamma-$ray energies, making them invaluable tools for understanding the evolution of SMBHs and their host galaxies. One of these very rare sources, NVSS J163547+362930, at redshift $z = 3.65$, allows us to study its emission processes, describing the physical mechanisms at work, and characterising its SMBH in the early universe. Using the particle propagation software `JetSeT`, employing a standard Shakura-Sunyaev disc (SSD), and assuming an initial particle distribution, we performed spectral energy distribution (SED) modelling, probing the effects of varying the black hole spin, ranging from non-rotating Schwarzschild black holes to the extreme Kerr variety. We found that a moderately spinning SMBH with a mass of $M_{BH} \sim 10^9 M_\odot$ governs the physics of the jet and that it likely evolved from a heavy seed. In the attempt of a consistency check, we verified the intrinsic correlation between the jet power and the accretion luminosity, in which the former appears to be weaker than the latter for high accretion efficiencies. Additionally, we properly related the $\gamma-$ray emissions to external Comptonization processes related to a seed of photons in a dusty torus (DT) rather than a broad-line region (BLR). Finally, using the best-fit SED model, we find a consistent lower limit for the redshift of the source employing the Lyman α drop-out technique in a novel approach.

Contents

Abstract **i**

0 Synopsis **1**
0.1 Introduction . . . 1
0.2 Motivation and Aims . . . 5
0.3 Thesis Structure . . . 6

1 Blazars: The Most Extreme Class of AGN **7**
1.1 Active Galactic Nuclei: AGN . . . 7
1.1.1 A Short History on Quasars, Blazars and AGN . . . 7
1.1.2 The Unified Model . . . 10
1.1.3 AGN Emission Lines . . . 11
1.2 Modelling the Blazar . . . 14
1.2.1 Blazar's SED . . . 15
1.2.2 Leptonic Models . . . 17
1.2.3 Hadronic Models . . . 21
1.2.4 Extragalactic Background Light Absorption . . . 22
1.2.5 Gamma-Ray Attenuation . . . 24
1.3 NVSS J163547+362930 . . . 25

2 Radiative Processes **29**
2.1 Radiative Transfer . . . 29
2.1.1 Fundamentals of Radiative Transfer . . . 30
2.1.2 Radiative Transfer Equation . . . 32
2.2 Radiation by Moving Charges . . . 34
2.2.1 Radiation Emitted in the Non-Relativistic regime . . . 35
2.2.2 Radiation Emitted in the Relativistic Regime . . . 36
2.3 Synchrotron Radiation . . . 38
2.3.1 Total Energy Loss Rate . . . 38
2.3.2 Synchrotron Spectrum . . . 40
2.3.3 Synchrotron Self Absorption . . . 42

2.4 Inverse-Compton Scattering . . . 44
2.4.1 IC Power for Single Scattering . . . 47
2.4.2 IC Spectrum for Single Scattering . . . 47
2.5 Synchrotron self-Compton Radiation . . . 48
2.5.1 SSC Contribution to the SED . . . 48
2.6 External Comptonization . . . 51
2.6.1 EC Contribution to the SED . . . 51
2.7 The Blazar's Jet . . . 52
2.7.1 High Emissions due SSC . . . 53
2.7.2 Power of the Jet . . . 54
2.8 Thermal Radiated Power due Accretion . . . 55
2.8.1 Accretion Disc . . . 56
2.8.2 The Shakura–Sunyaev Model: Stationary Approach . . . 59
2.8.3 The Multicolour Blackbody . . . 61

3 Data Analysis and Modelling **65**
3.1 Data acquisition . . . 65
3.1.1 Low-Energy Observations . . . 65
3.1.2 High-Energy Observations . . . 67
3.2 `JetSeT` . . . 68
3.3 Model Constraining . . . 70
3.3.1 Regrouping and Systematics . . . 70
3.3.2 Constraining from Observables . . . 71
3.4 Modelling the Central Engine . . . 74
3.4.1 The Disc Luminosity . . . 75
3.4.2 Prefit Model . . . 77
3.4.3 Different Accretion Efficiencies . . . 81

4 Discussions and Conclusion **85**
4.1 Markov-Chain Monte Carlo Sampling . . . 85
4.1.1 emcee Framework . . . 86
4.2 The SMBH Evolution . . . 100
4.3 Jet Power and Accretion Relation . . . 103
4.4 Lyman-Limit: Redshift Estimation . . . 105
4.5 Next Steps . . . 108
4.6 Conclusions . . . 109

Bibliography **111**

List of Figures

0.1 Variability of PKS 2155-304 of 2006 July 28 . . . 3
0.2 Spectral energy distribution for a blazar . . . 4

1.1 Rees' formation of SMBH . . . 9
1.2 AGN zoo . . . 10
1.3 Schematic of an AGN . . . 12
1.4 Composite rest-frame optical/UV spectrum for selected quasars in the SDSS . . . 13
1.5 The Fermi Blazar sequence . . . 16
1.6 Multi-epoch SED for Mkn 501 and 3C 454.3 . . . 17
1.7 One-zone blazar emission model . . . 18
1.8 Leptonic model for a high-redshift blazar SED with typical values . . . 19
1.9 Electromagnetic cascade from $p\gamma$ pion production . . . 22
1.10 Attenuation of $\gamma_{\rm HE}$ by pair-production with EBL photons . . . 23
1.11 NVSS J163547+362930 seen by DSS & SDSS . . . 27
1.12 NVSS J163547+362930 $\gamma-$ray light curve . . . 28

2.1 Electromagnetic spectrum . . . 30
2.2 Geometry for obliquely incident rays . . . 31
2.3 Moving charged particle . . . 34
2.4 Relativistic beaming . . . 37
2.5 Helical motion of a particle in a uniform magnetic field . . . 39
2.6 Synchrotron spectrum . . . 41
2.7 Compton scattering cross section . . . 45
2.8 Scattering photons from electrons in motion . . . 46
2.9 Typical example of SSC spectrum . . . 50
2.10 Bondi-Hoyle accretion disc . . . 59
2.11 Accretion disc's multicolour blackbody spectrum . . . 63

3.1 Binning and adding systematics to the SED dataset . . . 71
3.2 Prefit model using `JetSeT` . . . 72

3.3 SSD best fit for the accretion disc emissions 76
3.4 New prefit model considering a dependency in the radii of both the BLR and DT as a function of $L_{\rm disc}$ 78
3.5 SED for J163547+362930 using a SSD 80
3.6 Best fits for the SED at different accretion efficiencies 84

4.1 Corner plot for model with $\eta = 0.057$. 88
4.2 MCMC projection for model with $\eta = 0.057$. 89
4.3 Corner plot for model with $\eta = 0.083$. 90
4.4 MCMC projection for model with $\eta = 0.083$. 91
4.5 Corner plot for model with $\eta = 0.100$. 92
4.6 MCMC projection for model with $\eta = 0.100$. 93
4.7 Corner plot for model with $\eta = 0.150$. 94
4.8 MCMC projection for model with $\eta = 0.150$. 95
4.9 Corner plot for model with $\eta = 0.200$. 96
4.10 MCMC projection for model with $\eta = 0.200$. 97
4.11 Corner plot for model with $\eta = 0.300$. 98
4.12 MCMC projection for model with $\eta = 0.300$. 99
4.13 M_{BH} evolution for NVSS J16547+36293 102
4.14 Jet power versus accretion luminosity 105
4.15 Photometric redshift estimation 107

List of Tables

3.1 SED dataset 69
3.2 Parameters for the prefit model obtained by JetSeT 73
3.3 Parameters for the SED of J163547+362930 using a SSD 79
3.4 Space parameter SED 81
3.5 Parameters for the SED at different efficiencies 83

4.1 MCMC sampling of the models 87
4.2 SMBH evolution parameters 101
4.3 Jet's energetic report 104
4.4 Redshift lower limit estimation 107

Chapter 0

Synopsis

This chapter presents a comprehensive overview of active galactic nuclei, with a specific focus on blazars, their high-energy emissions, and the theoretical models used to elucidate these phenomena. This chapter emphasises the importance of investigating high-redshift blazars as a means of better understanding the early universe, particularly in relation to the evolution of supermassive black holes and their circumnuclear environment. It delves into the mechanisms responsible for both the low-energy and high-energy components of blazar emissions, including synchrotron self-Compton emission and the influence of external thermal sources. Additionally, the chapter explores the motivation behind conducting spectral energy distribution modelling for high-redshift blazars and outlines the structure of this thesis, which includes a detailed analysis of a specific blazar and its observed emissions.

0.1 Introduction

The universe is mainly composed of two energy domains: the lower energy range, covering radio to ultraviolet, and the higher energy range, spanning X-rays to $\gamma-$rays. Within this universe lies an enigmatic domain where potent energetic phenomena coexist with the subtle manifestations of lower energy states, thereby necessitating a thorough investigation that encompasses both energy spectra. The physical processes of this universe are difficult to replicate in Earth-based laboratories, making it essential to study these sources to improve our understanding of fundamental physics.

Astronomers have limited control over the processes and circumstances they observe. They depend on having telescopes and detectors ready at the right time to capture data. Nevertheless, they have the freedom to choose the source and how to do so. Additionally, by using an extensive array of sensors, they can scrutinise the phenomenon using a multiwavelength study, gaining a deeper understanding of its complexities. Thus, it is advantageous to maximise the sensitivity of every possible band of the electromagnetic

spectrum to obtain a complete picture. Moreover, astronomers have a unique advantage because sources are separated not only by distance but also by time. This allows them to understand the evolution of a source over time, and the further they look into space, the more they can learn about the observed phenomenon as well as the universe's beginnings.

Active galactic nuclei (AGNs) are a prime candidate for multiwavelength observations due to their variable emissions, which span the entire electromagnetic spectrum from radio waves to $\gamma-$rays. AGNs are some of the most luminous and energetic objects in the universe, and their primary emission is believed to be caused by accretion onto the supermassive black holes (SMBH) at the centre of the galaxy. AGNs, also known for their intense brightness, can be detected at significant redshift (e.g., the farthest-away being at a redshift of approximately $z \approx 7.6$, as reported by Wang et al. (2021)). This enables us to investigate the most distant corners of the universe and make inferences about the characteristics and evolution of SMBHs and their circumnuclear disc (CND) in the early stages of the universe.

A certain type of AGN are blazars, a type of radio-loud galaxy that have a relativistic jet aimed close to the Earth's line of sight, making them one of the most powerful sources of radiation, including γ-rays up to the TeV range. According to Prandini and Ghisellini (2022), observations of their spectra have identified two categories of blazars: the flat-spectrum radio-quasar class (FSRQ) with strong broad-line emission, and the BL Lac class (named after one of its members, BL Lacertae) with very weak or no emission lines. These jets are thought to be produced by magnetic field lines that accelerate and direct them, as neither gas nor radiation pressure can provide sufficient collimation for the large momentum flux. However, the source of this magnetic field remains not fully understood, as reviewed by Pudritz et al. (2012). There are two scenarios: a poloidal magnetic field passing through the accretion disc (as described by Blandford and Payne (1982)), and a toroidal magnetic field passing through the ergosphere of a spinning black hole (Blandford & Znajek, 1977). Most theories and simulations suggest that rapidly accreting or spinning black holes are the preferred mechanism for extracting energy and angular momentum, which generate highly relativistic jets.

Blazars are not just bright at $E > 100$ MeV, but in most cases they show their highest luminosity values in $\gamma-$ray energy band through all the spectrum. It has also been shown in multiwavelenght studies (e.g., Maraschi et al. (1994)) that the ratio of $\gamma-$ray to bolometric luminosity increases with overall luminosity. Also, these sources can be highly variable (change in flux $\geq 30\%$) on time scales of days up to seconds. One of the most famous and known examples is for the blazar PKS $2155-304$ (z=0.116) which showed a measured flux that was more than 10 times its typical values observed for $I(>200GeV)$, corresponding to ~ 7 times the flux observed from the Crab Nebula, varying on timescales of $\sim$200 s (Aharonian et al. (2007); see Figure 0.1). Another more recent example of minute time-scale variability is 3C 279 in which the γ-ray isotropic luminosity reached values $\sim 10^{49}$ erg s^{-1} (Ackermann et al.,

2016).

The presence of rapid variability strongly suggests, regardless of specific models, that the emission of $\gamma-$rays must involve relativistic beaming (Maraschi et al., 1992). This phenomenon occurs when plasma is expelled at speeds close to the speed of light, denoted as c, resulting in emissions that form an angle θ with the line of sight. This angle is inversely proportional to the Lorentz factor $\Gamma = (1 - u^2/c^2)^{-1/2}$, where u represents the velocity of the plasma. Consequently, blazars, which exhibit such relativistic beaming, rank among the most powerful entities in the universe. Therefore, comprehensive studies of blazars using multiwavelength observations are essential, specifically through the analysis of their spectral energy distribution (SED). In general, the SED is represented by plots of νF_ν or νL_ν against frequency ν, where F_ν and L_ν denote the flux and luminosity, respectively, at a given frequency. For blazars, the SED typically exhibits two peaks: one in the UV-X-ray range and another in the gamma-ray regime. Figure 0.2 provides an example of such a distribution.

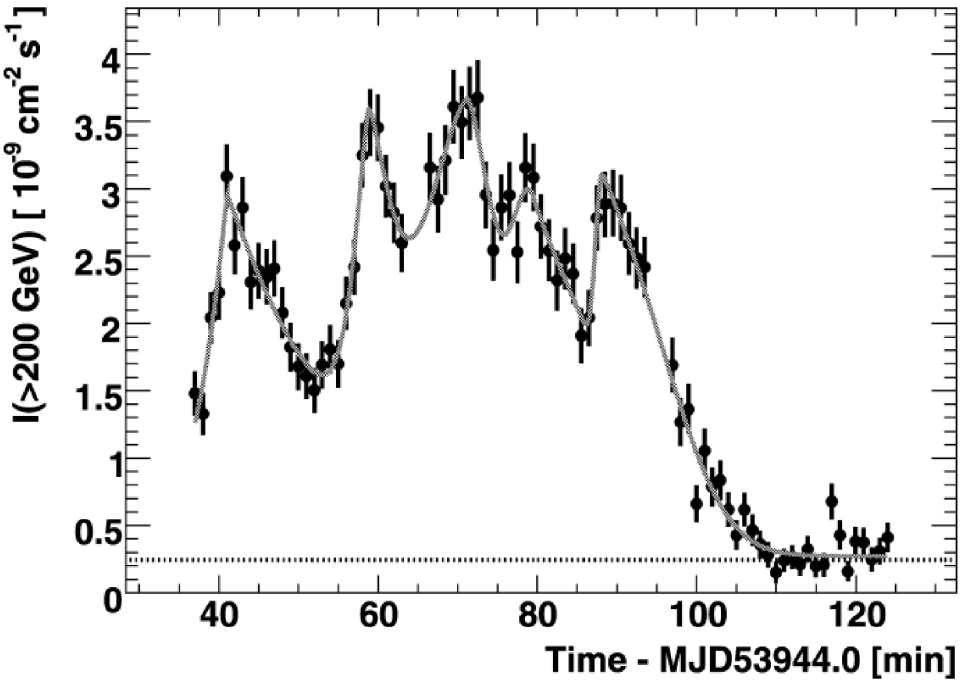

Figure 0.1. The observed flux of photons with $E > 200$ GeV from PKS 2155-304 against time, with the data binned into 1-minute intervals. The horizontal dotted-line in the graph represents the flux value from the Crab Nebula. Plot taken from Aharonian et al. (2007).

The origin of the low-energy component is well-understood and is attributed to synchrotron emission from relativistic electrons moving within the jet's magnetic field. However, the mechanism responsible for the high-energy component remains uncertain. Various models, both leptonic and hadronic, have been proposed to explain this phenomenon and offer valuable insights. In a leptonic model, high-energy emissions arise from the inverse Compton scattering (IC) of low-frequency photons by the same electrons that produce synchrotron emission. This

process, known as synchrotron self-Compton (SSC) emission (Mastichiadis & Kirk, 1996), can occur internally within the jet. It is also possible that external sources, such as the accretion disc surrounding the central black hole, clouds of hot gas in the broad-line region (BLR), or a toroidal cloud of hot dust (dusty torus or DT) surrounding this central engine, work as a seed of low-energy photons to be up-scattered to higher energies (explained further in Błażejowski et al. (2000), Bottacini, E. et al. (2010), Dermer et al. (2009), and Sikora et al. (1994) and § 2.6.1). On the other hand, in a hadronic model, the highest energy emissions in the spectrum are attributed to relativistic protons, the decay of neutral and charged pions, or muon cascades. While lepto-hadronic models are capable of describing blazar emissions, the preference leans towards the leptonic scenario over the hadronic counterpart. This inclination arises due to the leptonic scenario's demand for a magnetic field strength well below equipartition with the energy density of relativistic particles. This signifies a considerable disparity between the energy stored in the magnetic field and that contained within the accelerated particles, as exemplified by Bottacini et al. (2016).

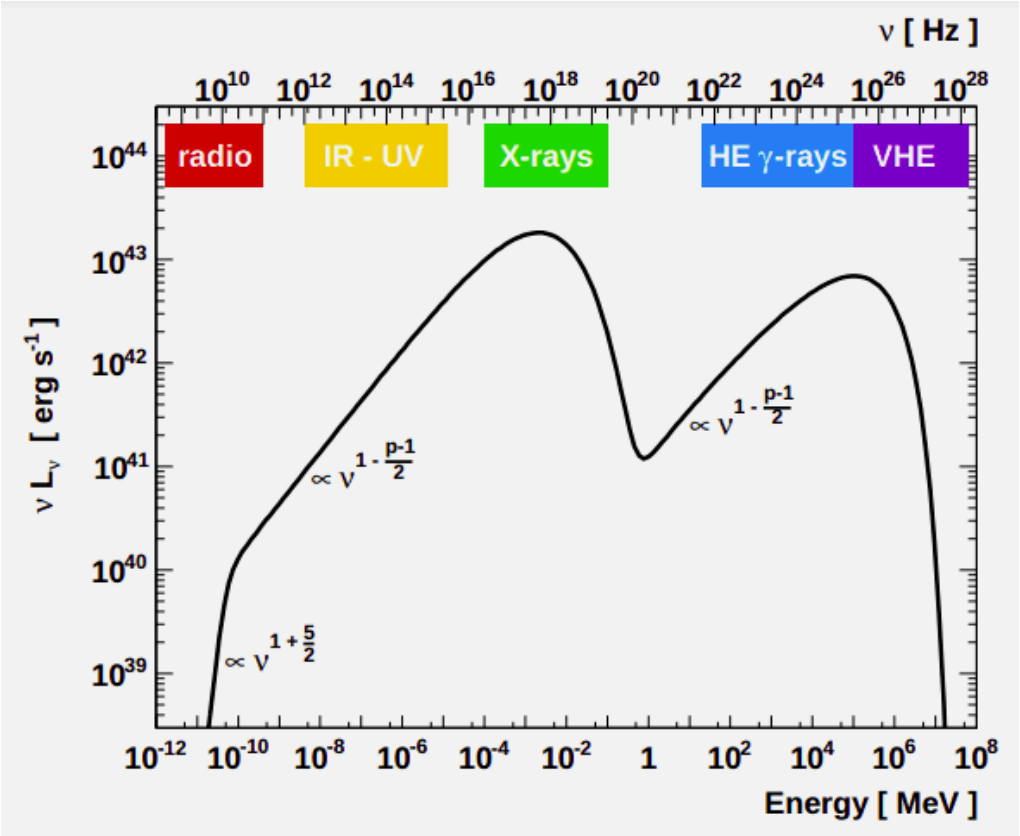

Figure 0.2. SED for a BL Lac class blazar using a synchrotron and SSC model, where the low-energy bump peaking in X-rays comes from the first and the high-energy bump comes from the latter. Figure from Biteau (2013). The slope dependencies are discussed in § 2.3.2.

0.2 Motivation and Aims

The phenomenon of relativistic beaming greatly enhances the visibility of blazars, even at high redshift, making them valuable tools for studying the early stages of the universe. Observations of high-redshift blazars have revealed the presence of sources within the range $3.0 < z \lesssim 6$ hosting SMBHs with masses exceeding $10^9 M_\odot$ (e.g., Ackermann et al. (2017), Belladitta et al. (2022), Ghisellini, Ceca, et al. (2010), Ghisellini et al. (2015), Paliya et al. (2020), and Sahakyan et al. (2020)) indicating a rapid and efficient growth of SMBHs in the early universe that is not yet fully understood (e.g., M. A. Latif and Ferrara (2016) and Volonteri (2010, 2012)). As this is only the case for blazar, we should also expect SMBH from other sources whose jets are not directed towards us, rendering them invisible. The calculation to estimate the number of these unseen sources can be performed as follows: assuming that the unique characteristics of the blazar population arise from the combination of the beaming effect and a random distribution of intrinsic source orientations, the fraction of blazars relative to the total population of radio galaxies can be obtained by integrating the following expression:

$$\frac{N(\theta < \theta')}{N} = \frac{1}{4\pi} \int_0^{\theta'} d\Omega = \frac{1}{4\pi} \int_0^{\theta'} \sin\theta d\theta d\phi \approx \frac{1}{2\Gamma^2} \tag{1}$$

Here, θ' represents the limiting angle, Γ denotes the Lorentz factor, and $N(\theta < \theta')$ represents the number of blazars within the given angle. This means that the number of galaxies that host these sources at this redshift is $2\Gamma^2 = 200(\Gamma/10)^2$ for each detected blazar. This motivates our search for high–z blazars, since it is competitive with the analogous search of heavy black holes in high–redshift radio–quiet quasars.

While moderately powerful sources have their peak emissions in the GeV range, extremely powerful sources at high redshift exhibit peak emissions in the MeV band, indicating that the search for such sources should focus on the hard X-ray band. As previously mentioned, the dominant factor behind the high-energy bump in the SED of a blazar may be the result of the Comptonisation of photons originating from external thermal sources within the blazar central region. In these instances, and especially for FSRQs, it could be possible to observe thermal radiation emissions both from the accretion disc and the surrounding hot dust, without any covering by the synchrotron flux as this peaks in the millimetre band and then exhibits a steep spectrum after reaching its peak. Therefore, by analysing the SED of a high-redshift blazar, particularly using a leptonic model for this thesis, it becomes possible to gain direct insights into the evolution of SMBHs and the CND in the early stages of the universe. The SED modelling not only improves our understanding of these components but also sheds light on the contributions made by the accretion disc, the DT, and the BLR to the generation of nonthermal broadband spectra in the high-energy band. Therefore, by modelling the SED

of these sources, we can continue studying the dominant processes responsible for producing non-thermal broadband spectra, providing valuable insight into the evolution of AGNs during the early stages of the universe.

In this study, we focus on the SED modelling of the blazar NVSS J163547+362930 ($z = 3.647763$), employing a one-zone emission leptonic model. Our analysis incorporates data from diverse missions that span the electromagnetic spectrum. To explain the observed emissions, we construct different models using the `JetSET` framework. By comparing and selecting parameter values that optimally match the observed data, we can achieve a more accurate characterisation of the properties encompassing the black hole within the host galaxy. Additionally, this approach enables a comprehensive examination of the contributions to the high-energy spectrum, facilitating a more detailed understanding of the physical processes at play.

0.3 Thesis Structure

In this thesis, we present a brief review of the previous study on AGNs and different techniques to model blazar's emissions in § 1. We give a brief description of theoretical frameworks that can guide the understanding of the radiation mechanism in blazars in § 2. We report the results and the modelling of the observed emissions from our source in § 3. Finally, the analysis and conclusions are presented in § 4.

Chapter 1

Blazars: The Most Extreme Class of AGN

This chapter provides an overview of key topics related to blazars. We will explore the nature of active galactic nuclei and their classification through a unified model, which explains their observed properties in terms of orientation and intrinsic characteristics. Also, we will examine the different types of blazars and discuss how their spectral energy distribution can be modelled using both leptonic and hadronic scenarios, which make different predictions for the observed emission. Following, we will review how multiwavelength data from radio to γ-rays can be fit to constrain the physical parameters of the blazar. Finally, a brief discussion on the main properties of the blazar of study will be done.

1.1 Active Galactic Nuclei: AGN

1.1.1 A Short History on Quasars, Blazars and AGN

At the beginning of the XX century, still the most popular way to do astronomy was through the optical band. During this time, in 1924, Edwin Hubble was inaugurating the study of extragalactic sources with his studies on the Andromeda Galaxy (M31). Almost twenty later, in 1943, Carl Keenan Seyfert did the first spectroscopy of spiral galaxies with a nucleus that outshone the rest of it, an AGN. Then, in the 1950s, scientists who worked on radar technologies during World War II, using Jansky's ('30s) and Reber's ('40s) work, discovered the first known radio galaxies: M87, Cygnus A, and Centaurus A, which all three of them emitted polarised radiation. The fact that the radiation was polarised meant that it was produced by charged moving particles; thus, it was not coming from a thermal source but from a synchrotron process.

It was until 1963 that the first quasi-stellar radio source (QSRS, or quasar) was discovered

when Marteen Schmidt realised spectroscopy on 3C 273; he measured that the spectrum, using hydrogen lines, had a redshift of 0.16 meaning it was an extragalactic source. At the same time, the second quasar, 3C 48, was discovered with a redshift of 0.37, bigger than most of the known galaxies (~ 0.2) back then. The four articles on this matter were published in Nature (e.g., Greenstein (1963), Hazard et al. (1963), Oke (1963), and Schmidt (1963)). It was also during these years that X-ray astronomy was winning popularity; so it is the case that studies performed by Bowyer et al. (1970), Friedman and Byram (1967), and Komberg and Charugin (1969) showed that there is a relation in the X-ray emission of both quasars and radio galaxies, as this emission would come from a compact central region of each source.

A couple of years later, during the Pittsburgh conference in 1978, a resemblance between two new extragalactic sources started gaining the attention of the scientific community. BL Lac objects and FSQR showed high-velocity emitting regions moving toward the observer (now known as "jets"). The name of the former comes from a first-thought variable star called BL Lacerate in the Lacerta constellation, associated with a radio source by Schmitt in 1968, and the latter was also called optically violently variables (OVVs). Both sources showed not only this moving region but also that the emissions were polarised and variable; however, the biggest difference was in the lack of emission lines in BL Lacs. During this convention, Ed Spiegel united these two objects with the name "blazar".

As noted previously, the radiation emitted from the AGN is polarised, indicating that it originates from charged particles that are accelerated by a magnetic field. This process suggests that there is an energy reservoir within the AGN, which may include relativistic particles and a magnetic field. According to a calculation of Burbidge (1959), this energy reservoir has a minimum value of approximately $\sim 10^{60}$ erg, which could increase even further when the energy of protons is taken into account. It is unlikely that this immense amount of energy could be generated by the collision hypothesis, which assumes that the gravitational potential energy from the collision of galaxies is the primary energy source. Therefore, it is clear that the energy source for the AGN must be something other than a collision between galaxies. Burbidge suggested that this energy could come from a chain reaction of supernovae, but the idea was not pursued. Instead, with pioneering work carried out by Hoyle and Fowler (1963), it was first proposed that these AGNs had a reservoir of energy that comes from gravitational energy, from the collapse of massive objects by their own gravitational field.

A few years later, Lynden-Bell (1969) concluded that the gravitational energy must be at least 30 times larger than the nuclear energy, almost affirming that the structures are powered by gravitational collapse, starting the belief that a SMBH lies at the centres of most (if not all) galaxies (e.g., Rees (1978), and Figure 1.1).

Finally in the mid 1980s, a better picture of all these objects was created with the results of large X-ray surveys showing that quasars, blazars, Seyfert galaxies, and radio galaxies host

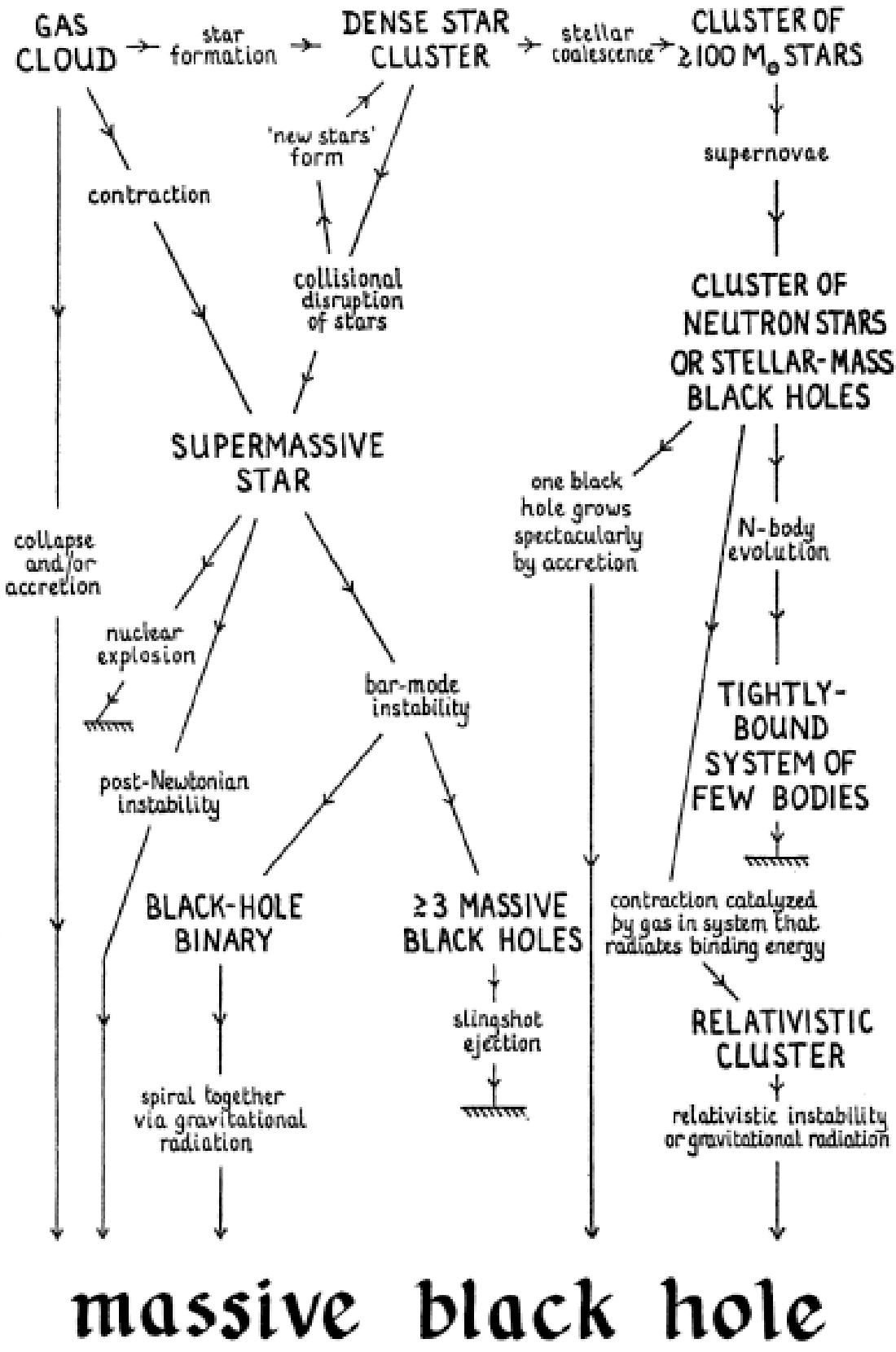

Figure 1.1. Possible modes of formation of a SMBH in an AGN. The figure is taken from Rees (1978).

an AGN, leading to the creation of a unified model.

1.1.2 The Unified Model

As a pioneer of quasars, Schmidt established the components that an object must fulfil to be classified as a quasar. These are:

- star-like object which emits on radio,
- variable emitter,
- strong emission on the UV spectra,
- large redshift,
- presence of broad emission lines.

All these criteria still apply to the classification of quasars, and it is easy to see that almost all these criteria apply to any AGN, with a few considerations that will dictate the specific type of AGN (see Figure 1.2). Typically, an AGN is constituted with the following components: a SMBH, an accretion disc, a torus, a BLR, narrow-line regions (NLR), and for some cases a superluminal bipolar jets. Under this idea, from the work by Antonucci (1993) and Urry and Padovani (1995) a theoretical framework was achieved that explains the observed diversity of AGN based on a single physical mechanism. This unified model provides a powerful tool for understanding different AGN properties, such as the SED, which is now an essential concept in AGN research.

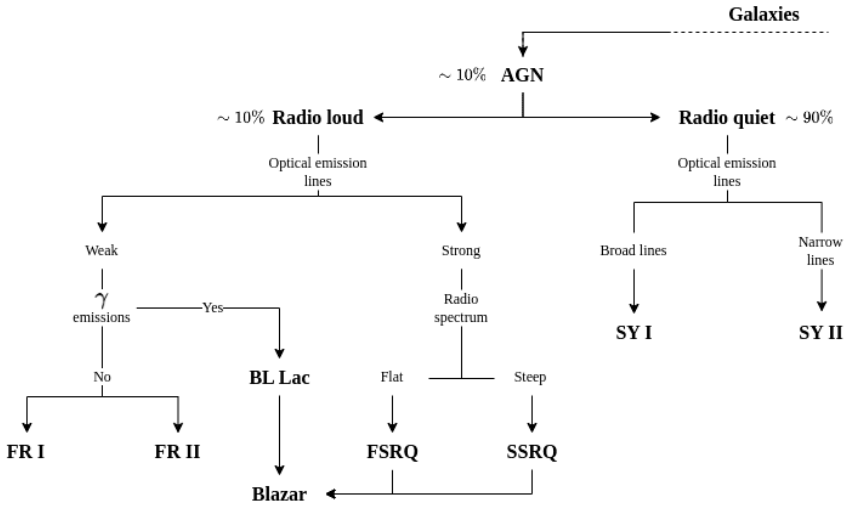

Figure 1.2. AGN classification diagram. Approximately 10% of galaxies are considered to be active, and from these $\sim 10\%$ are radio loud, meaning that blazars represent $< 1\%$ of all galaxies. AGN: active galactic nuclei; FR I and FR II: Fanaroff Riley I and II, respectively; BL Lac: BL Lacertae; FSRQ: flat-spectrum radio quasar; SSRQ: steep-spectrum radio quasar; SY I and SY II: Seyfert I and II respectively; RQ QSO: radio-quiet quasar.

In this model, the BLR is where broader emission lines are produced, whereas the NLR is believed to be where optical narrow lines originate. If the line of sight is between the jet axis and the torus plane, both the BLR and NLR are visible, and these galaxies would be classified as broad-line radio galaxies if they have radio emissions. If the torus obscures the broad-line region, the object is observed as a narrow-line galaxy. The difference in the line of sight between the jet axis and the torus plane explains the observational differences between Seyfert I and II galaxies, regardless of their radio loudness. Regardless of this, the takeaway message is that AGN will exhibit different behaviours due to differences in the observation angle of the central engine, as seen in Figure 1.3.

In Figure 1.3 it is also possible to have a better idea of the distribution and relative sizes of the AGN components. The distance of the black hole can be scaled with the event-horizon distance, the accretion disc sizes are believed to be at most of the order of light-days for the largest known black holes, and radio interferometry repeatedly shows that the superluminal jets have a length of a few kpc. For the DT, which surrounds the central engine, typical sizes of the order ~ 0.5 pc. However, it is worth considering that the advent of the James Webb Space Telescope (JWST) might potentially enable the spatial resolution of these dimensions. This is a notable advancement, as the sizes in question have remained too small to be discerned by current telescopes, due to the requirement of a resolution $\lesssim 1$ milliarcsecond or approximately 10^{-7} degrees, as previously emphasised in (Gandhi, 2005).

1.1.3 AGN Emission Lines

As mentioned earlier, AGNs exhibit distinctive emission lines in their optical spectra, emanating from two specific regions: the BLR, situated near the central engine, and the more extensive NLR. Exploring absorption lines in the optical/UV line spectrum of AGNs is of particular relevance, as they offer a wealth of information concerning the AGN's physical environment, central engine properties, and their influence on the surrounding galaxy. The study of absorption lines is particularly valuable in classifying AGNs into type I or type II categories and enables precise redshift measurements for these objects. Notably, crucial parameters such as the Full Width at Half Maximum (FWHM), density, temperature, and the distance of these regions from the SMBH are investigated to gain insight into AGN properties. For the latter, techniques such as "reverberation mapping" have been used (e.g., Peterson (1993)), where typical sizes for the BLR are

$$R_{\rm BLR} \sim 10^{17}\sqrt{\frac{L_{\rm disc}}{10^{46}}}\ {\rm cm} \tag{1.1}$$

showing a clear proportionality with $L_{\rm disc}$. Furthermore, the absorption lines serve as compelling evidence supporting the unified AGN model, as initially proposed by Antonucci

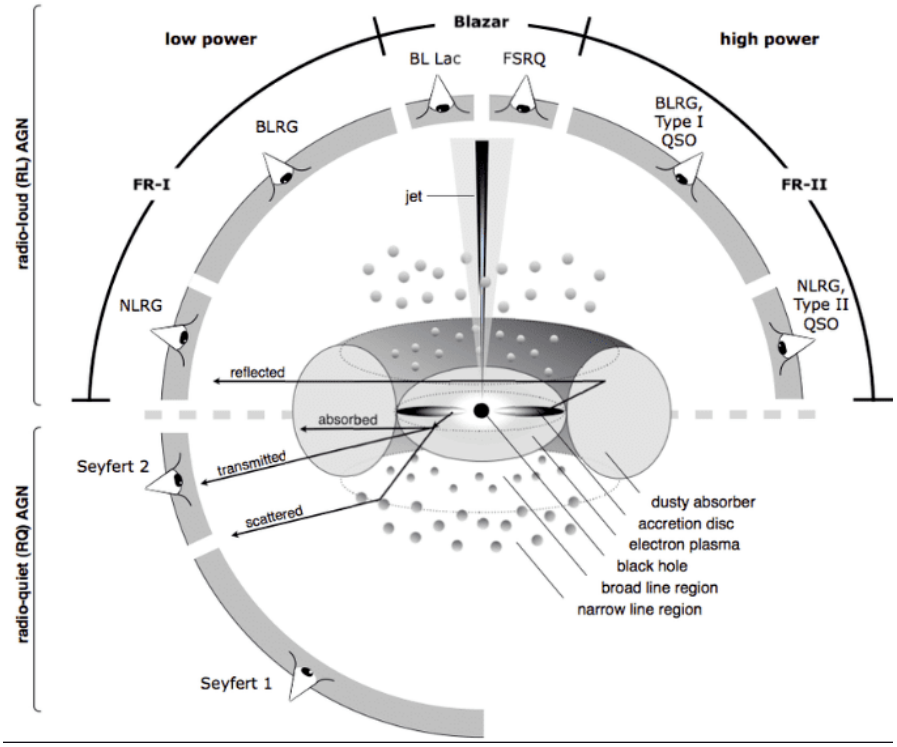

Figure 1.3. Schematic of an AGN. Figure from Beckmann and Shrader (2012). Depending on Earth's viewing angle we will see different types of the same astrophysical source. NLRG: narrow line radio galaxy; BLRG: broad line radio galaxy.

and Miller (1985). We have already said that it is only possible to see the BLR when it is not obscured by the DT, meaning we see a type I AGN. Figure 1.4 displays the composite spectra of more than 2200 of this type of quasars in their rest frame (Berk et al., 2001). The figure includes typical broad emission lines labelled for an AGN, the most prominent being the Lyman-α forest, often denoted as Ly-α forest. The Lyman series of spectral lines originates from the atomic electron transitioning from an $n = 2$ orbital to the ground state ($n = 1$), where n represents the principal quantum number. For hydrogen, the Ly-α line, which has the greatest increase in flux, has a wavelength of 1215.67 Å, corresponding to a frequency of approximately 2.47×10^{15} Hz, placing it in the UV part of the electromagnetic spectrum. While the Lyman-limit, the limit of the Lyman series, has a wavelength of 912 Å, also in the UV region. As the typical values for these lines can be accurately measured in a lab, it is possible to get all the information related to redshift of the AGN.

Typically in an AGN, the broad emission lines show values consistent with emission from regions that have an average speed of about ~ 5000 km s^{-1} (De Angelis & Pimenta, 2018). These velocities are too large to be solely attributed to thermal motions. For example, consider a cloud with a temperature of $T \sim 10^4$ K, fully exposed to intense radiation from the AGN engine. At this temperature, the thermal broadening effect, which arises from

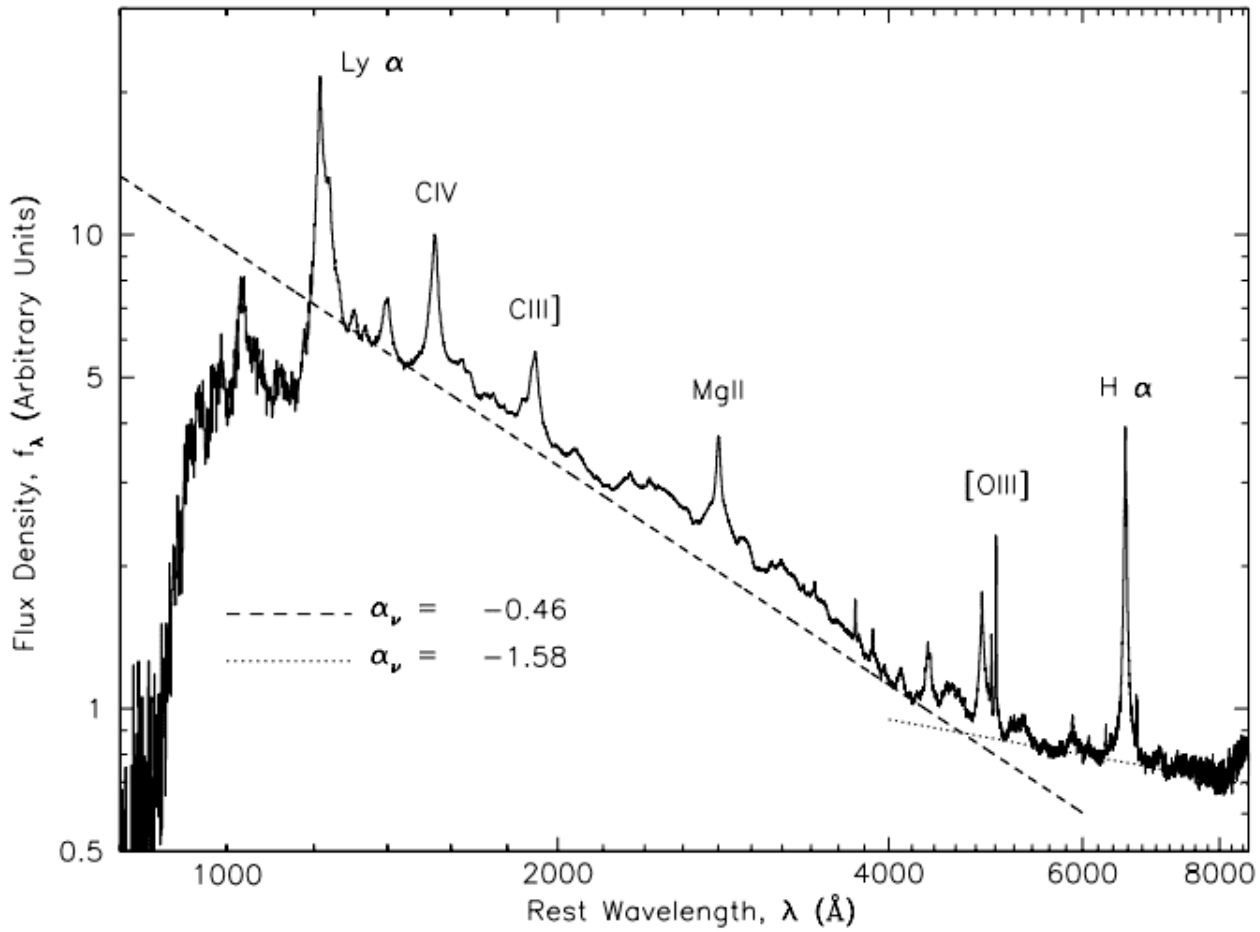

Figure 1.4. The composite optical/UV spectrum in the rest frame consists of more than 2200 quasar spectra sourced from the Sloan Digital Sky Survey (SDSS). Power-law fits to the continuum emission are illustrated by the dashed and dotted lines. Plot taken from Berk et al. (2001).

Doppler-broadening as a result of the movement of radiating particles relative to the observer, is

$$u \sim 10\sqrt{\frac{kT}{m_p}} \sim 10 \text{ km s}^{-1} \tag{1.2}$$

for a proton with mass $m_{\rm p}$, where k is the Boltzmann constant. This result implies that we require bulk motions (in various directions with respect to our line of sight) of the material emitting the lines, as the thermal motions alone cannot account for the observed velocities.

On the other hand, narrow emission lines show a FWHM of around 400 km s^{-1}, but as the NLR are located at greater distances than the BLR, they are unaffected by the possible presence, in a region close to the accretion disc, of absorbing material.

1.2 Modelling the Blazar

As already said, blazars, which represent less than 1% of the total number of galaxies, are a type of AGN that emits through all the electromagnetic spectrum, from high-energy radiation, including gamma rays, X-rays, to radio waves, making them among the most energetic and variable objects in the universe. What makes blazars unique is that their relativistic jets, associated with accretion onto the SMBH, are pointed directly towards the Earth, giving us a direct view of the powerful emission from these jets. This makes them one of the most important sources of information on the extreme physical processes that occur in the vicinity of SMBH.

The polarised emissions, variability, and apparent superluminal motions provide compelling evidence of a non-thermal continuum emission from small regions in their jets, travelling at relativistic speeds at a small angle relative to our line of sight. The low-frequency component of the SED is well established to come from synchrotron radiation from non-thermal, ultrarelativistic electrons. However, these relativistic electrons must be injected into the jet through different electron injection/acceleration scenarios, including impulsive injection (Dermer et al., 1997), isolated shocks (Sokolov et al., 2004), internal shocks (Spada et al., 2001), stochastic particle acceleration (Rieger & Duffy, 2004), magnetic reconnection (Sikora et al., 2005), and pair avalanches initiated by hadronic processes (Kazanas & Mastichiadis, 1999; Mannheim, 1993).

Still, there is a larger discussion of the origin of high-frequency emissions. This part of the spectrum is modelled by two fundamentally different approaches: a leptonic model, dominated by ultra-relativistic electrons draining energy to photons through inverse Compton scattering (ICS); and a hadronic model, dominated by hadronic cascades initiated by a $p-\gamma$ pair producing $\pi^{\pm}$ as well as protons, neutrons, and $\mu^{\pm}$. Although both models can explain some observed features of the blazar, they make different predictions for the emission at certain

wavelengths. For example, leptonic models predict that the gamma-ray emission should be strongly correlated with the X-ray emission, while hadronic models may not necessarily predict such a correlation. Additionally, hadronic models may predict the presence of high-energy neutrinos and $\gamma-$rays from neutral pion decay, while leptonic models do not produce such emission.

In this section, we will first briefly discuss the blazar SED's main characteristics following an explanation on the emission models of blazars based on a leptonic jet. Nevertheless, a comment on the hadronic model will take place.

1.2.1 Blazar's SED

Blazars can be categorised based on various factors in addition to their emission lines, as they are a complex group of objects with various sub-classifications. These categories can include their discovery method (e.g., radio or X-ray), the position of their synchrotron peak in the spectrum (e.g., Abdo et al. (2010)), and the presence or absence of broad emission lines. When examining these sub-classifications, it is important to consider the concept of equivalent width (EW), which describes the EW of both absorption and emission lines. The formula for EW is the following:

$$EW = \int \frac{F_0 - F_\lambda}{F_0} d\lambda. \tag{1.3}$$

Here, F_λ represents the total flux (line + continuum) and F_0 represents the flux of the continuum. In the case of emission lines, the result is negative, so sometimes the absolute value is given. Units of EW are usually in angstroms (Å), where $1\text{Å} = 10^{10}$ m. As already discussed, the main subgroups for blazars are BL Lac and FSRQ, and the rule for classifying them is as follows (Stickel et al., 1991):

$$\text{Blazar} \begin{cases} \text{BL Lac}, & \text{if } EW < 5\text{Å, showing weak or non emission lines.} \\ \text{FSRQ}, & \text{if } EW > 5\text{Å, showing broad emission lines.} \end{cases}$$

The EW reveals that FSRQs, similar to radio-quiet AGNs, exhibit broad emission lines. In contrast, BL Lacs typically exhibit weak emission lines most occasionally displaying absorption features. Given the highly variable nature of blazars, the categorisation relies on the source's observed state. This is because EW is a ratio involving both the line and the beamed optical flux, in which the latter fluctuates over time. Further classifications can also be made depending on the frequency at which a luminosity peak is found; this is also called the blazar sequence.

Using multiwavelength data from 126 sources, Fossati et al. (1998) proposed the blazar sequence in which they were able to relate the observational properties in the SED of blazars

with a specific class of AGN. This framework proposed that BL Lac objects and FSRQs with higher power levels would exhibit lower synchrotron peak frequencies, $\nu_{\rm peak}$, while those with lower power levels would have higher $\nu_{\rm peak}$ values. Although the original framework is somewhat controversial as a number of objects deviate from this scheme by showing a high total luminosity for a high value of $\nu_{\rm peak}$ (e.g., Giommi et al. (2012), Padovani et al. (2012), Padovani et al. (2003), and Scarpa and Falomo (1997)), and different models for the explanation on electron cooling process were being developed (e.g. Asano and Hayashida (2018)), a revised sequence called the *Fermi* blazar sequence was proposed by Ghisellini et al. (2017) as the detection of more than 1500 blazars, to that date, was reported in the 3LAC catalogue (Ackermann et al., 2017). The results show, as explained in the review by Prandini and Ghisellini (2022) that a noticeable trend is observed as the luminosity decreases, where in both the synchrotron and inverse Compton peak positions undergo a shift. The results of this framework can be seen in Figure 1.5.

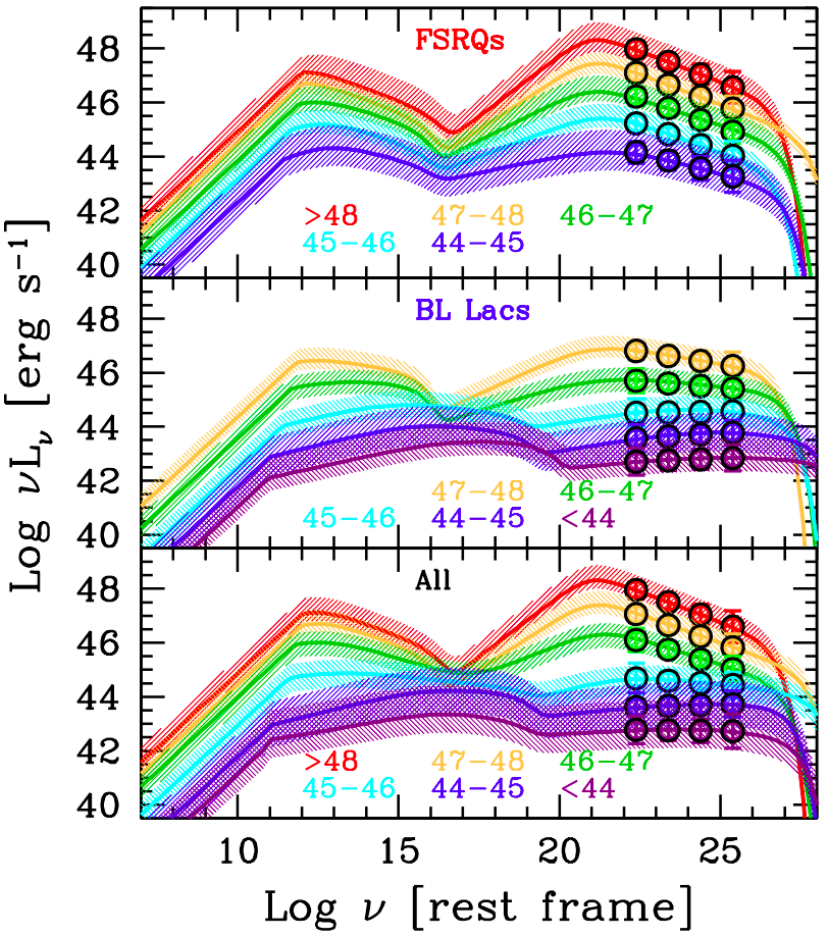

Figure 1.5. The Fermi blazar sequence, as described by Ghisellini et al. (2017). In the top panel, FSRQs belonging to different luminosity classes demonstrate an upward shift of the $\nu_{\rm peak}$ as luminosity decreases, the same behaviour being clearly manifested also in BL Lac objects. Thus, the same behaviour is seen plotted indiscriminately.

Regardless of the sub-classification of blazars, their SED exhibits two wide peaks. Although the specific frequencies at which these peaks occur can vary across blazars, typically the first peak is observed at lower energies between the millimetre and soft X-ray wavelengths. In contrast, the second high-energy peak is usually detected in the MeV-GeV range. Another main characteristic of blazars is their high variability, especially at high energies. Figure 1.6 illustrates the multi-epoch SEDs of two blazars, namely the BL Lac object Mkn 501 and a powerful FSRQ 3C 454.3 respectively, serving as an illustrative example. This high variability, even detected in high-redshift blazars (e.g., Li et al. (2018)), is likely due to changes in the flow of the plasma and magnetic fields in the jet, which can result in changes in the emission of radiation (Marscher, 2016). In particular, for the multi-epoch spectrum from 3C 454.3, it is possible to see even 2 orders of magnitude in the variability of the flux. It is clear that, for low states in the flux, it is possible to see the "naked" contributions from the accretion disc.

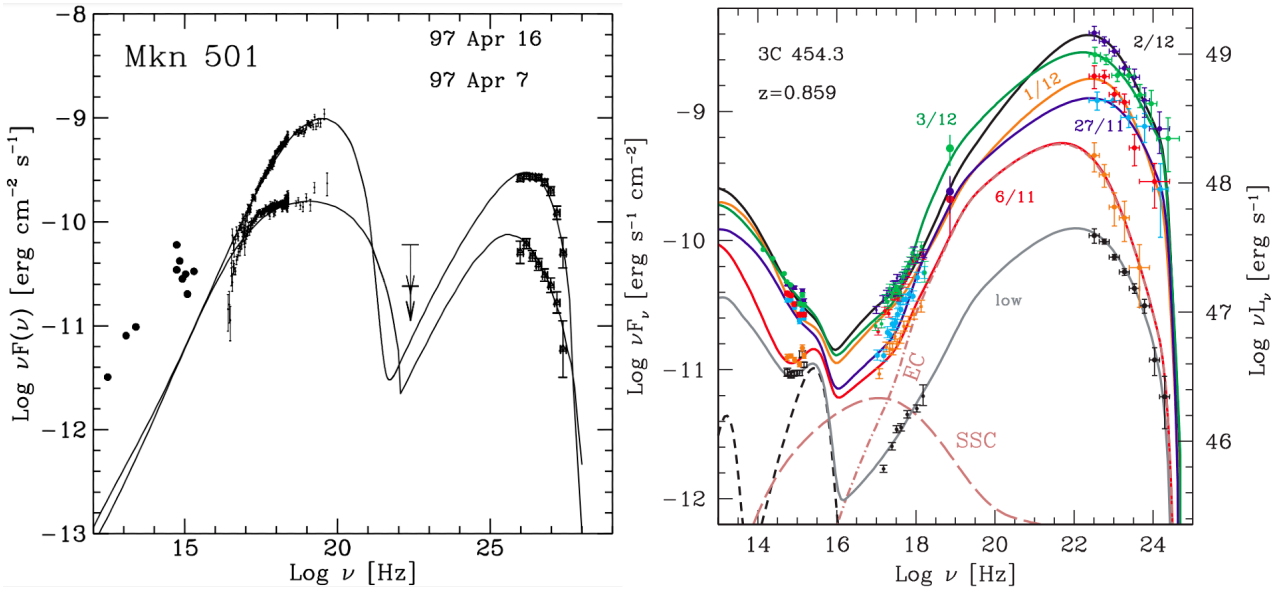

Figure 1.6. Left: SED for Mkn 501 during two different dates in April 1997, the spectrum was taken from Tavecchio et al. (2001); right: SED for 3C 454.3 during five different dates from November to December of 2009, plus a "low" γ-ray state, the spectrum was taken from Bonnoli et al. (2011).

1.2.2 Leptonic Models

In the simplest leptonic scenario, the radiation emission occurs within a uniform and solitary area called a "blob", where all leptonic processes originate from the same source; this approximation is commonly referred to as the one-zone homogeneous model. This blob, measuring size R, resides in the jet at a distance of $R_{\rm diss}$ from the central black hole and moves at a bulk Lorentz factor of Γ (refer to § 2.2.2), while containing a tangled, homogeneous magnetic field of strength B. Moreover, is in the blob where the extremely high-energy

electrons are situated. However, this is a simplification, as suggested by Ghisellini and Madau (1996), multiple emitting regions may be better suited for most of the cases studied. The one-zone model can be seen in Figure 1.7.

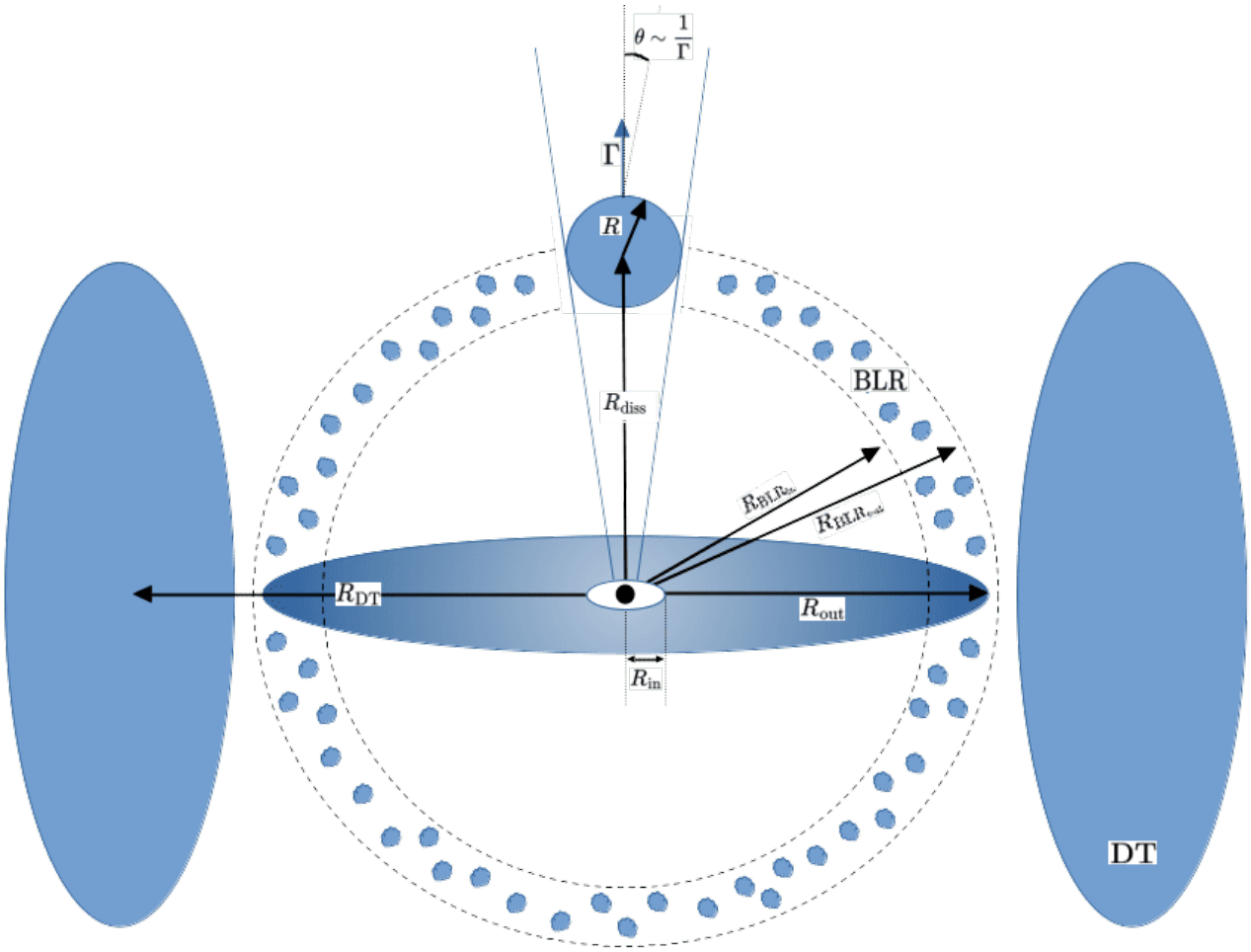

Figure 1.7. The one-zone model assumes a particular geometric configuration, depicted in a sketch (not to scale). The model considers a spherical BLR with a radius of $R_{\rm BLR}$, and a spherical DT surrounding the central engine at a distance of $R_{\rm DT}$. The emission being analysed originates from a compact blob of small radius R, and from a distance of $R_{\rm diss}$ from the black hole, which moves with a Lorentz factor of Γ. The limits of the accretion disc are denoted by $R_{\rm in}$ and $R_{\rm out}$, and all distances are measured relative to the black hole at the origin.

It is thought that both synchrotron and IC radiation are responsible for the broadband continuum spectrum. Although the low-energy peak is well established to be produced due to synchrotron radiation from relativistic electrons, in leptonic models, the high-energy emission is produced by ICS of low-energy photons that are produced during the synchrotron emission at lower frequencies. Depending on the location of birth of these low-energy photons, the process is either the synchrotron self-Compton (SSC) or the external Compton (EC) (e.g., Bloom and Marscher (1996) and Marscher and Gear (1985)). Both of these processes can be better seen in § 2.4. These seed photons can originate from the accretion disc (e.g., Dermer et al. (1992)),

from a fraction of the disc's luminosity reflected by the BLR (e.g., Sikora et al. (1994)) or the dusty torus in the infrared (e.g., Błażejowski et al. (2000) and Ghisellini and Madau (1996)), or from synchrotron radiation between decelerating and accelerating relativistic flows (e.g., Georganopoulos and Kazanas (2003)). In most cases, the sum of these processes is used to fit the SED. An illustration example can be seen in Figure 1.8.

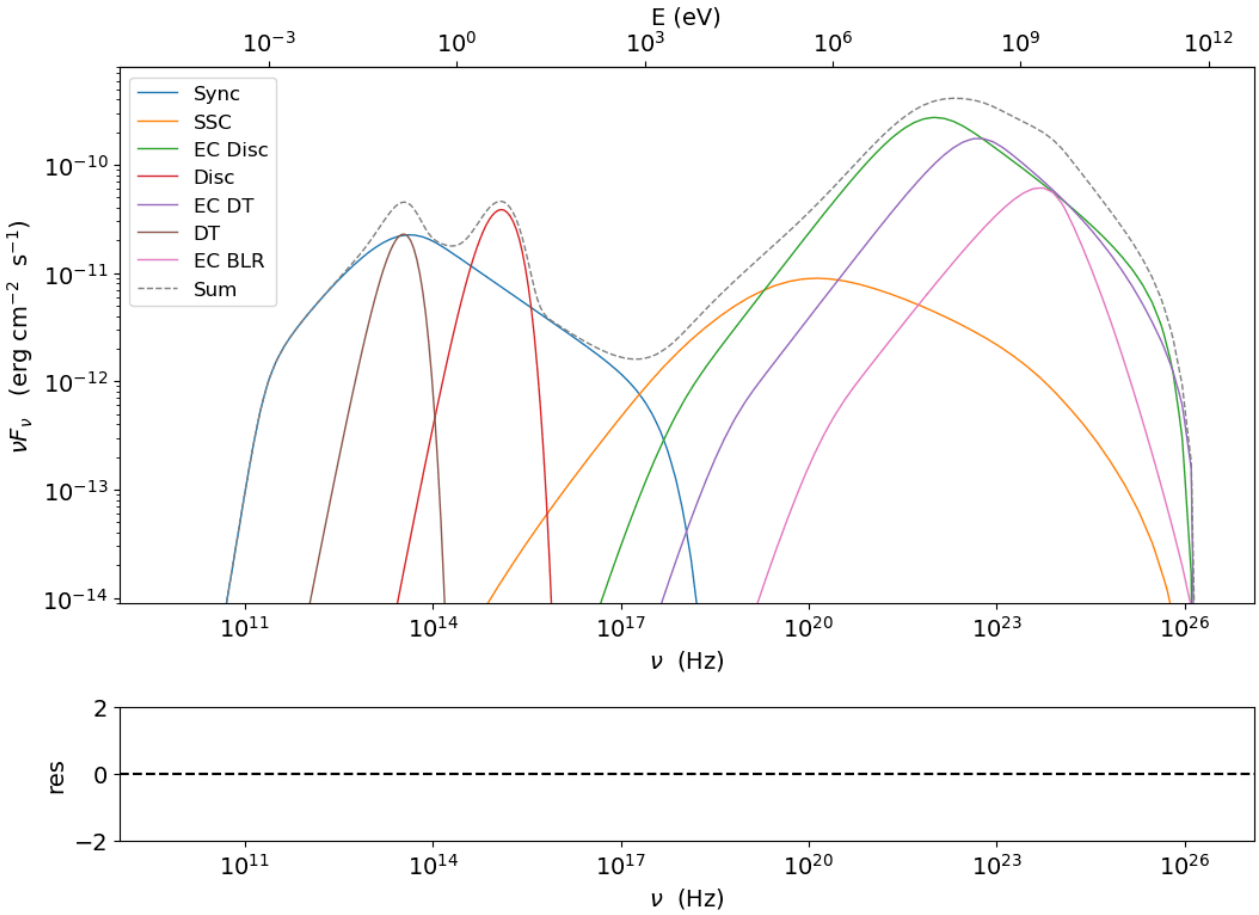

Figure 1.8. Leptonic model for a high-redshift blazar SED. All components are discussed in great detail in § 2. The abbreviations of the legend are: Sync, synchrotron radiation; SSC, synchrotron self Compton; EC Disc, external comptonization from the disc; EC DT; external comptonization from the dusty torus; EC BLR, external comptonization from the BLR; and the dashed line, Sum, is the sum of all the components.

To accurately model radiation spectra in this framework, it is necessary to consider various mechanisms that can modify the spectra. For example, the presence of $\gamma - \gamma$ absorption, both internal and external to the radiation source, can create additional relativistic electron-positron pairs. Moreover, to ensure precise spectral modelling, one must consider self-consistent continuous particle injection and/or acceleration, radiative and adiabatic cooling, and particle escape, as the emission region travels at relativistic velocities along the jet (Böttcher, 2007). The cooling mechanisms involved in the emission region

require a more realistic approach to determine the electron distribution function, such as those based on shock-acceleration theory. This is because simpler models rely on an ad hoc approach where the electron and/or positron distribution is predetermined by specifying, in most of the cases, a single or broken power-law with energy cut-offs at the high and low end.

To better understand this last concept, let us briefly discuss how an electron distribution is defined, particularly one that follows a broken power law. In general, an electron distribution is defined by the following:

$$\begin{aligned} \frac{dN}{dVdE} &= Kf(E) \\ n(E) = \frac{dN}{dV} &= Kf(E)dE \end{aligned} \tag{1.4}$$

where dV is the volume cell, $f(E)$ the differential electron distribution, $n(E)$ the differential electron distribution function, dE an energy range, and K a normalisation constant. Using the fact that $E = \gamma mc^2$, it can also be written as

$$n(\gamma)d\gamma = Kf(\gamma)d\gamma. \tag{1.5}$$

As said, for most of the time, it is enough to model the SED from a blazar using a broken power-law which must be defined over the energy interval [$\gamma_{\rm min}$, $\gamma_{\rm max}$]. Thus, it is possible to write down:

$$f(\gamma) = \begin{cases} (\gamma)^{-p}, & \gamma \leq \gamma_{\rm break} \\ (\gamma)^{-p_1}, & \gamma > \gamma_{\rm break} \end{cases} \tag{1.6}$$

where p is the low energy spectral index, p_1 the high energy spectral index, and $\gamma_{\rm break}$ the turnover energy. In some cases, it is also common to use different differential electron distributions such as a single power-law, a combination of a power-law plus an exponential cutoff, a logarithmic parabolic function (e.g., E. Massaro et al. (2004)), logarithmic parabolic function plus a power-law low (e.g., E. Massaro et al. (2006)), just to name a few different examples. In any case, this distribution function must then be normalised to unity through the constant K by:

$$\int_{\gamma_{min}}^{\gamma_{max}} Kf(\gamma)d\gamma = 1. \tag{1.7}$$

Thus, by definition, the numerical value N represents the number of particles emitting per unit volume, measured in units of $1/\mathrm{cm}^3$.

$$N = \int_{\gamma_{min}}^{\gamma_{max}} n(\gamma)d\gamma = \int_{\gamma_{min}}^{\gamma_{max}} Kf(\gamma)d\gamma \tag{1.8}$$

While these distributions may not be the most realistic, they have been successful in

reproducing blazar SEDs. However, for more information on self-consistent distributions for modelling the SED, the reader can refer to literature sources such as Acciari et al. (2009), Ghisellini and Tavecchio (2009), and Weidinger et al. (2010).

Although thermal emissions have not yet been discussed, they are expected to contribute to both EC processes and direct thermal emissions, regardless of whether a leptonic or hadronic model is used. In addition, the accretion disc is expected to contribute to direct thermal emissions because of the thermal motion of its matter as a result of the release of gravitational potential energy during matter infall into the SMBH. Furthermore, the viscous forces that drive the accretion process also generate heat in the disc. These thermal emissions typically have temperatures ranging from 10^{3-4} K, and fall within the mid-infrared to visible range of the electromagnetic spectrum. A simple blackbody profile is sufficient to model the spectral radiation emitted by the DT, whereas the accretion disc emissions require a multicolour-blackbody profile, which is explained in detail in § 2.8. Both contributions can be clearly seen in Figure 1.8.

1.2.3 Hadronic Models

In the early 1990s, Karl-Heinz Mannheim was among the trailblazers in the investigation of hadronic models for blazar emission, as evidenced in his published works (e.g., Mannheim and Biermann (1989, 1992) and Mannheim (1993)). He proposed several models that postulated the production of high-energy neutrinos and $\gamma-$rays from the interaction of relativistic protons with ambient matter or photons within the jet. Recently, these models have received renewed interest after the detection of high-energy neutrinos by IceCube (IceCube Collaboration, 2013), which could potentially be associated with hadronic blazar models (Cerruti et al., 2015; Tavecchio et al., 2014; Zheng et al., 2016). Mannheim's pioneering work has significantly impacted the field of astrophysics and particle physics, offering a plausible explanation for the origin of cosmic rays and the observed high-energy emissions from blazars.

In this scenario, relativistic protons within the jet are accelerated to ultra-high energies (UHE) through mechanisms such as diffusive shock acceleration where significant magnetic-field amplification is required. These UHE protons ($E_p \approx 10^{19}$ eV) then interact with ambient matter or photons, producing π^0, $\pi^{\pm}$, and kaons (K) through $p - \gamma$ interactions that lead to an electromagnetic cascade (see Figure 1.9).

During this process, UHE cosmic rays are also generated, such as neutrinos, which may be detected in projects like IceCube, providing evidence for the underlying energy production mechanisms, as discussed in Cerruti et al. (2022) and Halzen and Kheirandish (2016). Generating UHE protons requires high magnetic fields, usually several tens of Gauss.

$$p_{\mathrm{UHE}} + p/\gamma \rightarrow p/n + \pi^0 + \pi^{\pm} + K^{0,\pm}$$

$$\pi^0 \rightarrow \gamma + \gamma$$

$$\pi^{\pm} \rightarrow \mu^{\pm} + \overset{(-)}{\nu}_{\mu}$$

$$\mu^{\pm} \rightarrow e^{\pm} + \nu_e + \overline{\nu}_e$$

$$K^{0,\pm} \rightarrow \pi^0 + \pi^{\pm} + \mu^{\pm} + \nu_{\mu} + \overline{\nu}_{\mu}$$

Figure 1.9. Whenever a UHE proton (p_{UHE}) interacts with another proton or $\gamma-$ray from the jet's environment, an electromagnetic cascades can be started by subsequent processes, including photons from π^0-decay, $\pi^{\pm}$-decay, and$\mu^{\pm}-$decay.

This is necessary to confine the Larmor radius

$$R_L = 3.3 \times 10^{15} \Big(\frac{E_p}{10^{19}\mathrm{eV}}\Big)\Big(\frac{10\mathrm{G}}{B}\Big)\ \mathrm{cm}, \tag{1.9}$$

to a size smaller than the emission region (as discussed, typically $R \approx 10^{16}$ cm). In the presence of such high magnetic fields, synchrotron radiation from primary protons, as well as secondary muons and mesons, must be taken into account to create a consistent synchrotron-proton blazar model (SPB) (Mücke & Protheroe, 2000).

As a last comment, hadronic models have been very difficult to investigate in a time-dependent manner because they require computationally intensive Monte Carlo simulations. Despite this, the rapid time variabilities observed are not in line with the radiative cooling time scales of protons, and the occurrence of correlated X-ray/TeV flares cannot be adequately explained using hadronic models. However, spontaneous flares at the high-end of the TeV spectra can be readily accounted for in such models (Boettcher, 2011).

1.2.4 Extragalactic Background Light Absorption

As mentioned above, SED can be influenced by $\gamma - \gamma$ interactions, leading to absorption processes. These interactions extend beyond the Cosmic Microwave Background (CMB), which emerged about 380,000 years after the Big Bang, signifying the universe's transition

to transparency, but they also involve the Extragalactic Background Light (EBL), spanning a wide frequency range from IR to UV wavelengths ($0.1 \leq \lambda \leq 1000\mu m$). The EBL is believed to have originated when the first cosmic sources began emitting light at a redshift of approximately $z \sim 10$, uniformly filling the universe. Consequently, these interactions between the EBL and high-energy photons $\gamma_{\rm HE}$ from, said, blazars, resulting in pair production, lead to noticeable opacity effects, manifesting as high-energy cutoffs in the spectra of these sources at high and very high energies (e.g., Stecker et al. (1992)). We said that the photon absorption in the EBL is relevant for $\gamma_{\rm HE}$ because the probability for photon absorption depends on the cross section for pair production, which increases with increasing energies. This attenuation of $\gamma_{\rm HE}$ also depends on the distance these emissions have travelled to reach Earth (see Figure 1.10; e.g., Gilmore et al. (2012)). Thus, the study of the EBL not only gives us a better understanding in the SED modelling, but also the EBL can be used to provide constraints on the history of galaxy formation and evolution, as it is directly linked to the star formation history of the universe. We will now briefly review the key elements of these interactions. For this, and for a better treatment of the derivation, please refer to the literature, i.e., Franceschini et al. (2008) and Gilmore et al. (2012).

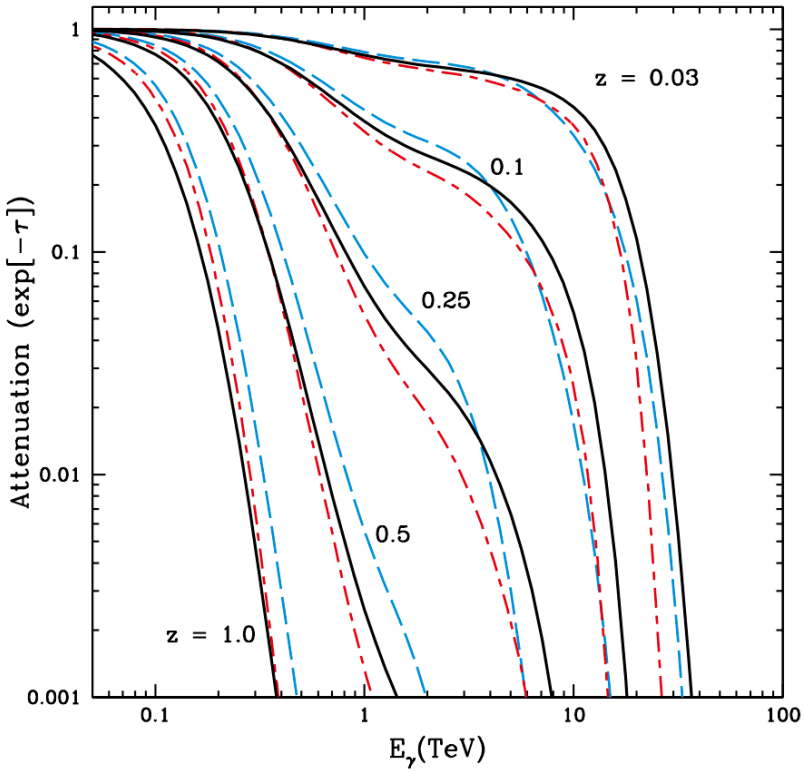

Figure 1.10. The attenuation of $\gamma_{\rm HE}$ vs. $\gamma_{\rm HE}$ energy, for sources at $z = 0.03$, 0.1, 0.25, and 0.5, and 1. The different lines represent distinct outcomes obtained from various cosmological models. Further details regarding the models and the plot can be accessed in the publication by Gilmore et al. (2012).

1.2.5 Gamma-Ray Attenuation

The overall scenario of electron-positron pair production resulting from interactions between high-energy gamma rays ($\gamma_{\rm HE}$) and the EBL can be described as follows:

$$\gamma_{\rm HE} + \gamma_{\rm EBL} \rightarrow e^- + e^+ \tag{1.10}$$

Here, $\gamma_{\rm EBL}$ represents an EBL photon, and e^- and e^+ denote the production of an electron and positron, respectively. Quantum electrodynamics provides the best understanding of this process. The fundamental kinematic requirement for pair production is that there must be sufficient energy in the centre-of-mass frame of the two-photon system to generate the pair, which can be expressed as:

$$\sqrt{2E_{\rm HE}E_{\rm EBL}\left(1-\cos\theta\right)} \geq 2m_e c^2 \tag{1.11}$$

Here, E represents the energy of each photon, θ denotes the angle of incidence, and m_e is the rest mass of the electron. Consequently, a threshold energy $E_{\rm th}$ can be computed for a background photon to interact with a γ-ray:

$$E_{\rm th} = \frac{2m_e^2c^4}{E_{\rm HE}(1-\cos\theta)} \tag{1.12}$$

Considering the cross-section for this process, as described by Gould and Schréder (1967), given by:

$$\sigma\left(E_{\rm HE}, E_{\rm EBL}, \theta\right) = \frac{3\sigma_T}{16}\left(1-\beta^2\right) \times \left(2\beta(\beta^2-2) + (3-\beta^4)\ln\left(\frac{1+\beta}{1-\beta}\right)\right) \tag{1.13}$$

with

$$\beta = \sqrt{1 - \frac{2m_e^2c^4}{E_{\rm HE}E_{\rm EBL}(1-\cos\theta)}} \tag{1.14}$$

and σ_T representing the Thompson cross-section, it can be observed that the cross-section is maximised for photons at approximately 4 times the value of $E_{\rm th}$ and when in a "head-to-head" configuration ($\theta \approx \pi/2$). Assuming $\theta = \pi/2$, we find that the photons that have the strongest impact on $\gamma_{\rm HE}$ have an energy of:

$$E = \frac{4m_e^2c^4}{E_{\rm HE}} = 1.044\left(\frac{\rm TeV}{E_{\rm HE}}\right)\,{\rm eV} \tag{1.15}$$

Hence, it can be concluded that the upper limit of IR light has the most significant influence on these energetic photons.

Within conventional physics, the effective flux of photons reaching the Earth is attenuated as

$$I = I_0 \exp\left[-\tau(E, z)\right] \tag{1.16}$$

where I_0 represents the flux of photons emitted at the source, and $\tau(E, z)$ the optical depth for a gamma ray observed at energy E at redshift z. This τ can be obtained by performing the integral along the line of sight to the target as

$$\tau(E, z_0) = \frac{1}{2}\int_0^{z_0} dz \frac{dl}{dz} \int_{-1}^{1} du(1-u) \times \int_{E_{\min}}^{\infty} dE_{\rm EBL} n(E_{\rm EBL}, z)\sigma(E_{\rm HE}(1+z), E_{\rm EBL}, \theta) \tag{1.17}$$

for which $E_{\min} = E_{\rm th}(1+z)^{-1}$, $n(E_{\rm EBL}, z)$ is the photon density align the line of sight, u is the typical change of variable $\cos\theta$, $\sigma(E_{\gamma_{\rm HE}}(1+z), E_{\rm EBL}, \theta)$ is the $\gamma - \gamma$ interaction cross section, and dl/dz is the cosmological line element described for a flat ΛCDM universe as

$$\frac{dl}{dz} = \frac{c}{H_0(1+z)\sqrt{\Omega_m(1+z)^3 + \Omega_\Lambda}} \tag{1.18}$$

Disregarding atmospheric effects, when considering small redshifts, the transparency of the universe allows $\tau(E, z) < 1$, implying unobstructed propagation of photons from the source. However, depending on the energy E, there exists a specific point along the line of sight where the universe can become optically thick. Consequently, a threshold redshift value can be calculated using Equation 1.16, indicating that beyond this horizon, the source becomes nearly invisible at high energies. Therefore, regardless of the type of model used for the SED analysis, when modelling a high-redshift blazar, it is crucial to consider EBL corrections in order to gain a better understanding of the emission processes that contribute to the high-energy portion of the spectrum.

1.3 NVSS J163547+362930

Blazars are a crucial subject of study in astrophysics, cosmology, particle physics, and plasma physics because of the unique conditions they offer for probing physical processes involving extreme acceleration, density, and magnetic and gravitational fields. Additionally, blazars with gamma-ray emissions are valuable tools for investigating the evolution of galaxies throughout the history of the universe, as they exhibit redshifts ranging from around 0.1 to greater than 5. An example of a high-redshift blazar is NVSS J163547+362930, which has a redshift of 3.65 (Pâris et al., 2018) and is located at RA. = 248.94682 deg and Decl. = +36.49166 deg (J2000; Petrov and Taylor (2011)). This object not only gives us the opportunity to study the mentioned phenomena, but also gives us insight into the creation

and evolution of the SMBH, which for this particular case was formed in the first 2 billion years since the Big Bang (Ackermann et al., 2017).

First reported in the third MIT - Green Bank 5 GHz survey (Griffith et al., 1990), NVSS J163547 + 362930 has now been part of several multiwavelength studies. NVSS J163547 + 362930 has also been observed by the Sloan Digital Sky Survey (SDSS) and the Digital Sky Survey (DSS) (see Figure 1.11), it has also been reported to be detected by the Large Area Telescope (LAT), one of the two instruments on the *Fermi* Gamma-ray Space Telescope, back in 2017, showing increasing gamma-ray activity (Ackermann et al., 2017). According to the initial analysis of Paliya et al. (2018), this source began to exhibit a high flux state on 7 July 2018, with the daily averaged gamma-ray flux ($E > 100$MeV) peaking at $6.4 \pm 1.5 \times 10^{-7}$ photons cm^{-2}s^{-1} (statistical uncertainty only) on 8 July. This represents the highest daily flux ever observed for this source. The photon index associated with this high flux state is 2.6 ± 0.2, indicating a harder spectrum compared to the previously reported index of 3.2 ± 0.1 in Ackermann et al. (2017). Since the discovery of this blazar and due to the fact of its high redshift, it has been the subject of multiwavelength studies for the last year, specially since *Fermi*-LAT detection (e.g., Li et al. (2018), Paliya et al. (2020), and Sahakyan et al. (2020)). From these studies, various properties related to variability and multiwavelength emission were revealed, as well as the estimate of logarithmic weight of the central black hole in solar masses derived from available optical spectroscopic information by using the so-called single epoch method (e.g., Vestergaard and Peterson (2006)). With a derived value of $\log M_{BH}/M_{\odot} = 8.7$ (Alam et al., 2015), it becomes apparent that a computation of the black hole mass using the complete spectrum energy is necessary when comparing it to other sources at a similar redshift as they show usually values higher than $M_{BH} > 10^9 M_{\odot}$.

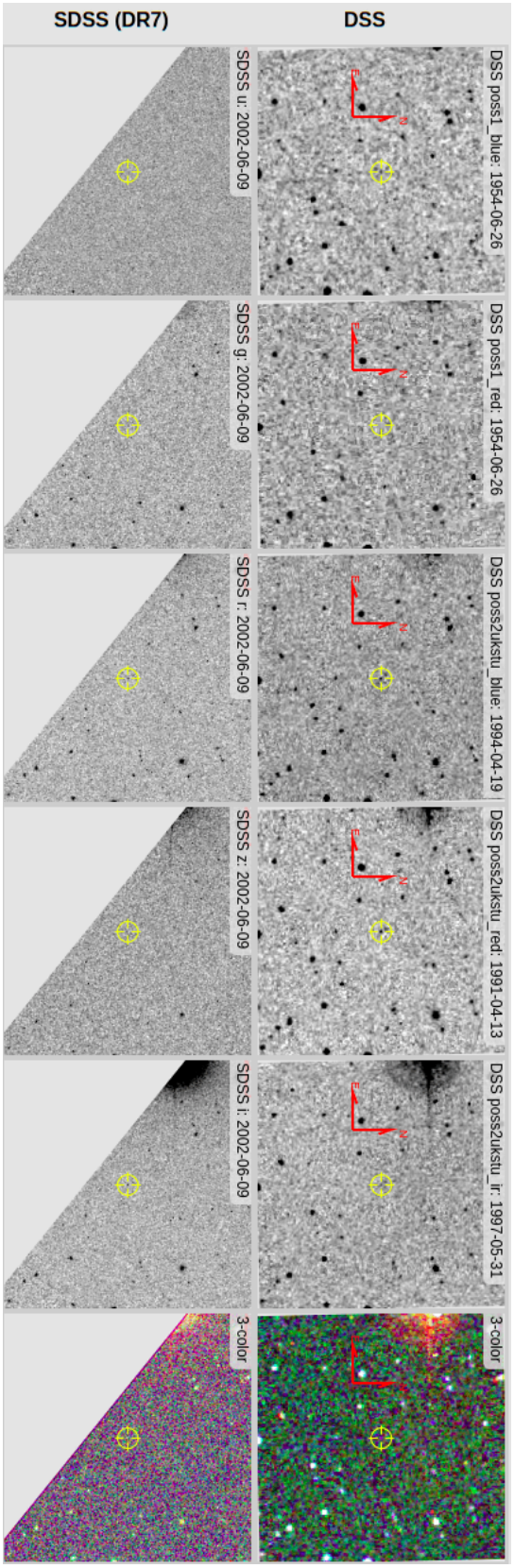

Figure 1.11. Images from both the Sloan Digital Sky Survey (SDSS) and the Digital Sky Survey (DSS) with a field of view of 298.8 arcsec, with target NVSS J163547+362930 at coordinates 16h 35m 47.23s + 36d 29m 30.1s (Equ J2000).

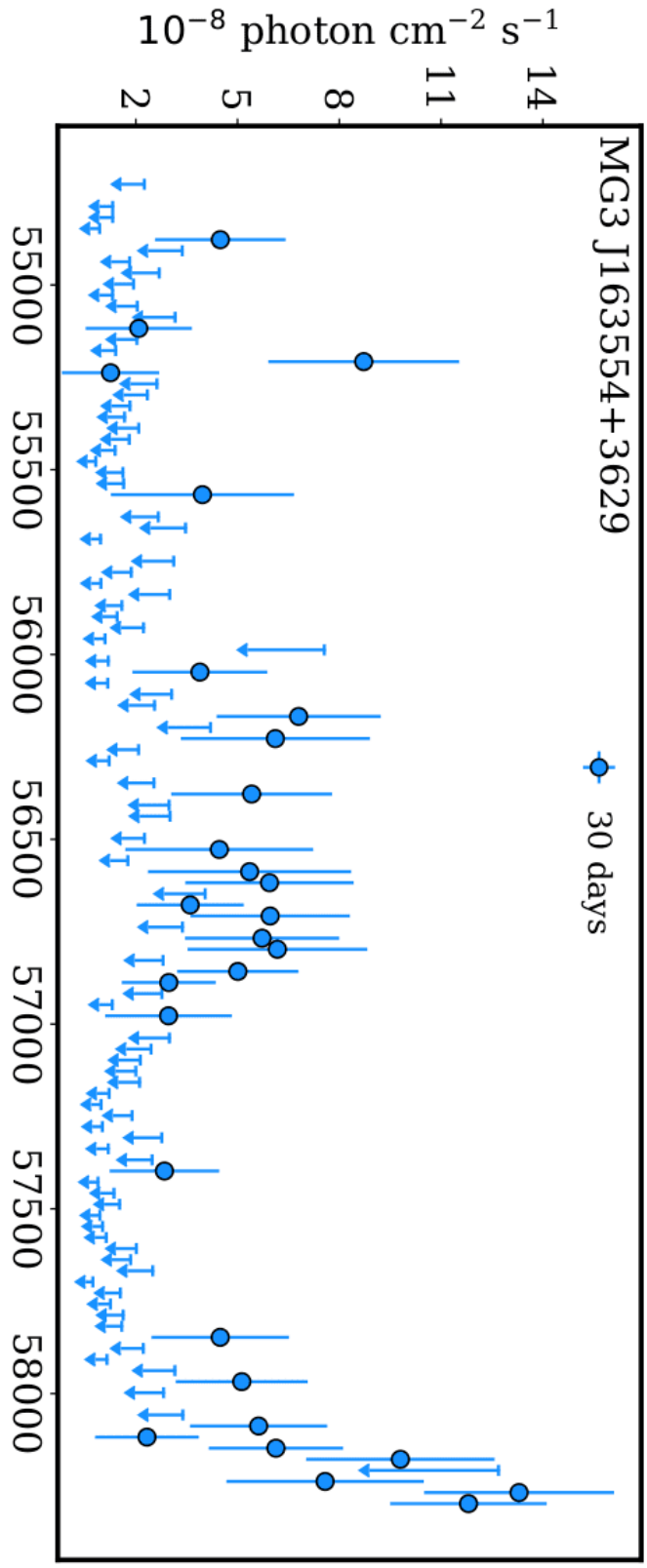

Figure 1.12. $\gamma-$ray light curve from the *Fermi*-LAT of NVSS J163547+362930 for the period from August 2008 to August 2018 calculated using 30-day binned light light curves. Figure taken from Sahakyan et al. (2020).

Chapter 2

Radiative Processes

This chapter will delve into the essential components of radiation that contribute to the SED of a blazar, elucidating their properties and mechanisms. Our focus will be on the phenomenon of free-electron scattering and generating radiation, with an emphasis on the underlying physical mechanisms, namely synchrotron radiation and the synchrotron self-Compton process. Additionally, we will examine how thermal radiation, such as radiated power from the accretion of plasma onto compact objects and radiation from the warm dusty torus, contributes to the SED.

2.1 Radiative Transfer

As discussed in Section 0.1, electromagnetic (EM) waves[1] provide us with a large amount of information from astrophysical sources, making it crucial to understand the underlying radiative processes to analyse various phenomena. Transfer theory provides a means of describing the behaviour of radiation when the size of a system is much larger than the wavelength of the radiation. This allows radiation to travel in straight lines, referred to as rays, through free space or uniform media. The frequency ν of photons is related to their wavelength λ through the speed of light c, which is a constant ($c = \lambda\nu$) with a value of 3.00×10^{10} cm/s in a vacuum. Additionally, energy $E = h\nu$ and temperature $T = E/k$ can be determined for each wavelength, where Planck's constant h is 6.625×10^{-27} erg s, and Boltzmann's constant k_B is 1.38×10^{-16} erg K^{-1}. Thus, the EM spectrum can be divided into various regions, as shown in Figure 2.1.

[1]It is now even possible to study some sources due to gravitational wave emissions (e.g., Abbott et al. (2016)).

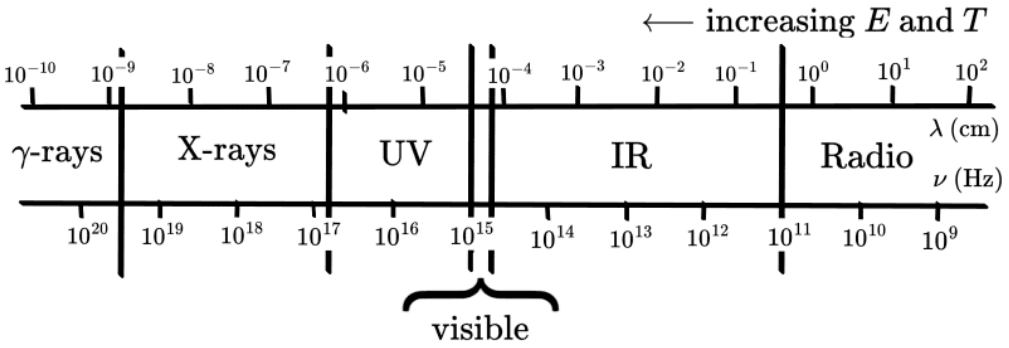

Figure 2.1. The EM spectrum. Distribution of electromagnetic waves with respect to frequency and wavelength, highlighting the visible part of the electromagnetic spectrum.

2.1.1 Fundamentals of Radiative Transfer

One of the most fundamental concepts of transfer theory is the energy flux. For example, consider an element of area dA exposed to radiation for a time dt: we define the energy passing through the element as simply proportional to $FdAdt$, where F is the energy flux measured in erg cm^{-2} s^{-1}. The energy passing through an element can also depend on its orientation.

Now, consider an isotropic radiation source (one that emits equally in all directions). If we surround the source with two spheres of radii r_1 and r_2 and assume the conservation of energy, the total energy passing through the first sphere should be the same as the energy passing through the outermost sphere:

$$\begin{aligned} F(r_1)A_1dt &= F(r_2)A_2dt \\ F(r_1)4\pi r_1^2dt &= F(r_2)4\pi r_2^2dt \\ F(r) &= \frac{F(r_1)r_1^2}{r^2} \end{aligned}$$

If we set fixed the first sphere we finally obtain the following result,

$$F = \frac{\text{constant}}{r^2} \tag{2.1}$$

indicating that the flux emitted from a source decreases like r^{-2}.

This flux is a measure of the energy carried by all rays passing through an element. If we want to know the energy carried by a single ray, we need to define the specific intensity or brightness I_ν to thus assign an infinitesimal value of the total energy to it. The energy crossing dA in dt time and in a frequency range $d\nu$ is then given by

$$dE = I_\nu dAdtd\nu d\Omega$$

where I_ν depends on the location in space, direction, and frequency.

In a radiation field, the net flux at some random orientation n of the small element dA can be obtained by integrating over all solid angles:

$$F_\nu = \int I_\nu \cos\theta d\Omega \tag{2.2}$$

where θ is the angle between the normal of dA and the direction of the flux (see Figure 2.2). It is clear that for an isotropic radiation field, the same amount of energy crosses in the n and $-n$ directions, which means $F_\nu = 0$. F_ν is also known as the first radiative moment. Recalling that the momentum of a photon is E/c, it is possible to obtain the second radiative moment, the momentum flux p_ν. As the momentum is proportional to the photon's energy, we can then write:

$$dp_\nu = \frac{dE}{c}$$
$$dp_\nu = \frac{1}{c} F_\nu \cos\theta d\Omega$$

obtaining as a final result

$$p_\nu = \frac{1}{c} \int I_\nu \cos^2\theta d\Omega \tag{2.3}$$

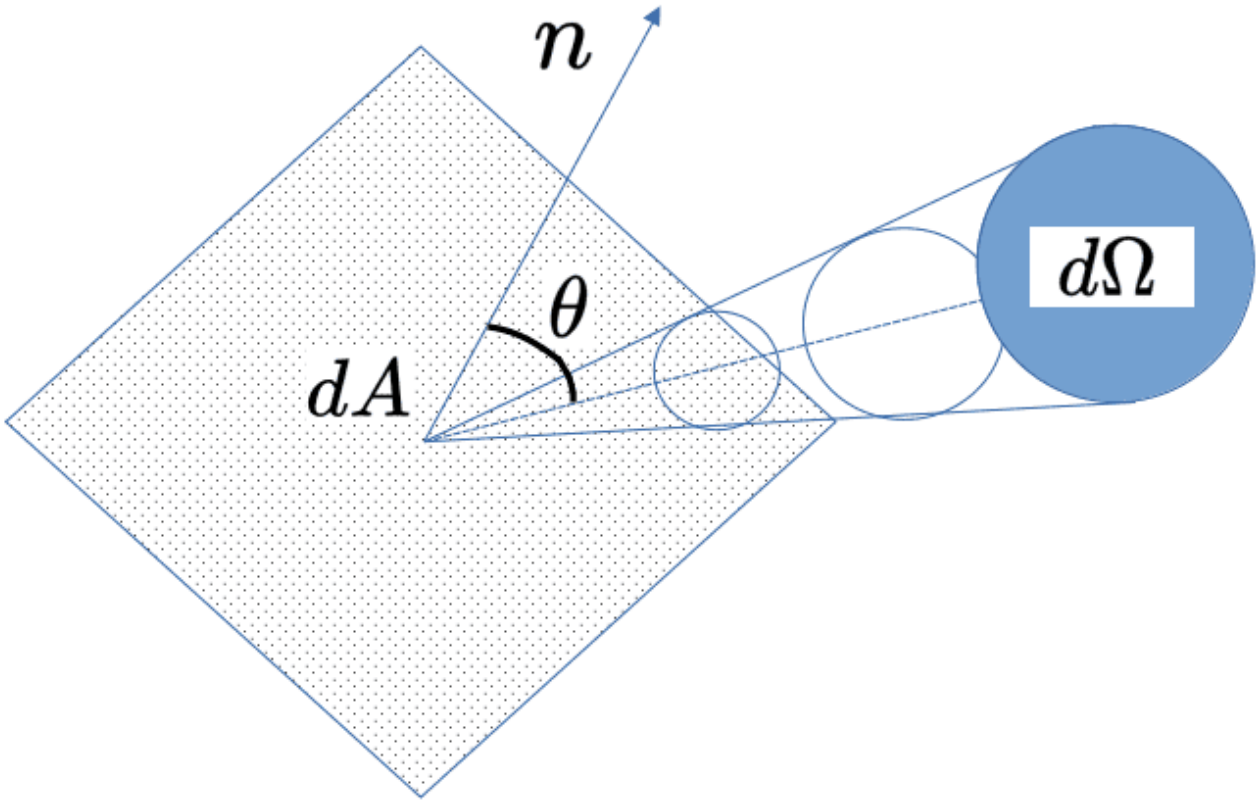

Figure 2.2. Geometry for incident rays passing through an element dA

It is also possible to talk about the specific energy density u_ν defined just as the unit per unit volume per frequency range. To better understand u_ν we can assume a cylinder of length $ds = cdt$ where dt is the time it takes light to pass through the cylinder. The volume of the cylinder dV is then $dAcdt$ which can be used to obtain u_ν,

$$dE = I_\nu dAdtd\nu d\Omega = u_\nu(\Omega)dV = u_\nu(\Omega)dAcdtd\nu d\Omega$$

obtaining from these relations

$$u_\nu(\Omega) = \frac{I_\nu}{c}$$

which if we integrate through all solid angles yields

$$u_\nu = \frac{1}{c}\int I_\nu d\Omega = \frac{4\pi}{c}J_\nu \tag{2.4}$$

where J_ν is defined as the mean intensity.

2.1.2 Radiative Transfer Equation

As radiation passes through matter, it can gain or lose energy, depending on the conditions. Let us first consider the case where an object gains energy from incoming radiation; for this to occur, the object must absorb rays, which results in a loss of the rays' intensity. The change in I_ν can then be written as:

$$dI_\nu = -\alpha_\nu I_\nu ds \tag{2.5}$$

where α_ν is the specific absorption coefficient with units cm^{-1} and ds is the distance in which we see this change. Another way to understand this is to imagine the radiation passing through a box full of particles with density n and with a cross section σ_ν. If the box has a $dV = dAds$, the total number of particles, absorbers, is just $ndAds$, or a total absorption area of $n\sigma_\nu dAds$. Thus, the energy absorbed by the beam is

$$dE = -I_\nu dAdtd\nu d\Omega = I_\nu(n\sigma_\nu dAds)td\nu d\Omega$$

giving as a result that

$$dI_\nu = -n\sigma_\nu I_\nu ds$$

which, if computed with Equation 2.5 gives us

$$\alpha_\nu = n\sigma_\nu \tag{2.6}$$

where σ_ν can also be written in terms of the mass absorption coefficient k_ν and the density of the system.

On the other hand, for the process of energy loss, which arises from radiation emission, we define the spontaneous monochromatic emission coefficient j_ν as the energy emitted per unit of time and unit volume:

$$j_\nu = \frac{dE}{dV dt d\nu d\Omega}.$$

In the most general case for an isotropic source, we can take the integral over all solid angles to thus get the total radiated power per unit volume per unit frequency

$$\frac{dE}{dV dt d\nu} = P_\nu = 4\pi j_\nu. \tag{2.7}$$

By defining a new parameter called emissivity e_ν as the spontaneous energy emitted per unit frequency per unit time per unit mass, namely, erg g^{-1} s^{-1} Hz^{-1}, and applying the same method as the one used to get Equation 2.6, we get

$$dI_\nu = j_\nu ds. \tag{2.8}$$

in which the relation between e_ν and j_ν is simply

$$j_\nu = \frac{e_\nu \rho}{4\pi} \tag{2.9}$$

where ρ is the mass density of the emitting medium.

Using what we have discussed so far, it is now possible to write an equation that explains how the incoming radiation changes when passing through a medium. As the beam will eventually suffer gains and losses, we find that our transfer equation can be written as

$$\frac{dI_\nu}{ds} = j_\nu - \alpha_\nu I_\nu \tag{2.10}$$

Finally, the last relevant component of the properties of the system must be named: the optical depth τ_ν. Defined as

$$d\tau_\nu = \alpha_\nu ds \tag{2.11}$$

will tell us if the medium is thick or thin. Whenever the integral of τ_ν along a length is greater than 1, we say that the medium is thick or opaque. This means that photons of frequency ν cannot completely traverse the medium. On the other hand, if the integral of τ_ν is less than one, we say that the medium is thin or transparent, and photons of frequency ν can traverse the entire medium. If we substitute Equation 2.11 into Equation 2.10 and add a source function S_ν, defined as the ratio between the emission and the absorption coefficient,

we get:

$$\boxed{\frac{dI_\nu}{d\tau_\nu} = S_\nu - I_\nu}. \tag{2.12}$$

It is now obvious that any change in the radiation emitted will depend only on the properties of the source, that is, in S_ν. In the most general scenarios, it is possible to solve Equation 2.12 quite simply considering only emission or absorption processes; however, this is out of the scope of this work. More detailed and rigorous treatments are given in the literature (e.g., Longair (2011) and Rybicki and Lightman (1991)).

2.2 Radiation by Moving Charges

We have already discussed (§ 1 maybe something else) the processes in which charged particles, specifically electrons, gain energy in the jet environment. It is now time to discuss the cooling processes and the different dependences on energy for each. We will work on our way to cover the energy distribution of electrons in an ascending way.

To understand the radiation emitted by a charged moving particle, illustrated in Figure 2.3, we need to study the electromagnetic effects that this will produce. For this, we must use the Liénard-Wiechert potentials. The reader can refer to the literature to see the full derivation of the potentials and fields (e.g., Jackson (1977), Longair (2011)).

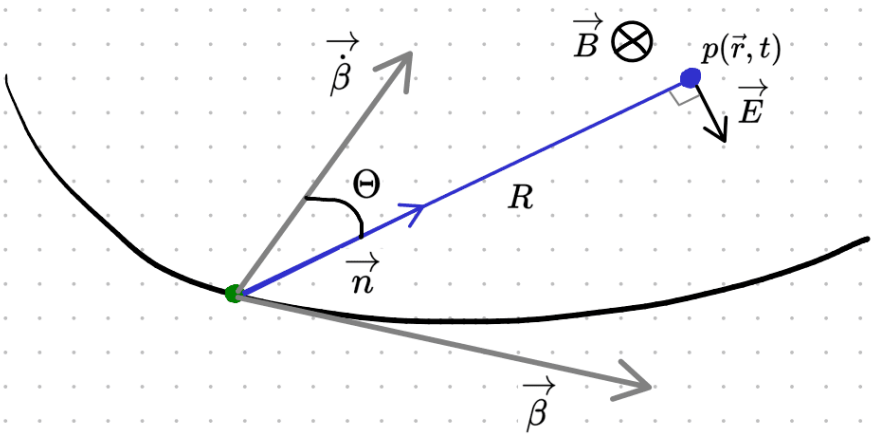

Figure 2.3. The diagram illustrates the trajectory of a negatively charged particle (depicted as a green dot) as it moves along a given path (shown in black). The grey arrows indicate the direction of both the particle's velocity and acceleration. At a point $p(\vec{r},t)$ at a distance of R (indicated by the blue line) from the charged particle along the direction of the vector $\mathbf{n}$, it is possible to measure both the magnetic and electric fields (denoted B and E, respectively). The crossed circles indicate that the direction of B is directed into the page.

In a general picture, the Liénard-Wiechert fields at a distance $\vec{r}$ and a time t are

$$\vec{E}(\vec{r},t) = q\Big[\frac{(\vec{n}-\vec{\beta})(1-\vec{\beta^2})}{k^3R^2}\Big] + \frac{q}{c}\Big[\frac{\vec{n}}{k^3R} \times \big((\vec{n}-\vec{\beta}) \times \dot{\vec{\beta}}\big)\Big] \tag{2.13a}$$

$$\vec{B}(\vec{r},t) = \big[\vec{n} \times \vec{E}(\vec{r},t)\big] \tag{2.13b}$$

where $\vec{\beta}$ is defined as $\vec{u}/c$ (being $\vec{u}$ the velocity of the particle), q its charge and k just the difference between 1 and the scalar product of $\vec{n}$ and $\vec{\beta}$. It can also be seen that the Equation 2.13a is conformed by two parts: the first term that scales like R^{-2} is called the radiation field (a generalisation of Coulomb's law), while the right hand of it is called the radiation field. As in fact $\vec{B}$ is always perpendicular to $\vec{E}$, we will put more effort into analysing its counterpart.

2.2.1 Radiation Emitted in the Non-Relativistic regime

The first thing we can observe from Equation 2.13a is that closer to the moving particle the electromagnetic effects will be dominated by the radiation field. Also, it is easy to show that in the non-relativistic regime ($\beta \ll 1$) the radiation field will be the dominant factor. For the latter case, using Equations 2.13, the magnitudes of E and B are

$$E = B = \frac{q\dot{\beta}}{Rc}\sin\Theta. \tag{2.14}$$

The electric field component mentioned denotes a burst of electromagnetic radiation, and therefore the amount of energy transmitted per unit area per unit time at distance r is equivalent to the Poynting vector's magnitude. This Poynting vector S in the direction of $\vec{n}$ has the magnitude:

$$S = |\vec{E} \times \vec{B}| = \frac{E^2c}{4\pi} = \frac{c}{4\pi}\frac{q^2\dot{\beta}^2}{R^2c^2}\sin^2\Theta \tag{2.15}$$

Consequently, the amount of energy that flows through the area $r^2d\Omega$, which is the area of a sphere contained by a solid angle $d\Omega$ at an angle θ and a distance R from the charge, in a given time, can be determined by

$$P = \frac{dW}{dt} = SdA = SR^2d\Omega = \frac{q^2\dot{\beta}^2}{4\pi c}\sin^2\Theta d\Omega. \tag{2.16}$$

Finally, by integrating Equation 2.16, the total power emitted by the moving charge, into all solid angles we have the following.

$$\boxed{P = \frac{2q^2\dot{\beta}^2}{3c} = \frac{2q^2a^2}{3c^3}} \tag{2.17}$$

where a is the magnitude of the acceleration vector. Equation 2.17 is also known as Larmor's formula.

Equation 2.17 shows that when a charged particle undergoes acceleration, it emits radiation whose power is directly proportional to the square of both the acceleration and the charge. Furthermore, the direction of E is determined by the vectors u and n: if the particle accelerates along a particular line, the resulting radiation will be entirely linearly polarised in the u and n plane.

2.2.2 Radiation Emitted in the Relativistic Regime

Now it is time to show how moving charges in the relativistic regime ($\beta \sim 1$) will emit radiation. This can be achieved by using transformations between different inertial frames: the lab frame (not primed) and an instantaneous rest frame (primed), in which the particle is at rest. In the latter case, it is easy to see that the momentum emission is zero (i.e. $dp' = 0$), so we can transform the energy from the primed frame to the lab frame as

$$dW = \gamma dW',$$

where γ^2 is the well-known Lorentz factor $\gamma = (\sqrt{1-\beta^2})^{-1}$. As expected, if the time dilatation formula is taken into account, it is straightforward to see that the amount of power emitted in both frames is the same[3] ensuring Lorentz invariance in the scalar quantity. Thus, it is possible to see that in the particle's frame, using Equation 2.17, P' will simply be

$$P' = \frac{2q^2 a'^2}{3c^3} \tag{2.18}$$

using the fact that a'^2 can be written as a four-vector product and that the particle can be considered at rest, so $a'_0 = 0$. Thus, we can substitute our last equation with its covariant form:

$$P' = \frac{2q^2}{3c^3}\left(\vec{a'} \cdot \vec{a'}\right) \tag{2.19}$$

We will differentiate the acceleration components that align with the velocity, denoted as $a'_{\parallel}$, from that perpendicular to it, denoted $a'_{\perp}$. These components undergo boost transformations as

$$a'_{\parallel} = \gamma^3 a_{\parallel} \qquad \text{and} \qquad a'_{\perp} = \gamma^2 a_{\perp} \tag{2.20}$$

[2]In literature, the letter Γ is commonly utilized to denote the bulk Lorentz factor of the blob for the purpose of modelling the SED.

[3]As $dt = \gamma dt'$, if dW/dt is computed we will have that $dW/dt = (\gamma/\gamma)dW'/dt' = dW'/dt'$ showing that in both frames the power emitted is equal.

Now it is possible to substitute in Equation 2.19 to obtain the following.

$$\boxed{P = \frac{2q^2}{3c^3}\gamma^2\left(\gamma^2 a_{\parallel}^2 + a_{\perp}^2\right)}, \tag{2.21}$$

where the emitted fluxes are affected by a beaming factor δ such as

$$\delta = \frac{1}{\gamma(1 - \beta\cos\theta)}. \tag{2.22}$$

It is also possible to explain and understand the angular distribution of the radiation emitted across a solid angle $d\Omega' = sin\theta' d\theta' d\phi' = d\mu' d\phi'$ by using Lorentz transformations and the popular formula for aberration of the angular region:

$$\mu = \frac{\mu' + \beta}{1 + \beta\mu'} \qquad \text{or} \qquad d\mu = \frac{d\mu'}{\gamma^2(1 + \beta\mu')^2}. \tag{2.23}$$

As the Lorentz boost is orthogonal to the azimuthal direction, this last equation can be generalised to any solid angle ($d\phi' = d\phi$) and so

$$\begin{aligned} d\Omega = d\mu d\phi &= \frac{d\mu'}{\gamma^2(1 + \beta\mu')^2} d\phi' \\ d\Omega &= \frac{d\Omega}{\kappa^2} \end{aligned} \tag{2.24}$$

where $\kappa^2 > 1$ makes the solid angle in the lab frame smaller than in the particle frame. This phenomenon called the beaming effect, can also be seen in Figure 2.4.

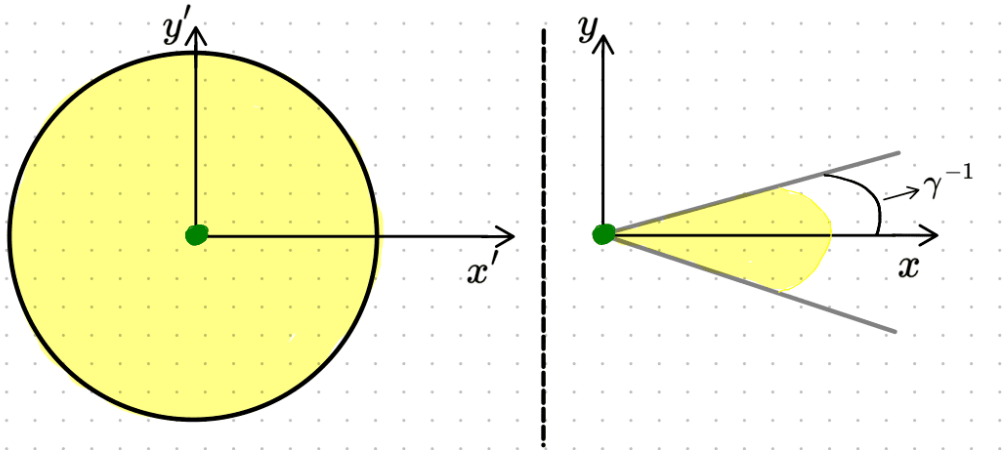

Figure 2.4. When a charged particle moves towards the x-direction in a non-primed frame, radiation emitted isotropically in its instantaneous rest frame undergoes relativistic beaming. To prevent ambiguous values of the solid angle at high γ values, the beam should have an opening angle θ of $1/\gamma$.

2.3 Synchrotron Radiation

When particles are accelerated by a magnetic field, they emit radiation. In the non-relativistic regime, the radiation emitted is called cyclotron radiation, and its frequency is simply the frequency of their gyration in the magnetic field, namely:

$$\nu_B = \frac{qB}{2\pi m} \tag{2.25}$$

where m is simply the mass of the charged particle. However, for particles with extreme relativistic velocities, the frequency spectrum of the radiation emitted is much more complex and can extend many times the gyration frequency. This type of radiation is known as synchrotron radiation and it is responsible for the nonthermal continuum optical emission of blazars. It is also responsible for the radio emission of our Galaxy, supernova remnants, and extragalactic radio sources. As discussed in the literature (e.g., Blumenthal and Gould (1970), Longair (2011), and Rybicki and Lightman (1991)), the total energy loss rate can be calculated using Liénard-Wiechert potentials, allowing us to use the formulas discussed earlier.

2.3.1 Total Energy Loss Rate

To obtain the total energy loss for a single relativistic charged particle in a uniform magnetic field, first we need to understand the motion of the particle, which can be achieved using the Lorentz force. As visible in Figure 2.5, when a charged particle moves through a magnetic field, it experiences a force that is perpendicular to both the magnetic field and the direction of its velocity. This force causes the particle to move in a circular path around the field lines of the magnetic field. So, the equation of motion of a particle of mass m is dictated by

$$\frac{d\vec{p}}{dt} = \frac{d}{dt}(\gamma m\vec{u}) = \frac{q}{c}\big(\vec{u} \times \vec{B}\big) \tag{2.26}$$

while for the time component, we have

$$\frac{d\vec{w}}{dt} = \frac{d}{dt}(\gamma mc^2) = q\big(\vec{u} \cdot \vec{E}\big) = 0 \tag{2.27}$$

An important result arises from this last equation, as it shows $\gamma = \text{cte}$, meaning the energy is conserved. Thus, it is possible to write Equation 2.26 as

$$\gamma m\frac{d\vec{u}}{dt} = \frac{q}{c}\big(\vec{u} \times \vec{B}\big). \tag{2.28}$$

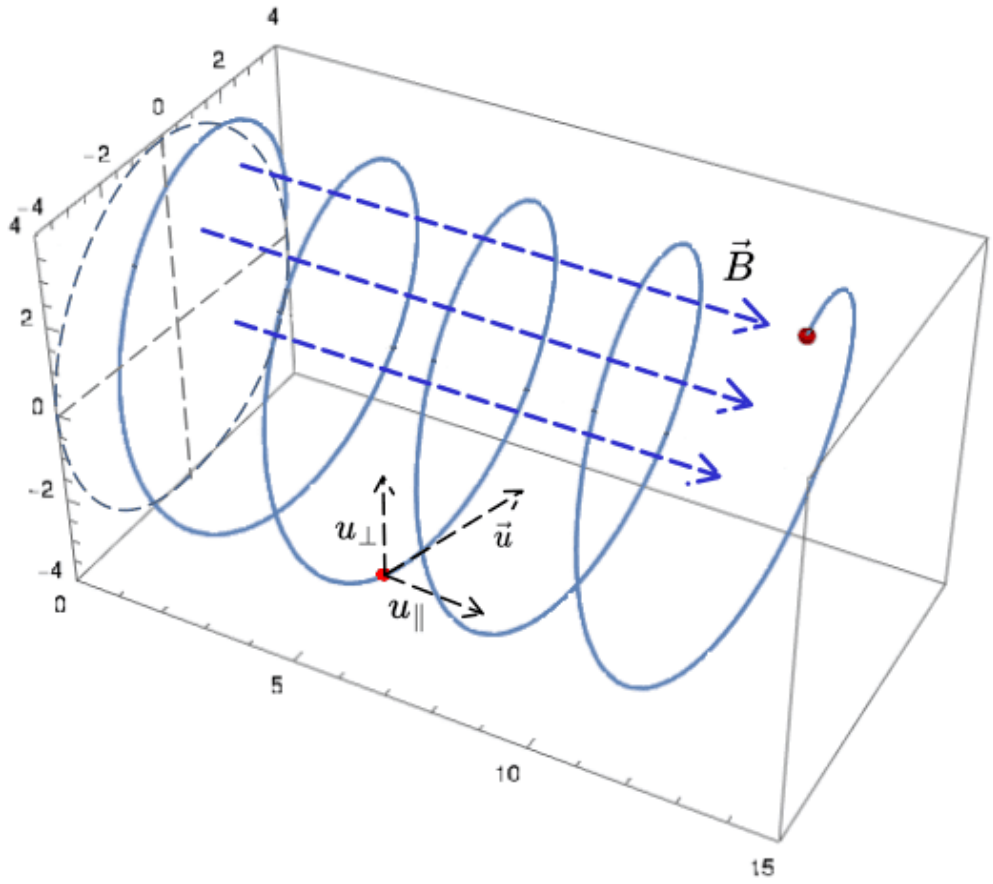

Figure 2.5. Helical motion (blue continuous line) of a positively charged particle in a uniform electromagnetic field $\vec{B}$(blue dashed arrows). It is also possible to deconstruct the velocity $\vec{u}$ into its two components: $u_\parallel$ parallel to $\vec{B}$, and $u_\perp$ perpendicular to it.

As the particle travels along the direction of the magnetic field, it is easy to see that only the $u_\perp$ component of the velocity will be affected, and also by the fact that it is perpendicular to $\vec{B}$ we have

$$a_\perp = \frac{q}{\gamma mc} u_\perp B = \frac{u_\perp^2}{R} \qquad \text{and} \qquad a_\parallel = 0, \tag{2.29}$$

as it must also be the same as the centripetal force. Thus, by substituting this last equation with the $u_\perp = \omega R$ we have that the angular gyrofrequency is

$$\omega = \frac{qB}{\gamma mc}. \tag{2.30}$$

Finally, if we substitute Equation 2.29 in Equation 2.21 for a single electron, we get

$$P(\alpha) = \frac{2}{3}\gamma^2 r_0^2 c\beta^2 B^2 \sin^2\alpha \tag{2.31}$$

where α is the angle between the velocity and $\vec{B}$, which is called the pitch angle, and r_0 is the

classical particle radius defined as:

$$r_0 = \frac{q^2}{mc^2} \tag{2.32}$$

It is also possible to write the total emitted power by substituting the magnetic field factor B^2 with the magnetic energy density $U_B = B^2/8\pi$. If we now take the average synchrotron power per electron, considering that over time the distribution of their pitch angles becomes isotropic due to magnetic fluctuations and scattering processes,

$$\langle \sin\alpha \rangle \equiv \frac{\int \sin^2\alpha d\Omega}{d\Omega} = \frac{2}{3},$$

the average synchrotron power in an isotropic relativistic distribution of electrons is,

$$\boxed{P_{\text{synch}} = \frac{4c\sigma_T}{3}\gamma^2\beta^2 U_B} \tag{2.33}$$

where σ_T is the Thomson cross section which is equal to $\frac{8\pi}{3}r_0^2$ (see§ 2.4).

2.3.2 Synchrotron Spectrum

The relationship between the variation in $\vec{E}$ and the spectrum of synchrotron radiation is essential for the perception of the observer. As discussed in Section 2.2.2, synchrotron radiation fields are emitted in a limited range of directions around the particle's velocity, known as beaming effects. This leads to a radiation pulse that is confined to a significantly shorter time interval than the gyration period. It is well known that the width of the observed pulse is γ^3 times smaller than the gyration period. By utilising the dependence of the electric field on θ solely through the $\gamma\theta$ combination, we can obtain a significant amount of information about the spectrum. Expressing $\vec{E}$ as proportional to the function $F(\gamma\theta)$, with t representing time measured in the observer's frame, allows us to achieve this. Therefore, knowing the relation between θ and t helps to understand the spectrum.

$$\gamma\theta \sim 2\gamma^3\omega \sin\alpha t \propto \omega_c t \tag{2.34}$$

in which ω_c is defined as a critical frequency, we can write down the relation between $\vec{E}$ and t like:

$$E(t) \propto g(\omega_c t) \tag{2.35}$$

in which ω_c refers to the frequency at which the emitted radiation is the brightest or has the highest intensity. This ω_c will roughly be around the cutoff point of the spectrum.

Now, recalling Equations 2.15 & 2.17, and using Parseval's theorem, telling us that the total energy of a signal is equal to the total energy of its Fourier transform, we can rewrite

the radiated power per solid angle to be

$$\frac{dW}{d\omega d\Omega} \propto |\widehat{E}|^2.$$

If we divide this power by the orbital period and integrate it over the solid angle, we get an averaged power per unit frequency that will depend only on the ratio ω/ω_c

$$P(\omega) = \frac{\sqrt{3}}{2\pi}\frac{q^3 B \sin\alpha}{mc^2} F\Big(\frac{\omega}{\omega_c}\Big) \tag{2.36}$$

where F is a dimensionless function given by

$$F(x) \equiv \int_x^\infty K_{\frac{5}{3}}(v)dv. \tag{2.37}$$

in which $K_{\frac{5}{3}}$ is a modified Bessel function. Equation 2.37, as seen in Figure 2.6, reaches a maximum of around 0.29, with a value close to 1 means that the pinnacle of synchrotron radiation is around $\omega \approx 0.29\omega_c$. The asymptotic values for large and small values of ω/ω_c are

$$F(x) \sim \begin{cases} \Big(\frac{\pi}{2}\Big)^{\frac{1}{2}} \exp^{-x} x^{\frac{1}{2}}, & \text{if } \omega \gg \omega_c \\ \\ \frac{4\pi}{\sqrt{3}\Gamma\big(\frac{1}{3}\big)}\Big(\frac{x}{2}\Big)^{\frac{1}{3}}, & \text{if } \omega \ll \omega_c \end{cases} \tag{2.38}$$

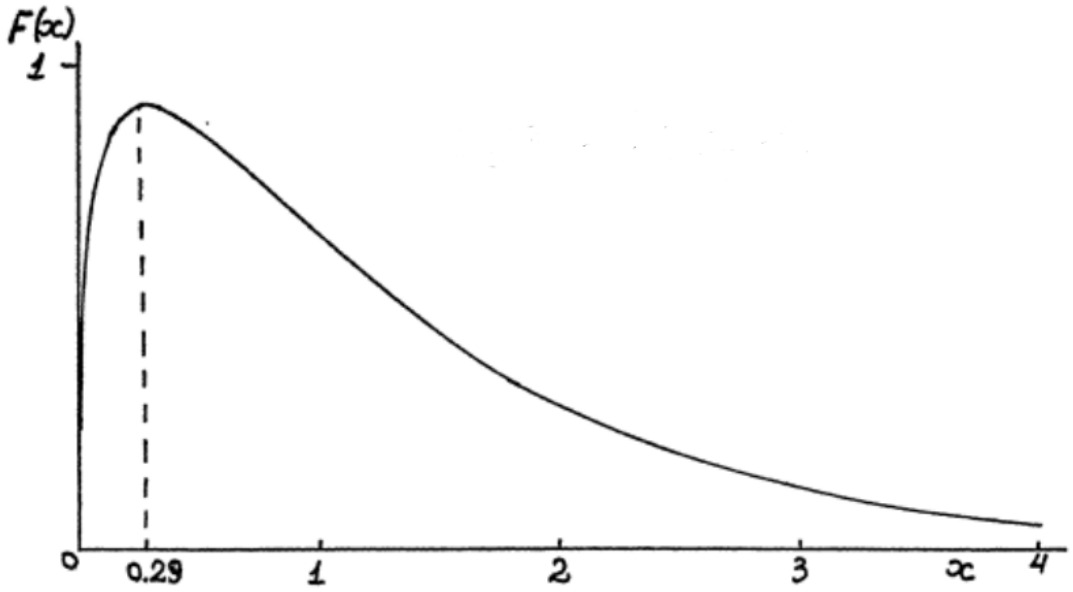

Figure 2.6. Synchrotron spectral distribution (over all solid angles) for a single electron in terms of $F(x)$ where $x \equiv \omega/\omega_c$. Plot taken from Ginzburg and Syrovatskii, 1965, p. 311.

Now, for a power-law distribution of relativistic electrons (see Equation 1.6, if we use $E = \gamma mc^2$, it is possible to write down the distribution as

$$N(\gamma)d\gamma = K\gamma^{-p}d\gamma \tag{2.39}$$

where K is our normalisation constant. The total power per unit volume per unit frequency $P_{\text{tot}}(\omega)$ will be given by the integral of Equation 2.39 times Equation 2.36. Thus, we have that

$$P_{\text{tot}} \propto \omega^{-(p-1)/2} \int_{x_1}^{x_2} F(x)x^{(p-3)/2}dx \propto \omega^{-(p-1)/2} \tag{2.40}$$

where the limits $x_1 \approx 0$ and $x_2 \approx \infty$. These limits are those that would correspond to γ_1 and γ_2 dependent on ω. Meaning that the spectral index s is related to p as

$$s = \frac{p-1}{2}, \tag{2.41}$$

i.e., it is possible to obtain the synchrotron spectrum from the electron distribution and the other way around.

2.3.3 Synchrotron Self Absorption

The process of synchrotron emission involves not only the emission of photons but also their absorption. When a photon interacts with a charge in a magnetic field, it relinquishes its energy to the charge. Moreover, stimulated emission can occur whereby a particle is induced to emit more strongly in a direction and at a frequency where photons are already present. The Einstein coefficients A and B represent emission and absorption, respectively, and are linked. It can be demonstrated that the emission particle's states correspond to its free particle states, which are determined by its position, momentum, and internal state. According to statistical mechanics, the translational degrees of freedom of a particle in a phase space volume of magnitude h^3 correspond to one quantum state. Therefore, we divide the continuous classical phase space into elements of h^3 size and treat the transitions between these elements as transitions between discrete states. If a photon has a specific energy of $h\nu$, there can be numerous transitions between states that differ in energy by an amount $h\nu$. Thus, in the formula for calculating the absorption coefficient, we must sum over all possible upper states (designated as 2) and lower states (designated as 1) that participate in the transition.

$$\alpha_\nu = \frac{h\nu}{4\pi} \sum_{E_1} \sum_{E_2} \Big[n\big(E_1\big) B_{12} - n\big(E_2\big) B_{21} \Big] \phi_{21}(\nu) \tag{2.42}$$

where the profile function $\phi_{21}(\nu)$ is essentially a function δ that restricts the states outside the gap $h\nu = E_2 - E_1$, while $n\big(E_1\big)$ and $n\big(E_2\big)$ are the respective number densities of the two energy states. In Equation 2.42 the first term will represent true absorption, as the particles go to a higher energetic level, while the second term represents stimulated emission, as the particle goes to a lower energetic level.

It is also possible to write the radiated power in terms of ν rather than ω simply by using $P(\nu) = 2\pi P(\omega)$. Thus, using Equation 2.7 we will have

$$P_\nu = 4\pi j_\nu = h\nu \sum_{E1} A_{21}\phi_{21}(\nu) \tag{2.43}$$

where the emission coefficient is written in terms of the Einstein coefficients. Now, taking into account the detailed balance relations (which state that the rate of absorption of energy by a particle from radiation at a given frequency is equal to the rate of emission of energy by that same particle at the same frequency), it is possible to use Equations 2.42 and 2.43 to write α_ν in terms of $j\nu$ so that a source function S_ν can be computed. For an isotropic relativistic power-law distribution of particles (Equation 2.39), it can be shown that, expanding in a power series around (E), the absorption coefficients read approximately as

$$\alpha_\nu \sim (p+2)\frac{c^2}{8\pi h\nu^2}\int \frac{N(E)}{E} P_\nu dE \tag{2.44}$$

which for the power radiated by a single charge (using Equation 2.36) yields

$$\alpha_\nu \propto \nu^{-(p+4)/2}. \tag{2.45}$$

Then, the source function can be simply found by computing

$$S_\nu = \frac{j_\nu}{\alpha_\nu} = \frac{P_\nu}{4\pi\alpha_\nu} \propto \frac{\nu^{-(p-1)/2}}{\nu^{-(p+4)/2}} \propto \nu^{5/2} \tag{2.46}$$

which is independent of the index p. In the case of optically thin synchrotron emission, the observed intensity is directly proportional to the emission function. On the other hand, in the case of a thick optical emission, the observed intensity is proportional to the source function. For the nonthermal power-law electron distribution, the emission and source functions are proportional to $\nu^{-(p-1)/2}$ and $\nu^{5/2}$, respectively. Therefore, the optically thick region occurs at low frequencies, leading to a low-frequency cutoff in the observed spectrum. This result can be better seen in Figure 0.2 which represents the SED of a blazar using exclusively the synchrotron and SSC parameters of a leptonic model. A more detailed and vigorous treatment is given in the literature, e.g., Ginzburg and Syrovatskii (1965), Longair (2011), and Rybicki and Lightman (1991).

2.4 Inverse-Compton Scattering

Whenever a photon interacts with an electron, a scattering process may take place. The energy exchange during this event will depend mostly on the ratio of the energies between the photon and the electron. For instance, for photons with energies lower than the electron rest mass, $h\nu \ll mc^2$, namely, in the non-relativistic regime, the scattering of radiation, for unpolarized incident radiation, reduces to the Thomson scattering case:

$$\begin{aligned} \frac{d\sigma_T}{d\Omega} &= \frac{1}{2} r_0^2 (1 + \cos^2\theta) \\ \sigma_T &= \frac{8\pi r_0^2}{3}, \end{aligned} \tag{2.47}$$

where r_0 is the classical electron radius with a value of 2.82×10^{-13} cm, θ is the scattered angle of the radiation, and σ_T is the well-known Thomson cross section $\approx 0.665 \times 10^{-24}$ cm^2. These interactions occur mainly between photons and electrons. This is because in this energy range, the cross section for a proton is significantly smaller than that for an electron. This can be shown simply by computing the ratio between the cross section of the proton and the electron. This ratio is solely dependent on their classical radius, Equation 2.32, and, consequently, on their mass, as both protons and electrons have the same charge:

$$\frac{\sigma_{T-p}}{\sigma_{T-e}} = \left(\frac{m_e}{m_p}\right)^2 \sim 10^{-7}, \tag{2.48}$$

meaning we can completely neglect protons when considering these interactions.

It is quite simple to prove that, in this energy regime, using energy and momentum conservation, the photon energy posterior to the interaction ϵ_1 is

$$\epsilon_1 = \frac{\epsilon}{1 + \dfrac{\epsilon}{mc^2}(1 - \cos\theta)} \tag{2.49}$$

while ϵ is the energy a priori. From this last equation, it is easy to see that for all possible values of $\theta, \epsilon_1 < \epsilon$. However, in quantum electrodynamics, the differential cross section for unpolarized radiation is given by the Klein-Nishina (KN) formula

$$\frac{d\sigma_{KN}}{d\Omega} = \frac{r_0^2 \epsilon_1^2}{2\epsilon^2}\left(\frac{\epsilon}{\epsilon_1} + \frac{\epsilon_1}{\epsilon} - \sin\theta\right) \tag{2.50}$$

from which it is possible to prove that in the relativistic regime, $h\nu \gg mc^2$, the cross-section for the process is smaller than σ_T; i.e., Compton scattering becomes less efficient at higher

energies (see Figure 2.7). The total section can be shown to be:

$$\sigma_{KN} = \sigma_T \frac{3}{4}\left[\frac{1+x}{x^3}\left(\frac{2x(1+x)}{1+2x} - \ln 1+2x\right) + \frac{1}{2x}\ln 1+2x - \frac{1+3x}{(1+2x)^2}\right] \tag{2.51}$$

where $x = h\nu/mc^2$. Different results are obtained for the relativistic and nonrelativistic regimes:

$$\sigma_{KN} \approx \begin{cases} \sigma_T\left(1 - 2x + \dfrac{26x^2}{5} + \dots\right), & \text{if } x \ll 1. \\ \dfrac{3}{8x}\sigma_T\left(\ln 2x + \dfrac{1}{2}\right), & \text{if } x \gg 1. \end{cases} \tag{2.52}$$

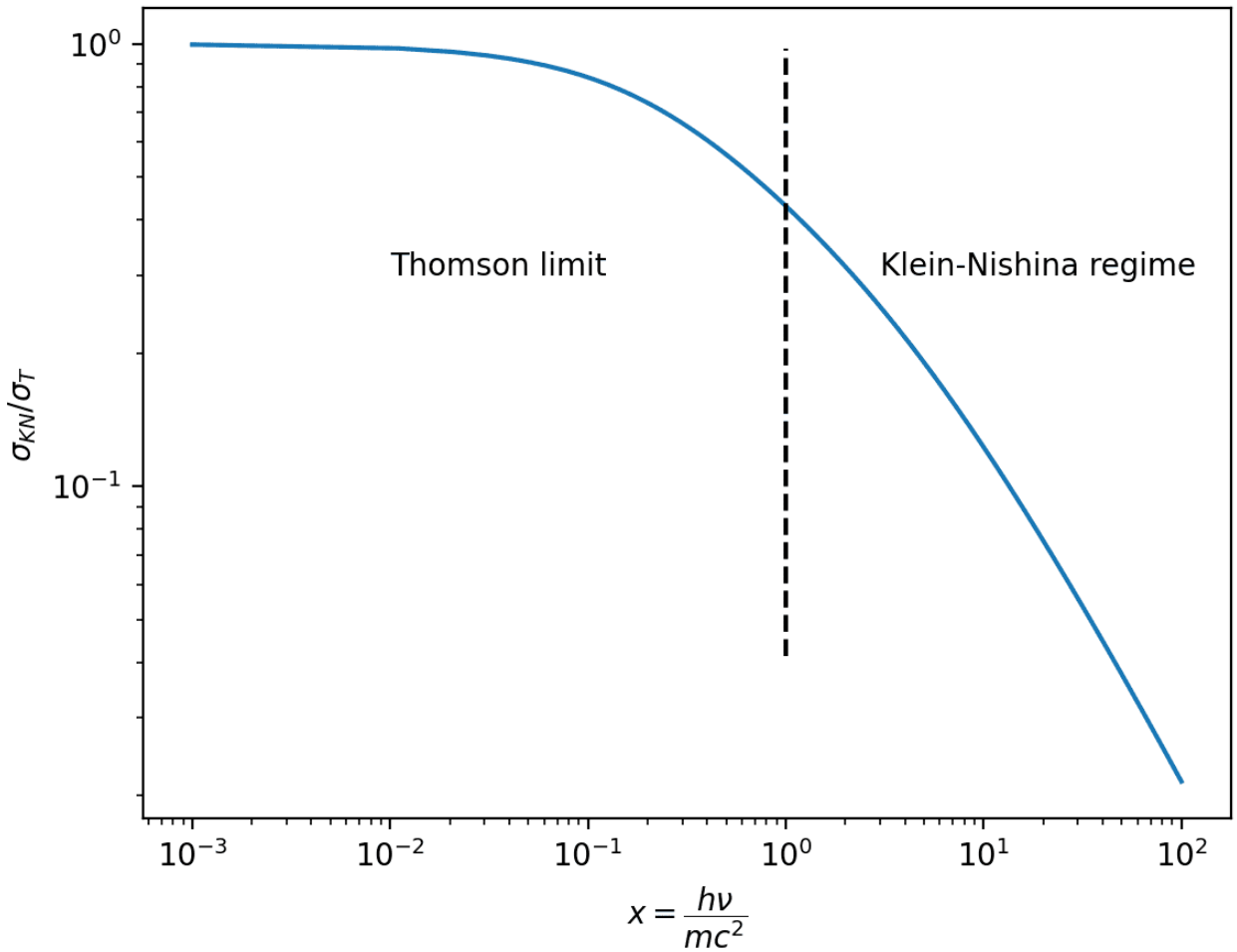

Figure 2.7. The Klein-Nishina (KN) formula is utilised to determine the overall cross-sectional area for Compton scattering. At low energy levels where $x \ll 1$, the cross section remains close to σ_T; however, when the effects of KN become significant at high energy levels where $x > 1$, the cross section diminishes.

For the case in which the moving electrons have a greater energy than the photon energy, net energy will be transferred from the electrons into the radiation field. This process is also known as inverse Compton scattering (ICS). As these electrons are relativistic, a treatment between the electron rest frame and the lab frame is required. The geometries for ICS can be seen in Figure 2.8, where the primed system refers to the electron rest frame and the non-primed one to the lab one. From the Doppler shift formula, we find

$$\epsilon' = \epsilon\gamma(1 - \beta\cos\theta) \tag{2.53}$$

$$\epsilon_1 = \epsilon_1'\gamma(1 + \beta\cos\theta_1'). \tag{2.54}$$

Using our previous result from Equation 2.47, it is also possible to write down

$$\epsilon_1' \approx \epsilon\left(1 - \frac{\epsilon}{mc^2}(1 - \cos\Theta)\right) \tag{2.55}$$

$$\cos\Theta = \cos\theta_1'\cos\theta' + \sin\theta'\sin\theta_1'\cos\phi' - \phi_1',$$

(where the phi' component is the azimuthal part of the system) and so,

$$\epsilon_1 \approx \epsilon\gamma^2(1 - \beta\cos\theta)(1 + \beta\cos\theta_1'). \tag{2.56}$$

This process converts a low-energy photon to a high-energy photon by a factor of the order γ^2. However, due to the conservation of energy, a photon with energy γmc^2 cannot be obtained after this process.

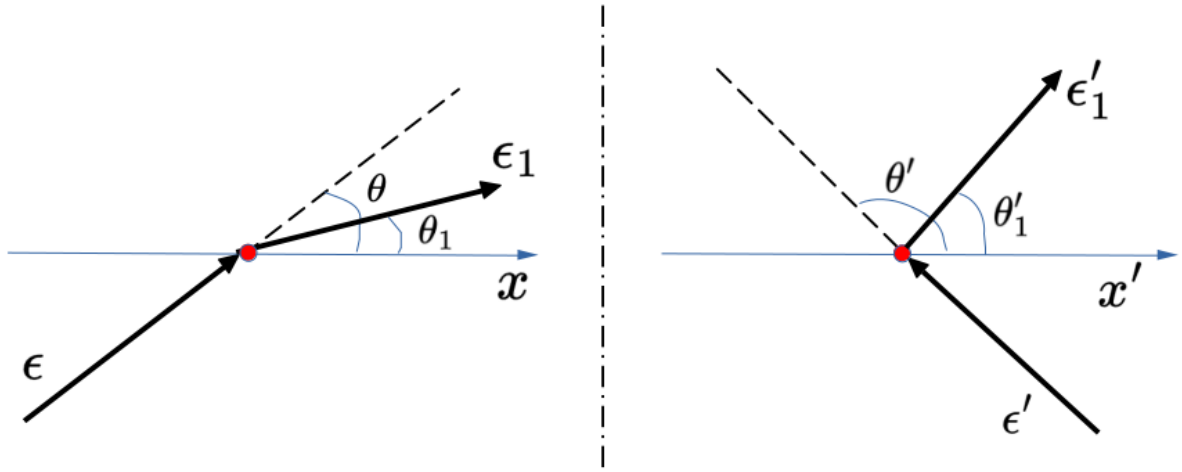

Figure 2.8. Geometries for inverse Compton scattering in the lab rest frame (non-primed system, left) and the electron's frame (primed system, right)

2.4.1 IC Power for Single Scattering

Now, we can derive the power for the case of an isotropic distribution of photons scattering an isotropic distribution of electrons. The previous formulas can be averaged, as done in Blumenthal and Gould (1970), to obtain the desired result. The total power scattered from the electrons in their rest frame is

$$\frac{dE_1'}{dt'} = c\sigma_T \int v'\epsilon_1' d\epsilon' \tag{2.57}$$

where $v'd\epsilon'$ is the density of photons in an energy range $d\epsilon'$. This number density is related to the photon phase space distribution function $n'(p')$ as

$$v'd\epsilon' = n'd^3p'. \tag{2.58}$$

As these quantities are Lorentz invariant, and using Equation 2.53, our previous equation becomes

$$\frac{dE_1}{dt} = c\sigma_T\gamma^2 \int (1-\beta\cos\theta)^2 v\epsilon d\epsilon. \tag{2.59}$$

With the fact that we are assuming an isotropic distribution, it is also possible to take the average over all angles; we obtain

$$\frac{dE_1}{dt} = c\sigma_T\gamma^2\Big(1+\frac{1}{3}\beta^2\Big)\int v\epsilon d\epsilon = c\sigma_T\gamma^2\Big(1+\frac{1}{3}\beta^2\Big)U_{\rm ph} \tag{2.60}$$

where $U_{\rm ph}$ represents the initial photon energy density

$$U_{\rm ph} \equiv \int v\epsilon d\epsilon. \tag{2.61}$$

By taking now the difference between the total power emitted and the rate of decrease of the total initial photon energy (recalling $\gamma^2 - 1 = \gamma^2\beta^2$) we finally have

$$P_{\rm IC} = \frac{dE_{\rm rad}}{dt} = \frac{4c\sigma_T}{3}\gamma^2\beta^2 U_{\rm ph} \tag{2.62}$$

This final result reveals the well-known ratio of IC to synchrotron energy losses (Equation 2.33):

$$\frac{P_{\rm IC}}{P_{\rm synch}} = \frac{U_{\rm ph}}{U_{\rm B}} \tag{2.63}$$

2.4.2 IC Spectrum for Single Scattering

The IC spectrum, from our last relation, must be expected to have the same behaviour as for the synchrotron case $s = (p-1)/2$. However, this spectrum is seen at higher energies.

In the simplest picture, using Equation 2.53, the maximum energy that a photon can achieve after IC is found by

$$\epsilon_1 \approx \epsilon' \gamma^2 (1+\beta) \approx \epsilon \gamma^2 (1+\beta)^2 \tag{2.64}$$

As in the relativistic case $\beta \to 1$, we find

$$\frac{\epsilon_1}{\epsilon} \approx 4\gamma^2 \tag{2.65}$$

meaning that the maximum energy an up-scattered photon can achieve is $4\gamma^2$ the original photon's energy. The average up-scattered energy $\langle \epsilon_1 \rangle$ can be found if we divide Equation 2.62 by the number of photons scattered per unit time per electron $\dot{N}_{\rm IC}$. The last rate can be written as

$$\dot{N}_{\rm IC} = \frac{c\sigma_T}{h\nu} U_{\rm ph}, \tag{2.66}$$

meaning that

$$\langle \epsilon_1 \rangle = \frac{4}{3}\gamma^2 \epsilon. \tag{2.67}$$

A more exhaustive treatment of the previous result, including the Compton effect and KN cross section, can be found in Jones (1968).

2.5 Synchrotron self-Compton Radiation

The synchrotron self-Compton (SSC) process is a mechanism in which high-energy electrons in a synchrotron radiation field scatter some of the synchrotron photons, boosting their energy to even higher levels. The scattered photons can then be emitted in the form of gamma rays. I.e., the nonthermal electrons that produce synchrotron radiation also interact with that radiation, resulting in a new emission of higher-energy photons. This process is important in understanding the emission properties of various astrophysical sources, such as blazars, as this process plays a crucial role in the modelling of the SED. It is possible to determine the radiated power due to SSC by calculating the emissivity e_ν (see § 2.1.2). The following explanation will be made using the same treatment as explained in Ghisellini (2013b).

2.5.1 SSC Contribution to the SED

Using the definition for e_ν, we can write it down

$$e_\nu d\nu = \frac{1}{4\pi} P_\nu N(\gamma) d\gamma \tag{2.68}$$

Using the result we found in Equation 2.67, it is possible to set

$$\left|\frac{d\gamma}{d\nu}\right| = \frac{\epsilon_1^{-1/2}}{2}\left(\frac{3}{4}\frac{1}{\epsilon}\right)^{1/2} \tag{2.69}$$

as the energy lost by an electron with energy γmc^2, within the interval $mc^2 d\gamma$, is converted into a radiation of frequency ν, within the range $d\nu$. Thus, substituting in Equation 2.68 our result from Equation 2.62, one finds a power-law distribution:

$$e_1(\nu_1) = \frac{1}{4\pi}\frac{(4/3)^\alpha}{2}\sigma_T c K \frac{U_{\rm ph}(\nu)}{\nu}\left(\frac{\nu_1}{\nu}\right)^{-\alpha} \tag{2.70}$$

and where the same link as in Equation 2.41 holds as a result of the fact that both the peak frequencies of the single electron spectra for IC and synchrotron radiation are typically a factor of γ^2 higher than the initial frequency. Now, if we multiply and divide by the radius of the source R, and use a proxy to estimate the optical depth of scattering of relativistic electrons such that $\tau \equiv KR\sigma_T$, we find

$$e_1(\nu_1) = \frac{1}{4\pi}\frac{(4/3)^\alpha}{2}\frac{\tau c}{\nu}\frac{U_{\rm ph}(\nu)}{R}\left(\frac{\nu_1}{\nu}\right)^{-\alpha} \tag{2.71}$$

Thus, when τc is less than 1, τc represents the proportion of seed photons ($U_{\rm ph}/h\nu$) that experience scattering during a time period of R/c. Additionally, the ratio of ν_1 to ν is approximately proportional to γ^2, which denotes the average in the increase in energy of the scattered photons.

A more appropriate expression for the photon energy density, one related to synchrotron radiation, must be used. This can be done by relating the specific synchrotron radiation energy density with the luminosity produced by the synchrotron and thus with the specific synchrotron emissivity. This reads:

$$U_{\rm syn}(\nu) = \frac{3}{4}\frac{R}{c}\frac{L_{\rm syn}(\nu)}{V} = 4\pi\frac{3R}{4c}j_{\rm syn}(\nu) \tag{2.72}$$

where the quantity of $3R/(4c)$ represents the typical time it takes for a photon to cross the source, while V denotes the volume of the source. If we now substitute our last equation into the result found in Equation 2.71, and using the trick of writing down the specific synchrotron emissivity calculated at the Compton frequency ($j_{\rm syn}(\nu) = j_{\rm syn,0}\nu^{-\alpha}$) we find

$$e_{\rm SSC}(\nu_1) = \left(\frac{4}{3}\right)^{\alpha-1}\frac{\tau}{2}j_{\rm syn,0}\nu_1^{-\alpha}\frac{1}{\nu} \tag{2.73}$$

Finally, considering the frequency range of the seed photons instead of them being monochromatic, we need to integrate our last result in terms of the incoming frequency. It is

clear that, regardless of the integration limits, this leaves us with a logarithmic function. This final result reads as follows:

$$j_{\rm SSC}(\nu_1) = \left(\frac{4}{3}\right)^{\alpha-1} \frac{\tau}{2} j_{\rm syn}(\nu) \ln \lambda \tag{2.74}$$

where λ will depend on the integration limits. It is straightforward that a ratio between the synchrotron and the SSC flux, which will be proportional to $\sim \tau \ln \lambda$. The result can be better understood using Figure 2.9.

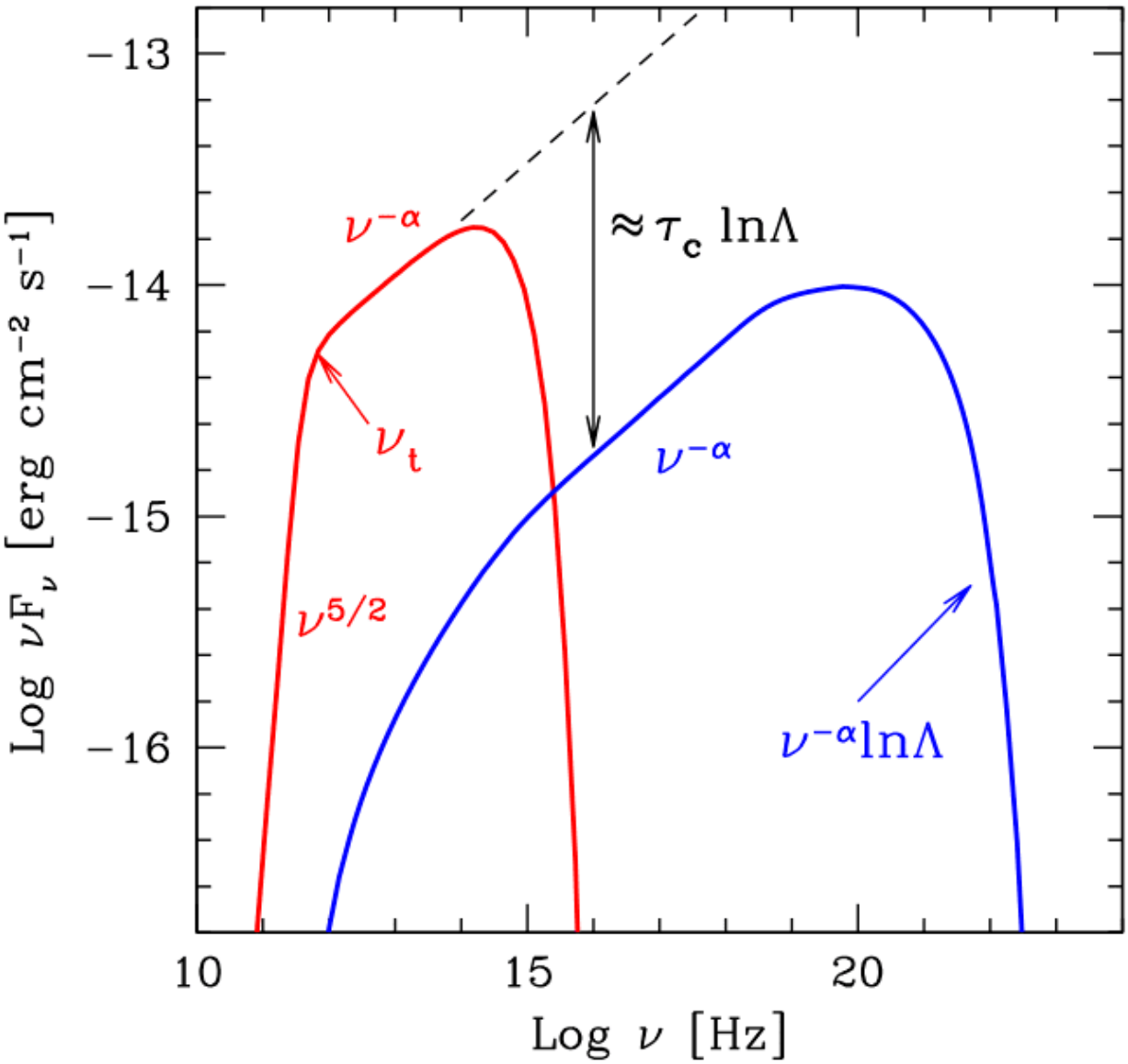

Figure 2.9. This is an illustration of an SSC spectrum which displays the synchrotron component in red and the SSC component in blue. The slopes of the spectrum at various photon energies are also shown, with an arrow indicating the ratio between the synchrotron and SSC spectra. Figure taken from Ghisellini (2013b).

2.6 External Comptonization

Proposed first by Dermer et al. (1992) and Sikora et al. (1994), the EC processes in a blazar involves the interaction of relativistic particles in the jet with photons from external sources, such as the accretion disc, DT, or the BLR. During this process, the relativistic particles scatter the external photons, causing them to be energised to much higher levels. The resulting boosted photons can escape from the system and are observed as high-energy radiation, with a significant contribution at $\gamma-$ray wavelengths in the SED.

As mentioned in Dermer and Menon (2009), there are two main approaches to analyse the scattered spectra in theoretical treatments. The first method involves transforming the external radiation field into the comoving frame, where the scattered spectrum is calculated, and then transforming it back into the observer frame (e.g., Dermer and Schlickeiser (1993)). The second method involves transforming the electron distribution into the stationary frame and then Compton scattering the external photon field (e.g., Georganopoulos et al. (2001)). Although both approaches lead to the same answer, we will focus on the latter. For the following, I will summarise and extract the most relevant results for this work from Georganopoulos et al. (2001), so for a more rigorous treatment, refer to the named paper.

2.6.1 EC Contribution to the SED

We will revisit the one-zone model previously discussed in § 1.2.2 in the current context. The model involves a plasma blob that moves at a relativistic speed with a bulk Lorentz factor of Γ and a velocity of βc. It is positioned at an angle θ to the observer's line of sight (refer to Figure 1.7). Since the relativistic outflow moves with a bulk Lorentz factor Γ and is observed at small angles $\theta \approx 1/\Gamma$ (see § 2.2.2), the emitted fluxes are affected by a beaming factor δ defined in Equation 2.22. Within the blob's frame-of-reference, the electrons have an isotropic power-law density distribution. We will assume that this electron distribution interacts with seed photons that have an arbitrary angular distribution. Since the electrons in the blob are ultrarelativistic, the resulting photons will travel in the same direction as their scattering electron. Thus, when observing from a specific angle, only the electrons that move in the same direction contribute to Compton luminosity. To calculate the external Compton luminosity, an angle-dependent multiplication term caused by varying seed-photon angular distributions must be factored in. It can be easily shown that this specific Compton luminosity, which is the luminosity observed per energy interval per solid angle, is proportional to δ^{3+p} due to the fact that the effective number of electrons is also proportional to δ^{3+p} (Dermer et al., 1992).

In this context, we introduce the assumption that the plasma blob travels through an environment containing an isotropic mono-energetic photon field with energy density $U_{\rm ph}$. A similar scenario was explored in § 2.4.1, where it was demonstrated that the observed scattered

energy is proportional to γ^2. It is now assumed that the outgoing photons are aligned with the scattering electrons, which is valid as long as the electron angular distribution changes gradually over the angular scales of $\lesssim 1/\gamma$. To calculate the specific luminosity, one must integrate the scattering rate (which can be obtained from Equation 2.62) over the electron energy distribution, then multiply the result by the observed photon energy $\epsilon_1 mc^2$ and the photon number density $n_p = U_{\rm ph}/\epsilon mc^2$. In the lower limit scenario, for Thomson scattering ($\gamma\epsilon \ll 1$), the luminosity yields,

$$\frac{dL}{d\epsilon_1 d\Omega} \approx \delta^{3+p} \frac{K}{\pi} \frac{2^{p-1} V_{\rm blob} c\sigma_T}{\epsilon(1+p)(3+p)} \left(\frac{\epsilon_1}{\epsilon}\right)^{-(p-1)/2} U_{\rm ph} \tag{2.75}$$

where K represents the normalisation constant for the electron distribution and $V_{\rm blob}$ the volume of the blob in the blob frame. Again, we recover our previous result for the spectrum in the Thomson limit to be a power-law with spectral index $\alpha = (p-1)/2$.

On the contrary, in the KN regime, the SED exhibits some differences. Numerical simulations demonstrate that the SED resulting from a power-law electron energy distribution is not a power-law and cannot be characterised by a unique spectral index. This is due to the fact that the limits of the integral of the electron energy distribution are different, since the maximum attainable energies scale as $\epsilon \propto \delta\gamma$. Furthermore, the peak energy is insensitive to changes in both δ and γ, and it is located at an energy $\epsilon_{1,\rm peak} \lesssim 1/\epsilon$ producing a cut-off energy higher than the maximum electron energy in the Thomson regime.

For a more comprehensive analysis and detailed computations of the EC emissivity with respect to different distributions of the external radiation field, please consult the existing literature (e.g., Dermer et al. (1992), Dermer and Menon (2009), Dermer and Schlickeiser (1993), and Georganopoulos et al. (2001)).

2.7 The Blazar's Jet

Having familiarised ourselves with the primary characteristics of an AGN, particularly a Blazar, and having explored the main radiative processes involved, we can now proceed to make initial estimations of the key parameters describing the emissions observed through the blazar's jet, as well as its power. As mentioned earlier, we will employ a consistent one-zone leptonic model. In particular, we are most curious to be able to determine the beaming factor δ, as well as the magnitude of the magnetic field B responsible for accelerating the electrons within the blob. Furthermore, we will assume knowledge of the luminosity peaks ($L_{\rm synch}$ for the peak associated with synchrotron emissions and $L_{\rm C}$ for the high-energy peak) as well as their respective peak frequencies ($\nu_{\rm synch}$ and $\nu_{\rm C}$). In this exercise, we will follow the same

approach as described in Ghisellini (2013b). For a more detailed discussion, we encourage interested readers to refer to the bibliography.

We will consider the case in which the high-energy peak is only the result of an SSC process. However, the same treatment can be used for EC processes as for FSQR, where the latter is dominant for the high-energy emissions.

2.7.1 High Emissions due SSC

We have already shown that the ratio between IC losses and synchrotron losses is constant (e.g., Equation 2.63. This same idea applies to SSC, which means:

$$\frac{L_{\rm C}}{L_{\rm synch}} = \frac{U'_{\rm ph}}{U'_B} \tag{2.76}$$

where the primed quantities refer to the comoving frame. If we now write $U_{\rm ph}$ in terms of $L_{\rm synch}$, passing from the observed frame to the comoving frame, one obtains

$$\frac{L_{\rm C}}{L_{\rm synch}} = \frac{L_{\rm synch}}{4\pi R^2 c\delta^4}\frac{1}{U'_B} \tag{2.77}$$

where R is the size of the emitting blob and δ the beaming factor (defined in Equation 2.22) as we should consider the relativistic beaming effect. Now, by using the magnetic energy density, $U'_B = B'^2/8\pi$, we get

$$\frac{L_{\rm C}}{L_{\rm synch}} = \frac{L_{\rm synch}}{4\pi R^2 c\delta^4}\frac{8\pi}{B'^2} \tag{2.78}$$

where B is the blob's magnetic field. Now, by substituting R, which is given by

$$R \sim ct_{\rm var}\frac{\delta}{1+z}, \tag{2.79}$$

where $t_{\rm var}$ is the minimum variability timescale, it is possible to obtain a first equation for the magnetic field, namely:

$$B'\delta^3 = (1+z)\frac{L_{\rm synch}}{ct_{\rm var}}\left(\frac{2}{cL_{\rm C}}\right)^{1/2}. \tag{2.80}$$

Now, lets consider our result from Equation 2.65. With it, we can write that the ratio between the frequencies peak of the SSC and the synchrotron is

$$\frac{\nu_{\rm C}}{\nu_{\rm synch}} = \gamma^2 \tag{2.81}$$

Now, by using our result from Equation 2.67 and Equation 2.25, we can have an expression

for the synchrotron frequency peak in terms of B', namely:

$$\nu_{\text{synch}} \sim \frac{4}{3}\nu'_B\gamma^2\frac{\delta}{1+z} = \frac{4}{3}\frac{eB'}{2\pi m_e}\gamma^2\frac{\delta}{1+z}. \tag{2.82}$$

By inserting this last expression into Equation 2.81 we obtain

$$B'\delta = \frac{3\pi m_e}{2e}\frac{\nu^2_{\text{synch}}}{\nu_{\text{C}}}(1+z) \tag{2.83}$$

meaning we have a set of two equations, 2.83 & 2.80, for two unknown parameters, B' and δ.

2.7.2 Power of the Jet

Blandford and Znajek (1977) explain that the total power of the jet is predicted to depend on the square of the product between the spin of the black hole, M_{BH}, and the magnetic field at its event horizon. Nevertheless, it is also possible to explain this power by dissecting it into its various constituents. Initially, there is radiation emission (represented as P_{rad}), which sets a lower limit on its power. The jet contains electrons responsible for generating the observed radiation, and they exhibit relativistic motion in the comoving frame (P_e). The presence of protons in the jet is a topic of debate; if radiation arises from electron-positron interactions, no protons are present. However, if the plasma contains both electrons and protons, there would be one proton per emitting electron (P_p). Additionally, the jet carries a magnetic field, contributing to its overall power through the Poynting flux (P_B). Generally, all these components can be expressed as follows:

$$P_i = \Gamma^2\pi R^2\beta c U'_i. \tag{2.84}$$

where U'_i represents the comoving energy density for the $i-$th component. Specifically, for the case of emitting electrons, the energy density is given by:

$$U'_e = m_e c^2 \int \gamma N(\gamma) d\gamma. \tag{2.85}$$

To describe the radiation, we use its relation with the total luminosity:

$$U'_{\text{rad}} = \frac{L}{4\pi R^2 c}\frac{1}{\delta^4} \tag{2.86}$$

as we transition to the comoving frame. When dealing with the magnetic field, the usual relation applies:

$$U'_B = \frac{B'^2}{8\pi}, \tag{2.87}$$

and finally, for the cold protons, we use:

$$U'_p = \frac{U_2}{\langle\gamma\rangle}\frac{m_p}{m_e}N_{p-e} \tag{2.88}$$

where N_{p-e} is the ratio of cold protons to relativistic electrons.

Observations indicate that the jet in powerful blazars is remarkably potent, sometimes comparable to or even surpassing the power of the accretion disc, with a clear correlation between them (e.g., Ghisellini et al. (2014)). Moreover, it is evident that the dominance of the jet cannot be solely attributed to the Poynting flux, as the inverse Compton component predominantly governs the bolometric luminosity.

2.8 Thermal Radiated Power due Accretion

Including thermal radiative processes in the description of the SED of a blazar is important to obtain a complete picture of the emission mechanisms and physical properties of the system. These processes can provide insights into the structure and dynamics of the central engine and help us better understand the mechanisms that drive the spectral characteristics of blazars. Although the thermal profile of the DT can be represented by a uniform blackbody with a temperature that can range from a few hundred to a few thousand Kelvin, the accretion disc surrounding the SMBH emits thermal radiation through the process of accretion, which requires a different treatment. The radiation emanating from the accretion disc can make a substantial contribution to the SED at low frequencies, particularly in the far-infrared wavelengths.

An accretion disc is a common phenomenon in astrophysics, where matter accretes and forms a rotating disc around a central object, such as a black hole or any other type of compact object. This disc is formed because of the conservation of angular momentum, where the accreting matter has sufficient angular momentum to orbit the central object instead of falling directly onto it. The properties of the accretion disc, including its temperature and radiated power, depend on the physical processes that govern the behaviour of the disc. Radiated power is one of the most important properties of the accretion disc. As the accreting matter falls onto the central object, it releases gravitational potential energy. Some of this energy is radiated away as light, whereas the rest increases the rotational kinetic energy of the disc. The temperature of the disc plays a crucial role in determining the radiated power, since the disc emits multicolour blackbody radiation. The radiated power depends directly on the accretion rate $\dot{M}$, which can be obtained from the continuity equation using the assumptions of the Bondi-Hoyle model: spherical symmetry, stationarity, plasma treated as a gas in an adiabatic system, non-self-gravitating system, and non-relativistic.

Understanding the radiated power in an accretion disc relies on the thin disc approximation, specifically the Shakura-Sunyaev treatment (e.g., Shakura and Sunyaev (1973)). This approximation assumes that the disc is thin and flat with all the radiated energy emanating from its surface. Although a simplified model, it has been shown to accurately describe the behaviour of accretion discs in many astrophysical systems. This section delves deeper into the radiated power in an accretion disc, focussing on the physical processes that govern its behaviour and the implications for astrophysical observations. By comprehending the properties of the accretion disc, we can gain valuable insights into the blazar's SED. The reader can refer to the literature to see a better treatment and the complete derivation of the relations named ahead (e.g., Frank et al. (2002) and Shakura and Sunyaev (1973)).

2.8.1 Accretion Disc

We will examine the dynamics of a thin disc, where we assume that the matter is confined to a plane very close to $z = 0$, in cylindrical polar coordinates (R, ϕ, z). Matter rotates in a circular motion with an angular velocity Ω around the accreting object, which has a mass M and a radius R_*. Typically, the angular velocity will have a Keplerian value

$$\Omega = \Omega_K(R) = \left(\frac{GM}{R^3}\right) \tag{2.89}$$

where G is the gravitational constant, R is the distance from the object's centre of mass, and M is the mass of the object in which matter is accreting. We can also write down the two components of the circular velocity

$$u_\phi = R\Omega_K(R) \tag{2.90}$$

$$u_r = -c_s^{\text{iso}} = -\sqrt{\frac{\partial P}{\partial \rho}} \sim -10\sqrt{\frac{T}{10^4 K}}\text{km/s} \tag{2.91}$$

for which c_s^{iso} is the plasma's isothermal speed of sound. It can be observed that the radial component of the velocity is negative, indicating that matter is indeed accreting onto the central object, while the velocity's ϕ component is significantly larger. This allows the system to be treated as a thin circular disc. With this information, it is now possible to estimate the disc's luminosity by determining the efficiency of the accretion process. The luminosity of the disc L_{acc} can be expressed as

$$L_{\text{acc}} = \eta \dot{M} c^2 \tag{2.92}$$

where c is the speed of light and efficiency η is defined as the difference of energy of a particle of mass m at infinity from the central object (E_∞) and the energy of the particle on the

surface or the innermost stable circular orbit $R_{\rm in}$ (which is often measured in units of the Schwarzschild radius R_S). If we set that the particle at infinity has no kinetic energy, then η is simply

$$\eta = \frac{E_\infty - E_{R_{\rm in}}}{E_\infty} = \frac{mc^2 - (mc^2 - GMm/R_{\rm in})}{mc^2}, \tag{2.93}$$

Thus, substituting in Equation 2.92, we finally get

$$L_{\rm acc} = \frac{GM\dot{M}}{R_{\rm in}}. \tag{2.94}$$

As the material in the disc moves towards the central object, it also moves relative to other material in the disc, causing a shear movement. This shearing motion creates turbulence in the disc, which leads to the generation of vortices and eddies. It is by the motion of the eddies that internal friction between the fluid molecules is generated, which results in the creation of kinematic viscosity ν in the disc. This ν plays an important role in the dynamics of an accretion disc, as it determines the rate at which material in the disc can transfer angular momentum and energy affecting the disc's temperature profile and has implications for the radiation emitted by the disc. The easiest way to understand this phenomenon is to do the following: suppose that we remove a ring from this disc, which can be characterised by its surface density Σ. This piece of the disc will exhibit macroscopic bulk motion with u_ϕ and with a flux o mass (the eddies) crossing back and forth, with a typical turbulent velocity called $\widetilde{u}$, and going from R to $R+\lambda$ (where λ is the typical lengthscale for the moving eddies), which will produce torque at the ring's border. The expression for Σ can be written as:

$$\Sigma = \int_{-H/2}^{H/2} \rho dz \approx \rho H \tag{2.95}$$

where H is the total height of the ring. As the border can be written as $S = 2\pi RH$. It is also possible to write the flux of mass going between the border of the ring as

$$\rho\widetilde{u}S = \rho\widetilde{u}2\pi RH.$$

Thus, the change in angular momentum over time, the torque, will be

$$\frac{\Delta L}{\Delta t} = 2\pi R\Sigma\widetilde{u}R(R\Omega(R) - (R+\lambda)\Omega(R+\lambda)) \tag{2.96}$$

which, by talking the limit where λ is infinitesimally small, transforms to

$$\frac{\Delta L}{\Delta t} \approx -2\pi R\Sigma\widetilde{u}\lambda R^2\frac{d\Omega}{dR}. \tag{2.97}$$

As ν has units of m^2/s, it is fine to say that ν can be written as

$$\nu \sim \widetilde{u}\lambda \tag{2.98}$$

which allows us to write the torque produced by the outer layer surface onto the inner layer of the ring as

$$\frac{\Delta L}{\Delta t} = G(R) = 2\pi R\Sigma\nu R^2\frac{d\Omega}{dR}, \tag{2.99}$$

telling us that for a rigid solid rotation, there is no torque and thus no transfer of matter. In any case, the torque, as already said, depends explicitly on the viscosity to which meaning must be given. However, turbulence is a complex and poorly understood phenomenon, and the physical mechanisms involved in determining the lengthscale and turnover velocity of turbulent eddies are not well understood. The largest turbulent eddies are limited by the thickness of the disc H, and the turnover velocity is likely to be subsonic to avoid thermalisation by shocks. Therefore, we can give a value to the kinematic viscosity:

$$\nu = \alpha c_s H \tag{2.100}$$

expecting $\alpha \lesssim 1$. This is known as the $\alpha-$prescription of Shakura and Sunyaev (1973).

Using what we have written down, it is now possible to find the radiated power per unit area of the disc. First, we must find the total torque produced on the disc, which will be

$$\tau = G(R+dR) - G(R) = \frac{dG}{dR}dR \tag{2.101}$$

This torque can be related to the dissipation of work by simply using the relation,

$$P = \frac{dW}{dt} = \tau\frac{d\phi}{dt} = \tau\Omega = \Omega\frac{dG}{dR}dR. \tag{2.102}$$

Taking the integral to have the total energy dissipation rate in the disc, we get the following:

$$\dot{E} = \int_{R_{\text{in}}}^{R}\Omega\frac{dG}{dR}dR = G\Omega\Big|_{R_{\text{in}}}^{R} - \int_{R_{\text{in}}}^{R}G\frac{d\Omega}{dR}dR \tag{2.103}$$

where the variation of $G\Omega$ represents the flow in the borders and the part $-$ is the true dissipation in the inner part of the ring. By defining the radiated power per unit area $D(R)$ as

$$D(R) = \frac{\dot{E}_{\text{in}}}{2\times 2\pi RdR} = \frac{G}{4\pi RdR}\frac{d\Omega}{dR}dR \tag{2.104}$$

where the denominator accounts for the two faces of the disc (see Figure 2.10), if we substitute

our result obtained in Equation 2.99 we get

$$D(R) = \frac{1}{2}\nu\Sigma R^2\Big(\frac{d\Omega}{dR}\Big)^2 \tag{2.105}$$

which again depends explicitly on the viscosity and on the fact that the accretion disc will only glow if it is rotating differently from the rigid solid rotation.

It is now possible to write down both mass and angular conservation. For this, we will use the already-named Shakura-Sunyaev disc (SSD).

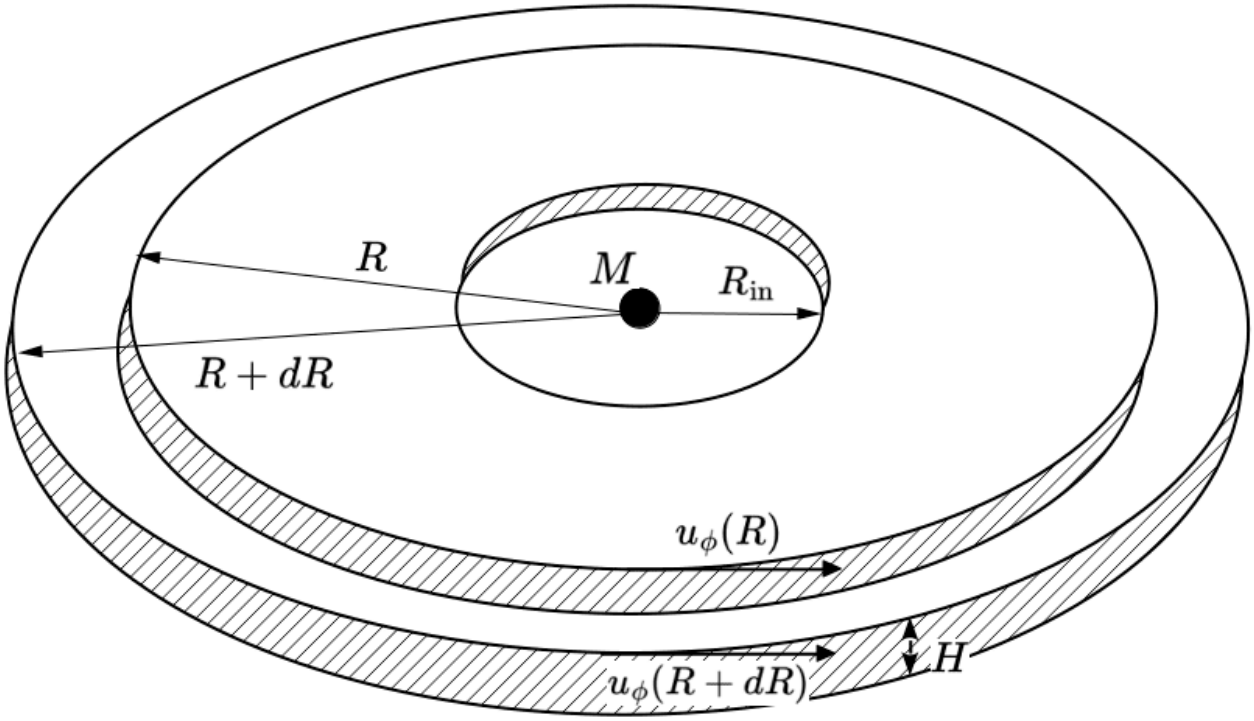

Figure 2.10. Slice of a thin Bondi-Hoyle accretion disc around an object of mass M where mass is accreting towards the object.

2.8.2 The Shakura–Sunyaev Model: Stationary Approach

To simplify the problem, we assume that α is constant, even though it is generally a function of factors such as pressure and temperature, we still expect that the properties of the disc are not explicitly dependent on α. To do this, we will make several assumptions. Firstly, the disc must be thin, which means that H in any radius is much smaller than R. Second, we will break down the velocity into its transversal and radial components and assume that the former is greater than the latter. Third, we assume that the system has azimuthal symmetry. We will be working with cylindrical coordinates, relying solely on R and z for dependence.

We will first start by writing down the conservation equations of the mass and angular momentum. For both, we need a differential mass element $\Delta m = 2\pi R\Delta R\Sigma$, so we have, for

mass conservation,

$$\begin{aligned}\frac{\partial \Delta m}{\partial t} = 0 &= u_r(R,t)2\pi R\Sigma(R,t) - u_r(R+\Delta R,t)2\pi(R+\Delta R)\Sigma(R+\Delta R,t) \\ &\approx -2\pi R\Delta R\frac{\partial(u_R R\Sigma)}{\partial R}\end{aligned} \tag{2.106}$$

meaning that the inside term of the partial with respect to R should be a constant, namely, the accretion rate:

$$\dot{M} = 2\pi u_r R\Sigma \tag{2.107}$$

For the angular momentum conservation equation, we will first write the angular momentum as

$$\Delta L = \Delta m R u_\phi = 2\pi R\Delta R\Sigma R^2\Omega. \tag{2.108}$$

Meaning that if we take the partial derivative with respect to the time we have, using the same treatment as in Equation 2.106,

$$\begin{aligned}\frac{\partial \Delta L}{\partial t} &= u_r(R,t)2\pi R\Sigma(R,t)R^2\Omega(R,t) \\ &\quad - u_r(R+\Delta R,t)2\pi(R+\Delta R)\Sigma(R+\Delta R,t)(R+\Delta R)^2\Omega(R+\Delta R,t) \\ &\quad + \frac{\partial G}{\partial R}\Delta R,\end{aligned} \tag{2.109}$$

which can be written more compactly as

$$\frac{\partial \Delta L}{\partial t} = -2\pi\Delta R\frac{\partial}{\partial R}\Big(u_r R\Sigma R^2\Omega\Big) + \frac{\partial G}{\partial R}\Delta R. \tag{2.110}$$

As done before, it is also possible to use a steady solution, meaning that the previous equation is equal to zero. This, and our previous result from Equation 2.107, yields

$$-\dot{M}R^2\Omega = G(R) + \text{constant} \tag{2.111}$$

where the constant comes from the integral and can be computed by setting initial conditions. For simplicity, we can evaluate our equation at $R = R_{\text{in}}$, where $G(R_{\text{in}}) = 0$. Thus, we have

$$-\dot{M}R^2\Omega = G(R) - -\dot{M}R_{\text{in}}^2\Omega(R_{\text{in}}) \tag{2.112}$$

and by substituting our result obtained in Equations 2.89 & 2.99 after some manipulation, we obtain the following result:

$$\Sigma\nu = \frac{\dot{M}}{3\pi}\left(1 - \sqrt{\frac{R_{\text{in}}}{R}}\right). \tag{2.113}$$

We now see that it is possible, using Equation 2.105, to relate the power emitted per unit area to the accretion rate. Thus, by using these two equations and evaluating the integral from R_{in} to a given R_{out} (where the former is much bigger than the latter), we get that the luminosity coming from the accretion disc is:

$$\boxed{L_{\text{disc}} = \frac{1}{2}\frac{GM\dot{M}}{R_{\text{in}}} = \frac{1}{2}L_{\text{acc}}.} \tag{2.114}$$

This is a powerful tool as now, knowing that the only mechanism process related to the emission of radiation from the accretion disc is only dependent on the temperature, it is possible to compute all the blackbody radiation fields giving us a multicolour blackbody.

As a final comment, there is a well-known quantity that serves as a limit on L_{disc}: the Eddington luminosity. Denoted as L_{Edd}, it corresponds to the maximum luminosity to balance the radiation pressure with gravity. For instance, a typical composition for the material in an accretion disc is made up of dissociated hydrogen: protons and electrons. As we have seen (Equation 2.48), the cross section of the electrons for Thomson scattering will be much larger than that of the protons, while the gravitational force will be much larger on the protons since they are more massive. Thus, by equating the radiative and gravitational force on the electron and proton, respectively, neglecting the two other forces, we find:

$$\frac{L\sigma_T}{4\pi R^2 c} = \frac{GMm_p}{R^2}, \tag{2.115}$$

and solving for L we find

$$L = L_{\text{Edd}} \equiv \frac{4\pi c GMm_p}{\sigma_T} = 1.26 \times 10^{38}\frac{M}{M_\odot}\ \text{erg s}^{-1}. \tag{2.116}$$

Meaning L_{Edd} exclusively depends on the M of the body responsible of the radiation emitted. For example, if the rate of accretion were to result in $L_{\text{disc}} > L_{\text{acc}}$, the accreting mass would experience radiation pressure that counters gravity. As a result, the process of accretion would cease, causing that at a certain point L_{disc} will decrease below L_{acc}. This demonstrates a self-regulating mechanism in action.

2.8.3 The Multicolour Blackbody

As said, the spectrum emitted by a thin disc will be dictated by a multicolour blackbody as the inner regions of the disc are hotter than the outer ones. Using then the relations discussed in § 2.1, it is easy to show that when the radiation is produced exclusively due to temperature,

the spectrum emitted is described by a Planck function:

$$I_\nu \equiv B_\nu(T_{\rm s}(R)) = \frac{2h}{c^2}\frac{\nu^3}{\exp\left(\frac{h\nu}{k_B T}\right)-1} \tag{2.117}$$

where $T_{\rm s}(R)$ refers to the temperature on the surface of the disc at a given distance. It is relevant to tell the reader that the temperature in the middle of the disc $T_{\rm c}$, at $z = 0$, is hotter than at the surface $z = H/2$, and that the disc is optically thick ($\tau >> 1$); that is, radiative transport can be treated using the diffusion approximation. The radiative flux, F_ν, then reads as follows:

$$F(z) = -\frac{16\sigma T^3}{\alpha_R}\frac{\partial T}{\partial z} = -\frac{4}{3}\frac{1}{\alpha_R}\frac{\partial}{\partial z}(\sigma T^4) \tag{2.118}$$

where α_R is the Rosseland mean absorption coefficient and σ the Stefan–Boltzmann constant with a value of 5.67×10^5 ergs cm^{-2} s^{-1} K^{-4}. If we assume that $\tau(z = H/2) = \tau_{\rm s} = 1$, and $\tau(z = 0) = \tau_{\rm c}$, we can use Equation2.118 to obtain the ratio:

$$\frac{F(z = H/2)}{F(z = 0)} = \left(\frac{T_{\rm s}}{T_{\rm c}}\right)^4 \tau_{in} \ll 1 \tag{2.119}$$

as $T_{\rm c} \gg T_{\rm s}$ and the ratio is to the fourth power, and using Equation 2.11 to set everything explicitly in terms of $\tau_{\rm c}$. Therefore, if we compute $D(R) \approx F(z = 0) - F(z = H/2) \approx F(z = 0)$, using Equations 2.105 & 2.113, we will have

$$\frac{4}{3}\frac{\sigma T_{\rm s}}{\tau_{\rm c}} = \frac{3GM\dot{M}}{8\pi R^3}\left(1 - \sqrt{\frac{R_{\rm in}}{R}}\right) \tag{2.120}$$

giving us a straight relation between the temperature and intrinsic properties of the system, means that the emitted spectrum will depend on these parameters. From this last equation it is also easy to see that T not only decreases for higher values of z, but also for higher values of R; i.e., the farther away the matter spirals from $R_{\rm in}$, the colder that ring of the disc will be.

Finally, it is possible to estimate the shape of the emitted spectrum for an observer at a distance D whose line of sight makes an angle i with the normal of the disc plane, assuming that the emission comes from the disc surface, by computing the angle of view of the disc plane.

$$F_\nu = \frac{4\pi h\cos i}{c^2 D^2}\int_{R_{\rm in}}^{R_{\rm out}} \frac{\nu^3 R}{\exp\left(\frac{h\nu}{k_B T_{\rm s}(R)}\right)-1} dR \propto \int_{R_{\rm in}}^{R_{\rm out}} \frac{\nu^3 R}{\exp\left(\frac{h\nu}{k_B T_{\rm s}(R)}\right)-1} dR. \tag{2.121}$$

In the emitted spectrum, we have three different regions:

$$F_\nu \propto \begin{cases} \nu^2, & \text{if } h\nu \ll k_B T_{\text{out}}. \\ \nu^3 \exp\left(\dfrac{-h\nu}{k_B T_{\text{in}}}\right), & \text{if } h\nu \gg k_B T_{\text{in}}. \\ \nu^{\frac{1}{3}}, & \text{if } k_B T_{\text{out}} \leq h\nu \leq k_B T_{\text{in}}. \end{cases} \tag{2.122}$$

where T_{in} and T_{out} represent the temperatures at the innermost and outermost rings respectively. In particular, it is also shown in the spectrum a dependence of 1/3 which is characteristic of accretion discs. An example of this spectrum behaviour can be seen in Figure 2.11.

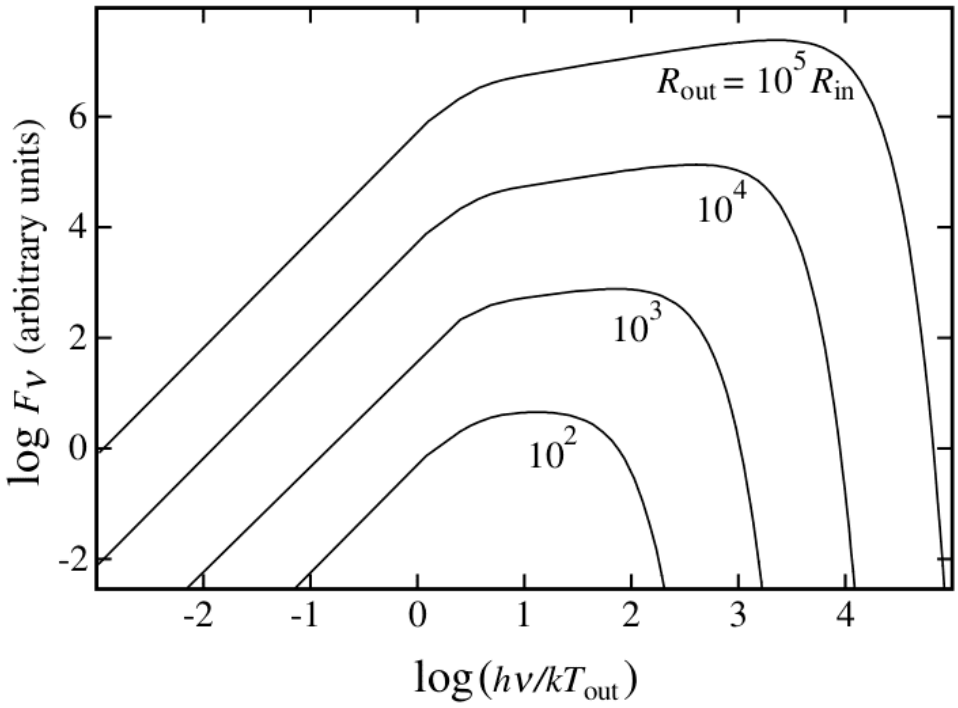

Figure 2.11. The spectrum F_ν of a constant, optically dense accretion disc that emits locally as a blackbody varies depending on the ratio of the disc's outer radius (R_{out}) to its inner radius (R_{in}). The frequency is normalised to $k_B T_{\text{out}}/h$, where T_{out} equals the temperature at R_{out}, the same way T_{in} at R_{in}. These spectra provide a visual representation of the proportionate size of the $\nu^{1/3}$ continuum in discs with different temperature ranges. It should be clear from the plot that the behaviour of $\nu^{1/3}$ can only be seen when R_{out} is very large. Plot taken from Frank et al. (2002).

As a last comment on the topic, we must expect that the peak of our spectra is determined by T_{in} which is the maximum temperature of the disc. Following the example presented in

Ghisellini (2013b): for an accretion disc with $T_{\rm max} = T_{\rm s}(R = R_{\rm in} = 10R_S)$, we find that:

$$\nu_{\rm peak} \sim \frac{kT_{\rm max}}{h} \sim 8.8 \times 10^{14} \left(\frac{L_{46}}{M_9^2}\right)^{1/4} \ {\rm Hz}$$

where M_9 is the black hole mass in units of $10^9 M_\odot$, and L_{46} the $L_{\rm disc}$ in units 10^{46} erg s^{-1}.

Chapter 3

Data Analysis and Modelling

In this study, we focus on analysing and modelling the spectral energy distribution of the blazar NVSS J163547+362930. Our objective is to obtain a comprehensive understanding of the source properties and investigate the underlying physical mechanisms that govern its behaviour. To achieve this, we employed a combination of data gathered from multiple missions and used the `JetSeT` *tool, which implements a homogeneous one-zone leptonic model.*

3.1 Data acquisition

Having delved into the characteristics of blazars, particularly focussing on our specific source, and having examined the primary radiative mechanisms that enable the investigation of the central engine's evolution and its interaction with its surroundings, our next step involves the creation and modelling of the source's SED. The initial phase of this chapter involves utilising publicly available information from various observatory catalogues to create a comprehensive raw SED, covering from radio to $\gamma-$rays. Subsequently, we will employ the established one-zone leptonic model within the `JetSeT` framework to develop a preliminary model that aligns with our data more accurately, especially when considering a standard SSD with an accretion efficiency of 0.083. Finally, following from the discussion of the different possible types of black hole that can be formed at high-redshift, we will propose different values for the accretion efficiency to constrain and relate the main parameters at play for all the models.

3.1.1 Low-Energy Observations

NRAO Green Bank Telescope & Very Large Array

Starting from the radio frequency range of the spectra, it was possible to use the information available from different surveys using the Green Bank (GB) Telescope of the

National Radio Astronomy Observatory (NRAO; e.g. Becker et al. (1991), Gregory and Condon (1991), Griffith et al. (1990), and White and Becker (1992)), different surveys from the NRAO Very Large Array (VLA; e.g., Becker et al. (1995) and Condon et al. (1998)), as well as the NRAO Very Long Baseline Array (VLBA) imaging and polarimetry Survey (e.g., Helmboldt et al. (2007)) to locate the emissions as well as the UL between the Radio-IR range of the SED.

Wide-field Infrared Survey Explorer

The Wide-field Infrared Survey Explorer (*WISE*; Wright et al. (2010)) is part of NASA's Explorers Programme [1] which was put into orbit back in 2009, and is one of the most suitable instruments to gather data in the IR band. Two years later after its launching, by 2011, it had surveyed the sky twice with its 40 cm telescope in four infrared wavelengths $w1$,$w2$, $w3$, and $w4$ at 3.4, 4.7, 12, and 23 μm, respectively. Upon completion of its surveys, the spacecraft has been put in hibernation mode, only to be reactivated in 2013 to become the Near-Earth Objects Wide-field Infrared Survey Explorer (*NEOWISE*). NVSS J163547+362930 is detected by the telescope onboard the *WISE* mission at a significance above 5 σ in the AB system in the two bands w 1 = 18.91 ($\pm$ 0.05) mag and $w2$=19.42 ($\pm$ 0.13) mag, while for the two bands $w3$ and $w4$, only upper limits 3 σ are derived. Conversions from instrumental source magnitudes to calibrated magnitudes were performed using the *WISE* photometric systems (Jarrett et al., 2011; Wright et al., 2010).

Early studies of *WISE* data have shown the connection between IR waveband and gamma-ray emission from blazars (Plotkin et al., 2012). Such an IR – gamma-ray correlation has been explored in a sophisticated study by F. Massaro and D'Abrusco (2016) where the authors explain a physical connection in favour of the correlation between the *Fermi*–LAT detected blazars and the *WISE* counterparts.

Gaia

The *Gaia* mission (Prusti et al., 2016) was launched in 2013 aiming to perform the most precise mapping of the Milky Way. While *Gaia* is optimised for selecting and measuring parallaxes and proper motion of point-like sources, it also provides accurate multi-band photometry. In a precise astrometry study by Plavin et al. (2019) related to the disk-jet environment in AGNs, the authors show that the coordinates and fluxes of the *Gaia* counterparts of high-redshift blazars are driven by the contribution of the accretion disk over the synchrotron component from the jet. Therefore, also the photometry is dominated by the accretion disk confirming several multifrequency campaigns of high-redshift blazars

[1] https://explorers.gsfc.nasa.gov

(Bottacini, E. et al., 2010).

The *GAIA* counterpart of the *Fermi*–LAT source (4FGL J1635.6+3628) has been searched in the publicly available third data release (DR3) (Vallenari et al., 2023) of the *G*aia mission. *GAIA*'s counterpart of the *F*ermi–LAT blazar is DR3 1327964378519702912. The *Gaia* G magnitudes are $G = 20.7951 \pm 0.0248$ mag, $G_{\rm BP} = 20.8728 \pm 0.3497$ mag, and $G_{\rm RP} = 19.6487 \pm 0.2105$ mag that are in agreement with the association and values of a cosmological evolution study of *Fermi*–LAT blazars by Zeng et al. (2021) for which the authors used the *Gaia* DR2 (Brown et al., 2018).

Swift UV–Optical Telescope

The high-redshift blazar was target by the UV–Optical Telescope (UVOT; e.g., Roming et al. (2005)) on board the *Swift* satellite with its filter of the day, which was the V filter. The data are analysed with `HEASoft` version 6.30 using CALDB version 20211108. This version allows for checking for the detector small-scale sensitivity, which can be corrected for count rates of up to 35%. We used the standard $5\prime$ aperture of the standard pipeline to reduce image products and correct exposure within the XIMAGE environment. The resulting magnitude is V=14.92 ($\pm$ 0.03). The conversion of magnitudes to fluxes is carried out using the constants of the photometric system in Poole et al. (2008).

SED of low energy observations

As a final comment on the data processing for the low-energy observations, we took into account for the attenuation due to the Galactic extinction. The extinction is computed with Cardelli's law (Cardelli et al., 1989) with a reddening coefficient of R_V=3.1 and an extinction coefficient in the V band of A_V=0.055 (Schlegel et al., 1998).

3.1.2 High-Energy Observations

XMM-Newton

The X-ray mission *XMM*-Newton (Jansen et al., 2001) has observed the source starting in 2017-07-23 10:27:12 (OBS-ID: 0802000101) for a rather low exposure (for such a distant source) of 23 ksec. Data were analysed using the Science Analysis Software 15.0.0 package following the standard procedure. The spectrum was extracted from a source region of $40''$ radius centred at the source of interest. The background was extracted from an area of same radius from the same chip, yet without contamination from the source. The tool for extracting the source and background spectra is `evselect`. The tools `rmfgen` and `arfgen` were used to generate response files and ancillary files.

Fermi Large Area Telescope

The *Fermi* mission, launched in 2009, observes the sky at GeV energies. Due to its observing strategy and its large field of view, the Large Area Telescope (LAT; e.g., Atwood et al. (2009)) scans the entire sky every two orbits (∼3 hours). This makes the mission very suitable for survey studies. Indeed, for the γ-ray range energy of the SED we utilised the information available in the fourth *Fermi* LAT 12-Year Point Source Catalogue (4FGL-DR3, for Data Release 3), based on 12 years of survey data in the 50 MeV-1 TeV energy range, including 5064 sources above 4σ significance (Abdollahi et al., 2022). The blazar NVSS J163547+362930, with its 4FGL designation 4FGL J1635.6+3628, is detected and identified in the LAT survey, from which the spectrum is taken.

Using the missions and observatories mentioned above, an extensive compilation of data was aggregated that spanned the entire SED range. The resulting data set is presented in Table 3.1, where it outlines the energy density values along with their associated errors at specific frequencies. Additionally, each data point is accompanied by the corresponding attributing mission or observatory, and it is indicated whether the point was employed as an upper limit (UL) or not.

3.2 JetSeT

`JetSeT` (Tramacere et al., 2009; Tramacere, 2020; Tramacere et al., 2011) is a versatile C/Python framework designed for simulating and reproducing radiative and accelerative processes in relativistic jets and galactic objects. The framework excels in handling observed data, defining data sets, and establishing connections with `astropy` tables and quantities. Moreover, it allows for the definition of complex numerical radiative scenarios, including SSC process, EC interactions, and EC interactions with the CMB. To enhance the accuracy of the modelling process, `JetSeT` incorporates a pre-fitting stage that constrains the model based on well-established phenomenological trends. By utilising parameters derived from observations, such as spectral indices, peak fluxes and frequencies, and spectral curvatures, the pre-fitting algorithm generates an informed starting model that aligns with these implemented trends. This ensures that the subsequent fitting process begins with a reliable initial configuration of the model. The framework supports both frequentist approaches, utilising the `minuit` package (James & Roos, 1975), and Bayesian Markov Chain Monte Carlo (MCMC) sampling, implemented through the `emcee` (Foreman-Mackey et al., 2013) package, facilitating the fitting of multiwavelength SEDs.

`JetSeT` provides a homogeneous one-zone framework, enabling the simulation of emission processes and physical conditions within the source. By considering the source's most relevant parameters (the magnetic field strength, particle densities, and accretion rates, etc.),

Source Data	Frequency (Hz)	νF_ν (erg cm^{-2} s^{-1})	$d\nu F_\nu$ (erg cm^{-2} s^{-1})	UL
4FGL-DR3 (100-1000 GeV)	7.65E+25	7.90E-13	0.00	True
4FGL-DR3 (30-100 GeV)	1.32E+25	5.28E-13	0.00	True
4FGL-DR3 (10-30 GeV)	4.19E+24	1.38E-13	0.00	True
4FGL-DR3 (3-10 GeV)	1.32E+24	3.29E-13	8.90E-14	False
4FGL-DR3 (1-3 GeV)	4.19E+23	4.99E-13	8.50E-14	False
4FGL-DR3 (0.3-1 GeV)	1.32E+23	9.54E-13	1.50E-13	False
4FGL-DR3 (0.1-0.3 GeV)	4.19E+22	2.28E-12	7.20E-13	False
4FGL-DR3 (0.05-0.1 GeV)	1.71E+22	1.38E-11	0.00	True
4XMM-DR12 (4.5-12 keV)	1.46E+18	6.80E-14	1.59E-14	False
4XMM-DR12 (2-4.5 keV)	7.87E+17	5.05E-14	9.45E-15	False
4XMM-DR12 (2-4.5 keV)	7.28E+17	5.13E-14	9.35E-15	False
4XMM-DR12 (1-2 keV)	4.75E+17	5.51E-14	9.91E-15	False
4XMM-DR12 (1-2 keV)	4.73E+17	5.40E-14	9.82E-15	False
4XMM-DR12 (1-2 keV)	3.72E+17	4.49E-14	8.71E-15	False
4XMM-DR12 (1-2 keV)	3.68E+17	5.06E-14	9.58E-15	False
4XMM-DR12 (0.5-1 keV)	2.99E+17	5.00E-14	8.35E-15	False
4XMM-DR12 (1-2 keV)	2.97E+17	3.85E-14	6.44E-15	False
4XMM-DR12 (0.5-1 keV)	2.36E+17	4.30E-14	7.18E-15	False
4XMM-DR12 (0.5-1 keV)	2.34E+17	4.77E-14	7.87E-15	False
4XMM-DR12 (0.5-1 keV)	1.67E+17	2.84E-14	4.95E-15	False
4XMM-DR12 (0.5-1 keV)	1.63E+17	3.07E-14	5.24E-15	False
Swift-UVOT	8.36E+14	4.20E-15	9.83E-15	False
GAIA	6.17E+14	4.11E-14	2.40E-15	False
GAIA	4.77E+14	7.21E-14	2.65E-15	False
GAIA	3.89E+14	7.72E-14	2.99E-15	False
GAIA	3.25E+14	5.08E-14	9.93E-15	False
WISE ($W1$)	8.53E+13	8.43E-14	4.09E-15	False
WISE ($W2$)	6.30E+13	3.89E-14	4.48E-15	False
WISE ($W3$)	2.42E+13	7.22E-14	0.00	True
WISE ($W4$)	1.32E+13	2.94E-13	0.00	True
NRAO VLBA (5 GHz)	5.00E+09	3.04E-15	0.00	True
NRAO GB	4.85E+09	4.32E-15	5.82E-16	False
NRAO GB	4.85E+09	4.17E-15	6.26E-16	False
NRAO GB	4.83E+09	2.66E-15	0.00	True
NRAO VLA	1.40E+09	2.13E-15	6.44E-17	False
NRAO GB	1.40E+09	1.72E-15	0.00	True
NRAO VLA	1.40E+09	1.59E-15	0.00	True
NRAO VLA	1.40E+09	1.55E-15	7.75E-17	False

Table 3.1. Summary of SED Data Points.

it is possible to investigate the emission mechanisms and gain insights into the fundamental processes at play. Building upon the acquired data and leveraging the capabilities of `JetSeT`, the next step involves constructing and refining the SED model for the blazar NVSS J163547+362930. This process entails adjusting the model parameters to achieve the best possible fit between the simulated SED and the observed data points. Through iterative refinement, the goal is to unveil the physical properties of the source, including the dominant emission mechanisms, energetics, and any unique characteristics that differentiate it from other astrophysical objects. The results obtained from the SED modelling provide valuable insights into the nature and behaviour of the source, facilitating a deeper understanding of its underlying astrophysical processes.

3.3 Model Constraining

3.3.1 Regrouping and Systematics

To enhance the accuracy of our model's fit to the data and effectively handle uncertainties, we will employ two complementary strategies: binning and the incorporation of systematic error into our dataset. Binning entails grouping similar data points into discrete bins, which minimises the impact of minor fluctuations and provides a clearer representation of the underlying data patterns while considering the overlapping of different instruments. By employing this approach, we can capture significant trends and relationships that may not be readily apparent when examining the raw data alone.

In addition, we will introduce systematic errors in our data set to account for various sources of inherent biases or inaccuracies. These sources can include limitations in instrumentation, calibration issues, and systematic biases in data collection methods. By adding systematics in our case, we address the concern that the minimiser may exhibit a bias towards better fitting the data in the IR-UV range as, typically, data points in this range have smaller errors compared to those at higher energies. Therefore, incorporating systematic errors helps to improve the overall reliability of our model by accounting for these potential biases. Additionally, considering these uncertainties allows for accounting for the intrinsic short-term variability of such sources, as the observations with the 6 previously mentioned facilities were not taken simultaneously. As already said, long-term variability has been ruled out by monitoring the source by the Fermi-LAT survey having a low variability index value.

The results of the implementation of these techniques can be seen in Figure 3.1. In general, the data were regrouped into 113 new bins, while a systematic error of 15% was added to all data points in the frequency range $10^6 \leq \nu \leq 10^{29}$ Hz. By implementing these techniques, we

not only enhance the quality and usefulness of our analysis, but we also optimise the runtime of the program to ensure the best fit of the data. This comprehensive approach allows us to handle uncertainties, accurately capture data patterns, and produce reliable results for our modelling efforts.

However, it is worth noting that coarse rebinning unavoidably results in the smoothing out of spectral characteristics. However, when modelling the broad-band SED from radio to γ-ray energies, the presence or relevance of narrow spectral features is neither of interest nor of use. As a final comment related to the data employed in this work, it is interesting to note that the *Swift* data point shows a relatively large error bar and is almost an order of magnitude smaller than the data within the IR-Optical region. This observation is noteworthy because this particular data point appears to be in close proximity to the Lyman-limit line, suggesting the potential for an independent approach to estimate the object's distance (e.g., Rau et al. (2012)). At the very least, it should enable us to establish a lower limit for the source redshift.

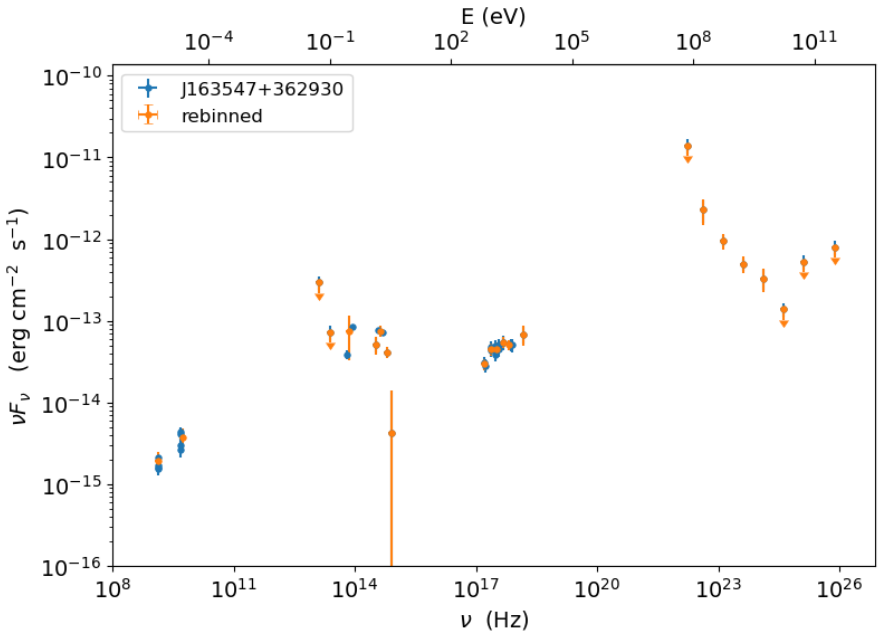

Figure 3.1. Comparison of the SED before and after employing data enhancement techniques. The original data are depicted in blue, whereas the new data resulting from the application of binning and the incorporation of systematic error are shown in orange. For the cases in which a data point is distant from another (such as the data point with the large vertical error bars between $\sim 10^{15}$ and 10^{17} Hz, as well as all *Fermi* points), the orange points overlap the blue ones rendering the latter not visible, despite its presence.

3.3.2 Constraining from Observables

As previously mentioned, `JetSeT` can be utilised to constrain our model from observable points. Thus, it is possible to obtain a phenomenological prefit model using minuit, resulting

in a set of initial conditions. For this purpose, and for all following models, a broken power-law for the electron distribution was used. The prefit SED model obtained in this step can be seen in Figure 3.2, as well as its values in Table 3.2. This gives us a good idea of the values that would be needed to be changed to better suit the observables, but also it gives us a first insight into the parameters related to the electron energy distribution, which will dictate the overall slopes of the SED.

Figure 3.2 reveals certain parameters in the initial prefit that fail to fully explain the SED. Specifically, the synchrotron component beyond the breaking energy inadequately matches the emissions in the IR-UV range. This discrepancy suggests that the synchrotron component within this range should have a lower intensity. Consequently, we anticipate a reduced slope after the break energy and a smaller minimum or breaking Lorentz factor for the electron energy distribution. Additionally, this indicates that the thermal emissions remain "naked", uncovered, by the synchrotron flux. These initial observations align with findings in the literature (e.g., Ghisellini (2013a), Ghisellini et al. (2009), Sahakyan et al. (2020), Tavecchio et al. (2000), and Zhang et al. (2014)). Exposure to thermal emissions, in particular to the emission of the disc, allows for a precise calculation of the total luminosity generated by the accretion disc $L_{\rm disc}$. Consequently, this model allows for more accurate constraints on the parameters associated with both the accretion disc and the total mass of the SMBH.

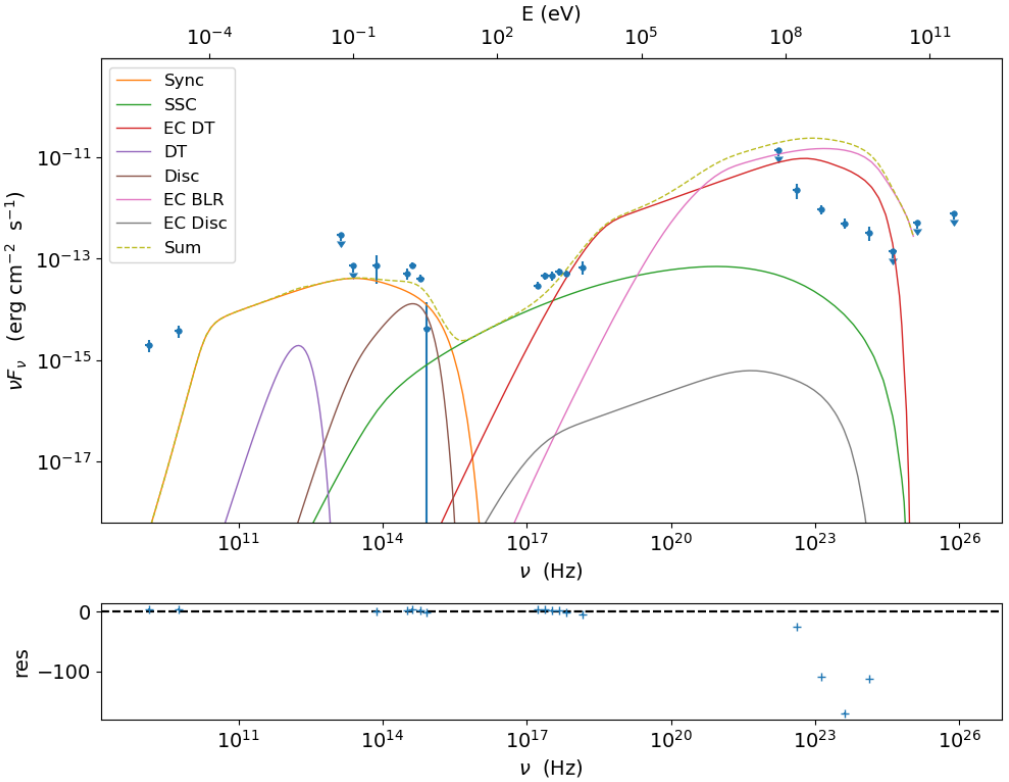

Figure 3.2. Prefit model for the SED of NVSS J163547+362930 from which a pair of initial physical observations providing crucial insights into the observed emissions were obtained.

Parameter	Value	Units	Model component
R	7.45	10^{16} cm	Blob
$R_{\rm diss}$	1.50	10^{18} cm	Blob
B	5.00	10^{-2} G	Blob
θ	3.00	deg	Jet viewing angle
Γ	1.85	10^{1}	Jet bulk factor
δ	1.91	10^{1}	Beaming factor
$\gamma_{\rm min}$	3.63	10^{1}	LE cut-off
$\gamma_{\rm break}$	5.38	10^{3}	Turn over energy
$\gamma_{\rm max}$	3.32	10^{4}	HE cut-off
N	4.20	10^{2} cm^{-3}	Emitters density
p	2.32		LE spectral slope
p_1	3.50		HE spectral slope
$R_{\rm in}$	3.00	$R_{\rm S}$	Disc
$R_{\rm out}$	5.00	$10^{2}R_{\rm S}$	Disc
M_{BH}	1.00	$10^{9}M_{\odot}$	Disc
η	8.00	10^{-2}	Disc
$L_{\rm disc}$	3.33	10^{45} erg s^{-1}	Disc
$R_{\rm DT}$	5.00	10^{18} cm	DT
$T_{\rm DT}$	1.00	10^{2} K	DT
$\tau_{\rm DT}$	0.10		DT
$R_{\rm BLR_{in}}$	1.00	10^{18} cm	BLR
$R_{\rm BLR_{out}}$	2.00	10^{18} cm	BLR
$\tau_{\rm BLR}$	0.10		BLR

Table 3.2. Prefit model values, Figure 3.2, as explained in § 1 and Figure 1.7.

Another inference that can be drawn from the prefit obtained by `JetSeT` is that the second peak in the SED is predominantly governed by EC scenarios. However, it remains unclear which specific component dominates the contributions in this energy range, particularly at the highest energies. However, as discussed in § 2.6.1, these emissions are explicitly dependent on both the distribution of electron energies and the energy density of the seed photons. Consequently, the optimal approach to fitting these emissions involves initially developing a more accurate model to explain the emissions up to the X-ray range. Of particular interest is a comprehensive characterisation of the central engine component, including the SMBH and the accretion disc, as these elements will have significant implications for both BLR and DT.

With this in mind, our strategy for modelling the SED is as follows: first, since the emissions from the accretion disc are believed to be entirely revealed, we will fit a multicolour blackbody to the data points corresponding to this energy band to obtain a coherent initial value of the total $L_{\rm disc}$. Second, with a better understanding of $L_{\rm disc}$, we can establish a range of values for both the size of the SMBH and the circumnuclear disc by modelling the SED using a set of accretion efficiency (η) values. Throughout this process, we will use a range of values for the synchrotron emission, and consequently, the SSC emission, to best match the X-ray contributions, which we believed are primarily attributed to the SSC component. Once these initial two steps are completed, taking into account the insights gained, we will fine-tune the

model to account for the high-energy contributions observed by the *Fermi*-LAT.

3.4 Modelling the Central Engine

As mentioned previously, SMBHs are located at the centre of the AGN and therefore also on powerful blazars. It is crucial to determine the black hole properties, such as the accretion rate $\dot{M}$, the already named accretion efficiency η, as well as the luminous accretion disc L_{disc} for SED modelling. One way to achieve this is by modelling the blazar accretion disc as proposed by Shakura and Sunyaev (1973) and explained exhaustively in § 2.8. The modelling will not only provide the previously named parameters, but also give us an estimate on the SMBH mass M_{BH}.

Blazars observed at high redshift provide insights into earlier stages of their evolution, indicating a more youthful phase for both the black hole and the host galaxy. Previous studies have proposed four main mechanisms for the formation of SMBHs: direct collapse scenarios (e.g., Begelman et al. (2006) and M. Latif and Schleicher (2015)), the collapse of massive Population III stars (e.g., Alvarez et al. (2009)), gas collapse and star formation (e.g., Devecchi and Volonteri (2009)), or intense gas accretion in a super-Eddington phase (e.g., Alexander and Natarajan (2014) and Madau et al. (2014)); a more exhaustive discussion of the topic can be found in Boekholt et al. (2018), Johnson et al. (2013), M. A. Latif and Ferrara (2016), and Petri et al. (2012). However, with the growing interest in gravitational waves and upcoming missions like the Large Interferometer Space Antenna (*LISA*), another formation possibility must be considered: mergers and/or gas accretion from smaller "seed" black holes (Berti, 2006; Tanaka & Haiman, 2009). In the context of *LISA*'s future operation in 2030, it becomes relevant to explore the dynamics of these primordial black holes, as their non-vanishing derivative of the mass quadrupole moment could generate mHz gravitational waves detectable by *LISA*. This would provide valuable insights into the formation theory. In any case, if any of these hypotheses holds for our specific object under consideration and the conditions are met, we anticipate that the SMBH will possess spin a and consequently exhibit higher values for η compared to a typical SSD model.

Furthermore, research indicates that rotating black holes not only demonstrate increased efficiency, but also have the potential to generate more luminous accretion discs, as the latter is proportional to η. Therefore, an expected $L_{\text{disc}} \geq 10^{46}$ erg s^{-1} is anticipated, which means that, as explained in Volonteri (2012), the "golden era" of SMBH with $M_{BH} \geq 10^9 \odot M$ occurred early in the universe. This expectation is supported by various observational studies, including Ackermann et al. (2017), Ghisellini et al. (2015), Paliya et al. (2016), and Sahakyan et al. (2020), among others.

Since the discovery of our blazar of study, estimations of its M_{BH} have been made by

studying its emissions in the IR-UV range (Ackermann et al., 2017; Li et al., 2018; Sahakyan et al., 2020), with a value of $\log M_{BH}/M_{\odot} = 8.7$. However, this is not the only method for calculating the mass. A comprehensive modelling of the entire spectrum, encompassing more than just the IR-UV range, could be employed. This is because the central engine not only affects the blazar's thermal emissions but also influences the non-thermal emissions generated through EC effects (e.g., as described in § 2.6.1, Błażejowski et al. (2000), Dermer et al. (2009), Liu and Zhang (2011), and Sikora et al. (1994)). Furthermore, when comparing the SMBH mass of the target source with similar sources and other SMBH values at that specific redshift, we anticipate that it will exhibit a larger size ($\log M_{BH}/M_{\odot} \gtrsim 9$). Therefore, SED modelling could also provide valuable insights into the size of the SMBH, and thus in its nuclear environment.

3.4.1 The Disc Luminosity

To determine $L_{\rm disc}$, a series of calculations were performed. Initially, the optical-UV data points within the SED originating from the accretion disc were fitted using a SSD multicolor blackbody model. The primary objective of this fitting process was to identify the optimal fit that accurately represents the observed data points, as shown in Figure 3.3. Once a satisfactory fit was achieved, the subsequent step involved obtaining the bolometric flux of the disc, denoted as $F_{\rm bol}$. This flux represents the total flux emitted over all wavelengths or frequencies by the accretion disc. In essence, $F_{\rm bol}$ was determined by integrating the flux per unit frequency across all frequencies using the following integral:

$$F_{\rm bol} = \int_0^{\infty} F_{\nu} d\nu. \tag{3.1}$$

For this particular case, a Monte Carlo integration method was employed to perform the integral. The procedure for this integration can be summarised as follows: initially, $N = 10^8$ random points were generated uniformly within a rectangle of area A, ensuring that the points spanned the minimum and maximum values along the x and y axes of the monochromatic flux. Subsequently, the number of points falling below the curve (denoted k) representing the multicolor blackbody were determined. Finally, the integral was approximated as follows:

$$F_{\rm bol} \approx \frac{k}{N} A. \tag{3.2}$$

This process was done 1,000 times to reduce the stochastic error as much as possible. This approximation yielded a value of $F_{\rm bol} = 1.064 \pm 0.002 \times 10^{-13}$ erg cm^{-2} s^{-1}. Having obtained the bolometric flux, further calculations were carried out to determine the total luminosity of the accretion disc.

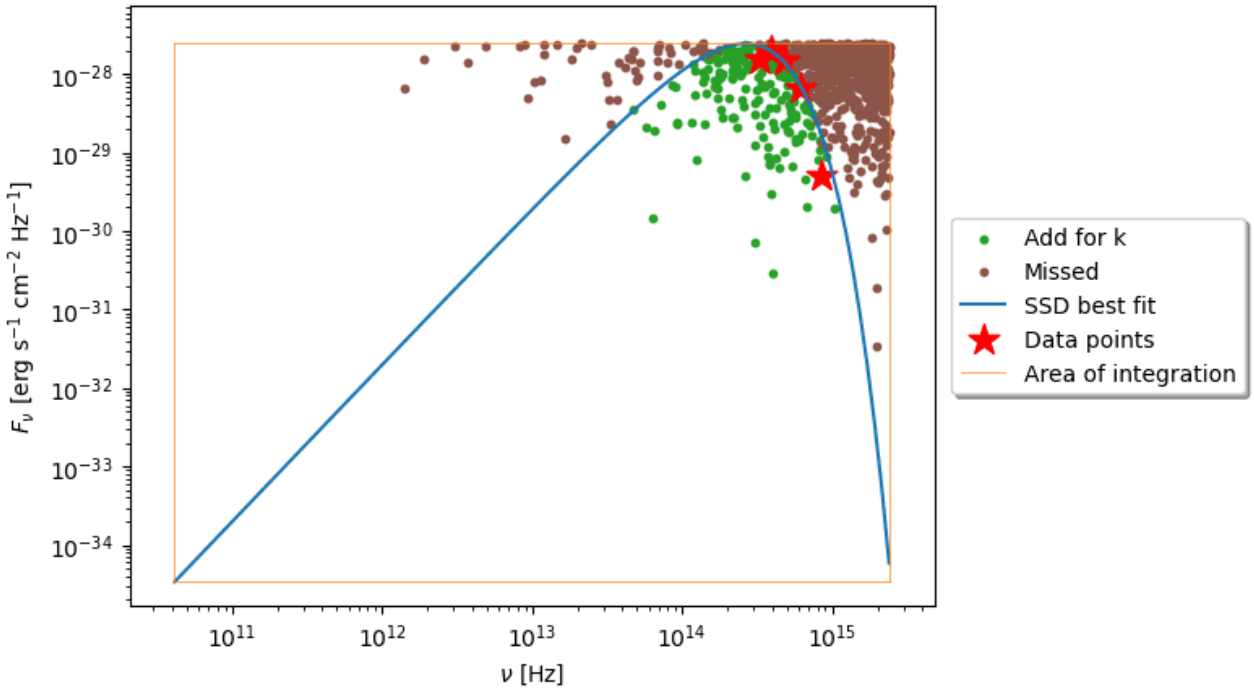

Figure 3.3. Best fit of a multicolor blackbody spectra for the emission points coming the accretion disc, as well as the Monte Carlo integration method.

Expanding upon the concepts presented in § 2, we proceeded to estimate the value of $L_{\rm disc}$ by incorporating the redshift of our observed source by using the following formula:

$$L_{\rm disc} = 4\pi D_L^2 F_{\rm bol} \tag{3.3}$$

Here, D_L^2 signifies the squared luminosity distance, serving as a well-defined measure of distance between two arbitrary points in spacetime. Applying this formula and considering the specific redshift value for our source ($z \approx 3.647763$; Pâris et al. (2018)), we successfully calculated $L_{\rm disc}$. For this particular phase of our investigation, we used the Cosmology Calculator provided by Wright (2006) to derive a value for D_L. This calculation accounted for a generalised λCDM (Lambda cold dark matter) model that incorporates a Hubble constant of $H_0 = 67.8$ km/s/Mpc, a matter density parameter of $\Omega_M = 0.307$, and a dark energy density parameter of $\Omega_\lambda = 0.693$ (Planck Collaboration, 2016). The resulting luminosity of the accretion disc was determined to be $L_{\rm disc} = 1.381 \pm 0.003 \times 10^{46}$ erg s^{-1}. This outcome offers essential insights into the energetics and overall behaviour of the accretion process within the investigated system. In fact, it is now possible to estimate a value for the SMBH mass, but as for what we have discussed, we would be missing insights from all the other regions of the SED. Therefore, to better model the central engine, we will proceed now by setting a set of different values for η which will result in different values for the SMBH mass, as these parameters are explicitly related by Equation 2.92. In particular,

we will use $\eta = 0.057, 0.083, 0.150, 0.200,$ and 0.300 to account for the possibility of having either a non-rotating Schwarzschild black hole, an extreme Kerr black hole, or spin values in between, as explained in Thorne (1974). This approximation to the problem of modelling the SED not only will give us a better calculation on the SMBH mass, but also it will give a better insight in the high-energy emissions of our blazar.

Therefore, considering the factors mentioned above and their implications, it becomes necessary to employ a new ad hoc prefit approach to more effectively characterise the blazar emissions. Specifically, due to the availability of a precise measurement of $L_{\rm disc}$, this parameter will be set as a lower limit, while a revised range of values will be defined for the remaining parameters.

3.4.2 Prefit Model

In our new prefit, considering the values obtained initially from the observables, we will consider a self-consistent model that takes into account these initial values. In this model, the size of the blob will be determined by a parameter based on a fixed opening angle, denoted as $\theta_{\rm open}$, and the distance between the dissipation region $R_{\rm diss}$ and the black hole. Specifically, the size can be calculated using the equation:

$$R = R_{\rm diss} \times \tan\theta_{\rm open} \tag{3.4}$$

This approach enhances the model's coherence, as it recognises that in a one-zone model, the blob should expand as it moves away from the central engine. In addition, with the accurate determination of a lower limit of $L_{\rm disc}$, an important consideration arises, namely the establishment of a relationship between the BLR and the DT radii, and $L_{\rm disc}$. This significant development allows us to seamlessly incorporate the DT and the BLR radius as additional parameters within our model, further refining its accuracy and comprehensiveness. Guided by the insights presented in Cleary et al. (2007) and Kaspi et al. (2007), we can assign specific values to $R_{\rm BLR_{in}}$, $R_{\rm BLR_{out}}$, and $R_{\rm DT}$, respectively, using the following expressions:

$$R_{\rm DT} = 2.00 \times 10^{19} \sqrt{\frac{L_{\rm disc}}{10^{46}}} \text{ cm} \tag{3.5}$$

$$R_{\rm BLR_{in}} = 3.00 \times 10^{17} \sqrt{\frac{L_{\rm disc}}{10^{46}}} \text{ cm} \tag{3.6}$$

$$R_{\rm BLR_{out}} = 1.10 \times R_{\rm BLR_{in}} \text{ cm} \tag{3.7}$$

Consequently, the incorporation of these radii as a function of $L_{\rm disc}$ enhances the overall reliability and effectiveness of our emission model, facilitating a more accurate and comprehensive characterisation of the physical processes at play.

By incorporating these concepts into the SED modelling, we can observe that we already possess a model that elucidates the underlying process responsible for each segment of the spectra (as demonstrated in Figure 3.4). At this stage, our focus shifts to fitting our model. Specifically, we are particularly interested in obtaining a good fit for the disc emissions, as they also define the high-energy portion of the spectra. To achieve this, we will initially employ a standard SSD model with a fixed efficiency parameter of $\eta = 0.083$. For this particular case, we established lower and upper limits for the electron energy distribution, setting $\gamma_{\text{min}} = 1.00$ and $\gamma_{\text{max}} = 2.00 \times 10^4$, respectively. We will continue to incorporate the aforementioned dependencies and allow the variables to assume values within a specified range, which are used in the literature. For the fitting, we will be using the `minuit` package which is the frequentist approach to the fitting.

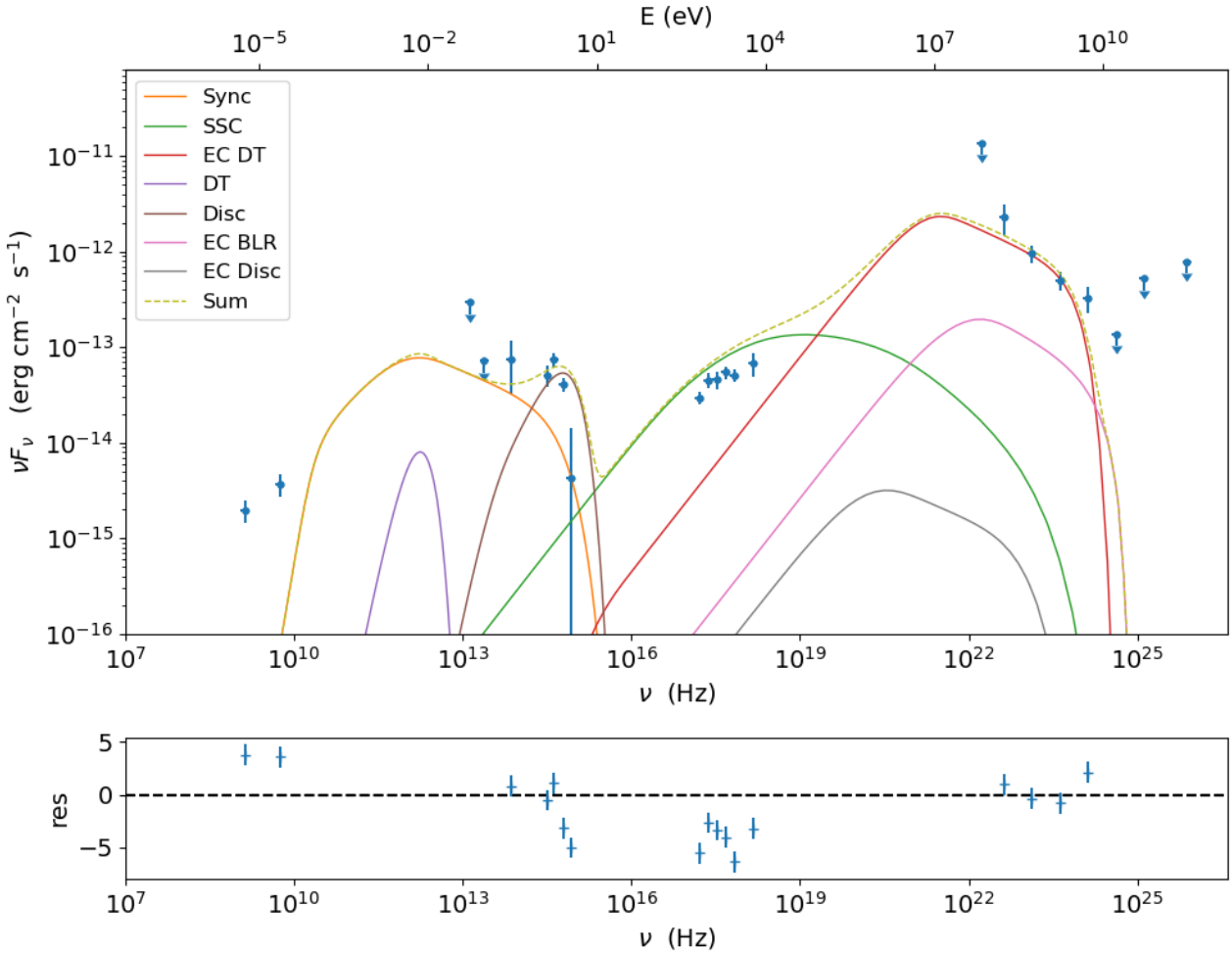

Figure 3.4. New prefit model considering a dependency in the radii of both the BLR and DT as a function of L_{disc}

After obtaining our prefit, which provides an initial understanding of the SMBH mass, we will explore various scenarios within our model to explain different values of η. Initial examination of Equations 2.92 & 2.114 suggests that altering η will result in proportional changes in $L_{\rm disc}$, thus influencing the contributions of EC emissions from the BLR and DT. As our emission zone moves closer or farther away from these regions, the energy density of photons in each respective region will increase or decrease, leading to observable changes at high energies. In relation to this matter, Costamante et al. (2018) explain that a higher contribution in the γ-rays from the DT is expected, particularly for larger values of η (indicating higher $L_{\rm disc}$), as this creates a stronger radiative pressure capable of forming the CND. In their analysis of the Fermi $\gamma-$ray spectra of 106 FSRQs with significant BLR luminosities and sizes, they showed no evidence of the anticipated BLR absorption resulting from $\gamma - \gamma$ interactions with BLR photons. In approximately two-thirds of the sources, significant absorption was excluded, indicating that the maximum optical depth at the peak of the $\gamma - \gamma$ cross section was less than 1. For the remaining one-third, possible absorption was constrained to be 1.5-2 orders of magnitude lower than expected. As a result, it is inferred that in 90% of the cases, the jet does not interact with BLR photons. This suggests that γ-rays are primarily produced outside the BLR or that the BLR is approximately 100 times larger than estimated through reverberation mapping; meaning the DT should be the seed of the external photons. Figure 3.5 illustrates the model employing a standard SSD, while Table 3.3 presents the corresponding parameter values.

Parameter	**Value**	**Units**	**Model component**
R	7.86	10^{16} cm	Blob
$R_{\rm diss}$	1.50	10^{18} cm	Blob
B	5.56	10^{-2} G	Blob
θ	3.00	deg	Jet viewing angle
Γ	1.90	10^{1}	Jet bulk factor
δ	1.91	10^{1}	Beaming factor
$\gamma_{\rm min}$	1.00		LE cut-off
$\gamma_{\rm break}$	9.46	10^{2}	Turn over energy
$\gamma_{\rm max}$	2.00	10^{4}	HE cut-off
N	9.21	10^{2} cm^{-3}	Emitters density
p	1.45		LE spectral slope
p_1	3.58		HE spectral slope
$R_{\rm in}$	9.27	$R_{\rm S}$	Disc
$R_{\rm out}$	8.41	$10^{2}R_{\rm S}$	Disc
M_{BH}	1.10	$10^{9}M_{\odot}$	Disc
η	8.30	10^{-2}	Disc
$L_{\rm disc}$	1.41	10^{46} erg s^{-1}	Disc
$R_{\rm DT}$	2.37	10^{19} cm	DT
$T_{\rm DT}$	9.27	10^{2} K	DT
$\tau_{\rm DT}$	0.10		DT
$R_{\rm BLR_{in}}$	3.56	10^{17} cm	BLR
$R_{\rm BLR_{out}}$	3.92	10^{17} cm	BLR
$\tau_{\rm BLR}$	0.10		BLR

Table 3.3. SED model values using a SSD for J163547+362930, Figure 3.5.

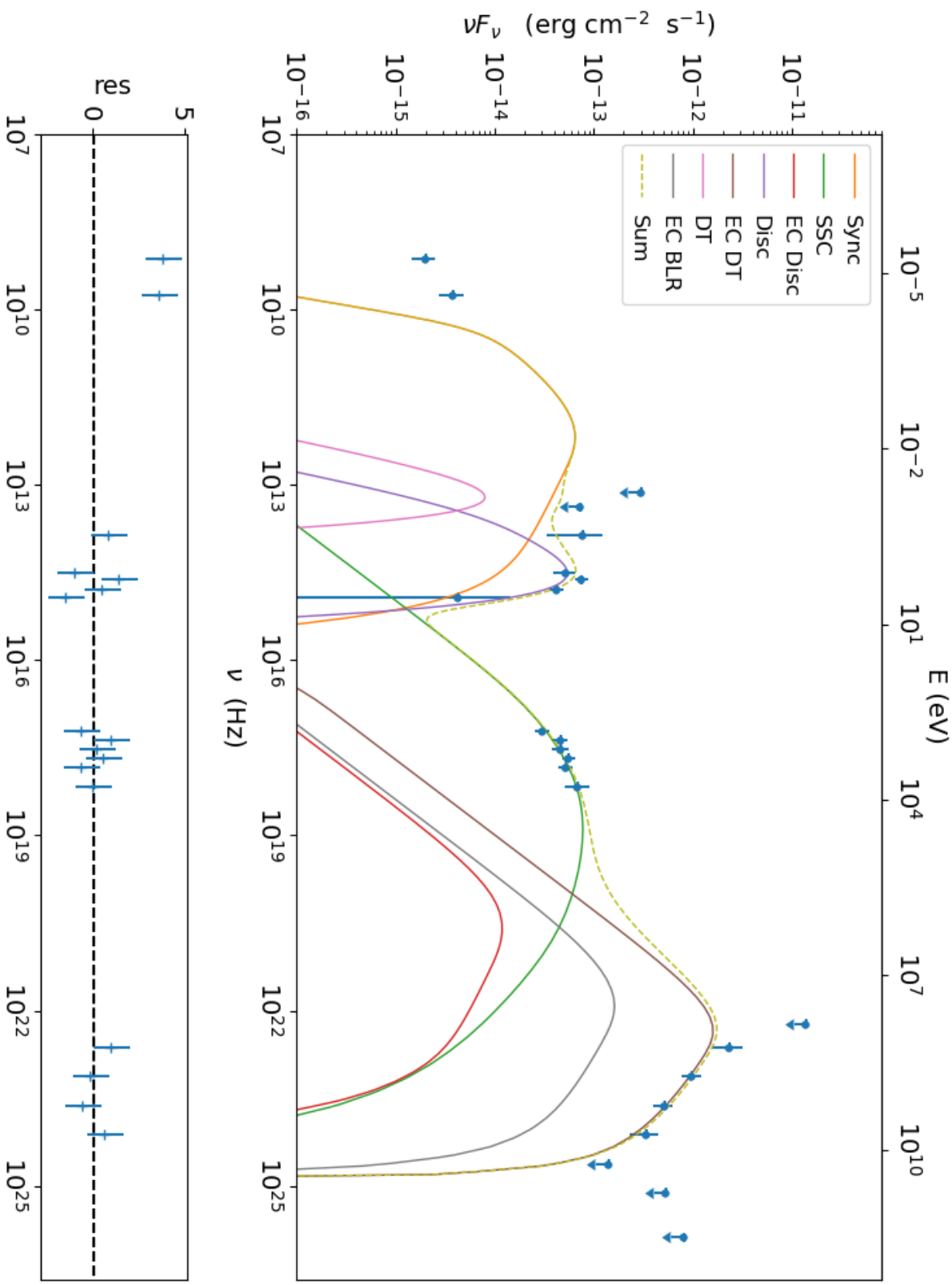

Figure 3.5. SED for J163547+362930 using a SSD which parameters can be seen in Table 3.3

3.4.3 Different Accretion Efficiencies

Using our new prefit model, we will proceed to fit the SED using a specific set of η values. To ensure that the fit avoids non-physical values, we have established minimum and maximum values for each parameter, as indicated in Table 3.4. These values align with our assumptions, initial insights on the disc luminosity, and the relevant literature. Consequently, by exploring various efficiency values, we can investigate how the overall parameters of the system will be affected.

Parameter	**Min value**		**Max value**	**Units**
R	0.26	-	1.57	10^{17} cm
$R_{\rm diss}$	0.50	-	3.00	10^{18} cm
B	0.10	-	1.00	10^{-1} G
Γ	1.00	-	2.50	10^{1}
$\gamma_{\rm break}$	0.50	-	3.00	10^{3}
p	1.40	-	1.60	
p_1	3.30	-	3.50	
M_{BH}	0.50	-	2.00	$10^{9} M_{\odot}$
$L_{\rm disc}$	0.80	-	8.00	10^{46} erg s^{-1}
$R_{\rm DT}$	1.79	-	5.66	10^{19} cm
$R_{\rm BLR_{in}}$	2.68	-	8.49	10^{17} cm
$R_{\rm BLR_{out}}$	2.95	-	9.33	10^{17} cm

Table 3.4. Parameter ranges for SED modelling within the realm of various black hole types in consideration.

For the fitting process, we will again utilise the `minuit` package, which will also provide the necessary information for performing inference on the probability distributions of our main parameters using Markov Chain Monte Carlo (MCMC) techniques. Taking into account the discussion presented in the previous section, it was initially hypothesised that a satisfactory fit could be achieved for different models by keeping all parameters fixed except for $R_{\rm diss}, B, L_{\rm disc}$, and M_{BH}. We then set the values of these parameters while keeping η constant to optimise the contributions from the accretion disc and ensure a faster convergence of the fitting process.

Our hypothesis was that modifying η would cause a proportional change in $L_{\rm disc}$. The reader may also think that this is not completely true; it can also be thought that by changing η what would be needed to change is $R_{\rm in}$ (i.e., $T_{\rm max}$) and not $L_{\rm disc}$ as the latter is more dominant on the first, as can be seen in Equations 2.120 & 2.121. Nevertheless, when this approach was taken, it was clear that what was changing was the peak position of the multicolour blackbody and not the $F_{\rm bol}$. From this, by trying different values for $R_{\rm diss}$ it was possible to obtain a good ad hoc fit, particularly on these emissions. In particular, we found that it was not necessary to

drastically alter the value of M_{BH} to achieve a good fit to the data. With these parameters set, we began the fitting process, anticipating a successful modelling of the SED. However, upon performing this approach, a good fit was solely attained for emissions within the X-ray range. Therefore, to achieve a more accurate fit, it became necessary to also free the parameters that influence the electron energy distribution, particularly p, p_1, N, and γ_{break}. It is worth noting that the dependencies previously established for the BLR and DT radii, as well as the ratio between R and R_{diss}, will still be utilised to ensure that the model remains within the realm of physical plausibility.

In Figure 3.6, which shows the sum of all components responsible for the SED, we can observe the different outcomes of our model considering various values for η based on the assumptions discussed. The parameter values for each model are shown in Table 3.5. It is evident from the figure that the uncertainty of the models lies primarily in the energy ranges where no data are available, particularly at the low-energy peak and in the hard X-ray energy range. Nevertheless, it is now evident that different values for the accretion efficiency, that is, different models for the SMBH, can be used to model the SED. With this newfound information, we can not only achieve more accurate estimations of the main parameters for the model, but also gain valuable insights into the early evolution of the SMBH and its nuclear environment, taking into account different types of SMBHs.

Parameter	Value						**Units**	**Model component**	**Frozen**
η	0.57	0.83	1.00	1.50	2.00	3.00	10^{-1}	Disc	True
R	0.63	0.79	0.94	1.10	1.22	1.42	10^{17} cm	Blob	False
$R_{\rm diss}$	1.20	1.50	1.80	2.10	2.33	2.70	10^{18} cm	Blob	False
B	7.95	6.56	4.05	2.16	1.90	2.23	10^{-2} G	Blob	False
θ	3.00	3.00	3.00	3.00	3.00	3.00	deg	Jet viewing angle	True
Γ	2.00	1.90	1.57	1.32	1.32	1.52	10^{1}	Jet bulk factor	True
δ	1.91	1.91	1.87	1.78	1.79	1.86	10^{1}	Beaming factor	True
$\gamma_{\rm min}$	1.00	1.00	1.00	1.00	1.00	1.00		LE cut-off	False
$\gamma_{\rm break}$	0.88	0.94	1.07	1.24	1.28	1.23	10^{3}	Turn over energy	True
$\gamma_{\rm max}$	2.00	2.00	2.00	2.00	2.00	2.00	10^{4}	HE cut-off	False
N	11.48	9.21	7.70	9.01	8.17	6.03	10^{2} cm^{-3}	Emitters density	False
p	1.42	1.45	1.41	1.41	1.41	1.45		LE spectral slope	False
p_1	3.61	3.58	3.65	3.68	3.66	3.63		HE spectral slope	False
$R_{\rm in}$	9.27	9.27	9.27	9.27	9.27	9.27	$10^{1} R_{\rm S}$	Disc	True
$R_{\rm out}$	8.41	8.41	8.41	8.41	8.41	8.41	$10^{2} R_{\rm S}$	Disc	True
M_{BH}	1.15	1.10	1.24	1.46	1.30	1.15	$10^{9} M_{\odot}$	Disc	False
$L_{\rm disc}$	0.99	1.41	1.99	3.37	4.22	5.78	10^{46} erg s^{-1}	Disc	False
$R_{\rm DT}$	1.99	2.37	2.82	3.67	4.11	4.81	10^{19} cm	DT	False
$T_{\rm DT}$	9.27	9.27	9.27	9.27	9.27	9.27	10^{2} K	DT	True
$\tau_{\rm DT}$	1.00	1.00	1.00	1.00	1.00	1.00		DT	True
$R_{\rm BLR_{in}}$	2.98	3.56	4.23	5.51	6.17	7.21	10^{17} cm	BLR	False
$R_{\rm BLR_{out}}$	3.28	3.92	4.66	6.06	6.78	7.93	10^{17} cm	BLR	False
$\tau_{\rm BLR}$	1.00	1.00	1.00	1.00	1.00	1.00		BLR	True

Table 3.5. SED model values using a set of accretion efficiencies for the SED of J163547+362930, Figure 3.6.

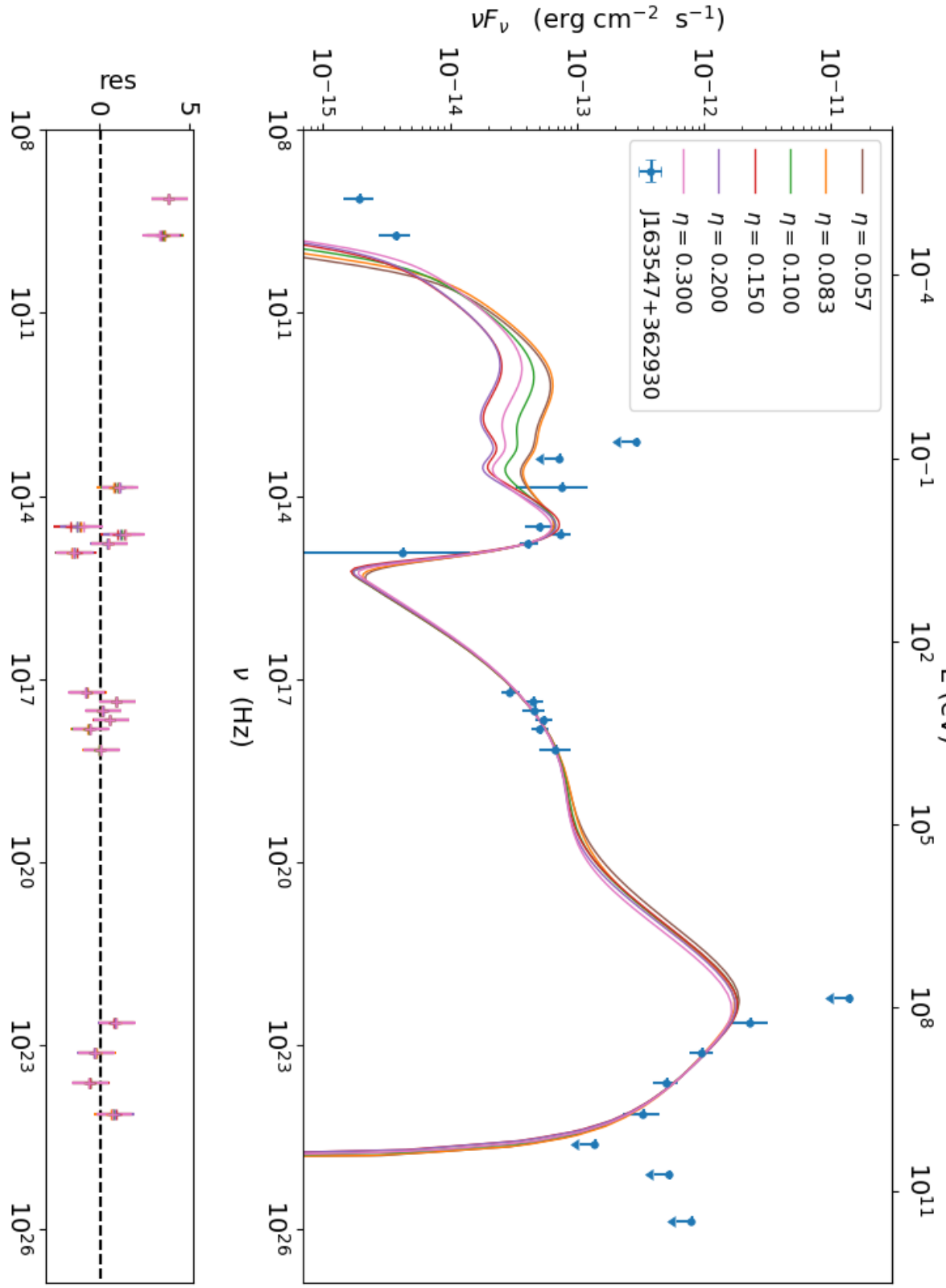

Figure 3.6. Different outcomes for the SED at different values of the accretion efficiency. The values of each parameter are shown in Table 3.5

Chapter 4

Discussions and Conclusion

This chapter presents a comprehensive analysis of our results and models obtained in the previous chapter. We highlight the use of the MCMC sampling technique for parameter estimation. Additionally, a theoretical framework for the formation and evolution of SMBHs is presented. The chapter further showcases the intrinsic correlation between the accretion luminosity and the total jet power. Furthermore, crucial future steps in characterising the SMBH and its nuclear environment in NVSS J163547+362930 during the early universe are mentioned. Finally, we conclude the work by synthesising the implications of our findings and mapping a trajectory for future investigations in this field.

4.1 Markov-Chain Monte Carlo Sampling

It should be clear now that leptonic (but also hadronic) models for blazars SED are challenging to model. Standard chi-square minimisation methods often fall short in effectively constraining the model parameters due to their high dimensionality, parameter degeneracies, local minima, and model-specific dependencies, including electron distribution parameters and Lorentz factors. As a result, employing Markov-Chain Monte Carlo (MCMC) methods, by performing a maximum likelihood test, to fit and explore the SED's parameter space is always considered a prudent approach.

MCMC combines two fundamental concepts: Monte Carlo and Markov chain. Monte Carlo techniques use random numbers to generate samples from a probability distribution, enabling the estimation of expectations for functions under this distribution. On the other hand, Markov chains represent a sequence of states where each state has a probability distribution dependent on the previous value. MCMC methods create Markov chains that eventually reach an equilibrium distribution that matches the desired probability distribution. In this thesis, we do not aim at delving into the general statistical concepts behind MCMC methods. However, for a comprehensive understanding, interested readers can refer to MacKay (2003),

which extensively discusses these concepts and beyond. Instead, we will briefly introduce the core idea of MCMC and provide an overview of the `emcee` algorithm.

4.1.1 emcee Framework

Since successive samples in the chain are correlated, it can take a considerable amount of time to generate effectively independent samples from the target distribution. In our project, we used the MCMC package called `emcee` (e.g., Foreman-Mackey et al. (2013)). This package requires a user-defined log probability function to evaluate the goodness of a fit, particularly a Chi-squared fit test. The posterior probability density function is then automatically constructed using a specified number of steps (iterations), walkers (exploring the state space), and a defined burn-in sample (to approach the equilibrium distribution).

The maximum-likelihood approach determines the best-fitting model to establish confidence regions in the parameter space. For our specific case, using the formalism portrayed in Sawicki (2012), we first defined a likelihood function, which represents the probability of the data set given the model parameters, and then numerically optimised it. The likelihood function is expressed as:

$$\ln p(f_d|f_m) = -\frac{1}{2}\sum_i \left(\frac{f_{d,i} - f_{m,i}}{\theta_i}\right)^2 + g_i(f_{\mathrm{UL}}) \tag{4.1}$$

where f_d represents the data, f_m the model, θ the data error, and $g(f_{\mathrm{UL}})$ returns the error function when considering the upper limits (UL) which is defined as

$$g(f_{\mathrm{UL}}) = -2\sum_j \ln \int_{-\infty}^{f_{\mathrm{UL},j}} \exp\left[-\frac{1}{2}\left(\frac{f - f_{m,j}}{\sigma_j}\right)^2\right] df \tag{4.2}$$

The assumption is that the errors are Gaussian and independent, which of course, is not the case in real life. Nevertheless, due to the fact that we are collecting data from different instruments with different response functions, this assumption is not an oversimplification. Maximising the likelihood that the observed dataset (detections and non-detections) is drawn from the given model is equivalent to minimising the sum inside the likelihood function. Thus, considering Equation 4.2, we can define

$$\chi^2 = \sum_i \left(\frac{f_{d,i} - f_{m,i}}{\theta_i}\right)^2 - 2\sum_j \ln\left[\sqrt{\frac{\pi}{2}}\sigma_j\left(1 + \mathrm{erf}\left(\frac{f - f_{m,j}}{\sqrt{2}\sigma_j}\right)\right)\right] \tag{4.3}$$

where the second integral from Equation 4.2 is written in terms of the error function, $\mathrm{erf}(x) = (2/\pi)\int_0^x e^{-t^2} dt$. From here, by using a Bayesian data analysis, it is possible to start

constructing the posterior probability function

$$p(f_m|f_d) \propto p(f_m)p(f_d|f_m) \tag{4.4}$$

in which is clear we will need to define the probability $p(f_m)$, the prior. For this case we used a flat prior which demands that $p(f_m)$ be kept at a constant value centred on the best-fit value for each parameter. When obtaining the samples from the MCMC process, we can estimate the constraints on the parameters f by creating a histogram of these samples projected into the parameter subspace defined by the model. This histogram provides an approximate representation of the distribution of possible values for the parameters, allowing us to understand the range and likelihood of different f_m values. Hence, the expectation value of a function of the model parameters $F(f_m)$ is:

$$\langle F\left(f_m\right)\rangle = \int p(f_m|f_d)F(f_m)df_m \sim \sum_i F(f_{m,i}) \tag{4.5}$$

Once these functions where all defined, we used the simplest and most commonly used MCMC algorithm, the Metropolis-Hastings (M-H) algorithm (e.g., Gregory (2005), Hogg et al. (2010), and MacKay (2003) encoded in the `emcee` package, to perform our analysis. In particular, we used the same approach for all our models, namely: a flat prior centred on the best fit value within the interval [best fit value $-\ \delta_m$, best fit value $+\ \delta_p$], with $\delta_m = \delta_p = 5 \times$ best fit value, a burn-in run of 10 steps to approach the equilibrium distribution, with 175 walkers, and finally a production run of 75 steps. The results, which will be used in the subsequent sections of this chapter, can be found in Table 4.1, as well as in Figures 4.1 to 4.12. Specifically, we showcase the MCMC model confined within the 5% and 95% confidence intervals of the SED. In addition, we provide corner plots that show the distributions of variables such as N, M_{BH}, $R_{\rm diss}$, B, $L_{\rm disc}$, and the Bulk Lorentz Factor Γ.

η	0.057	0.083	0.100	0.150	0.200	0.300
$N(10^2\ \mathrm{cm}^{-3})$	$11.50^{+1.29}_{-1.06}$	$9.01^{+1.30}_{-1.14}$	$7.55^{+1.27}_{-1.13}$	$8.74^{+1.28}_{-1.56}$	$7.98^{+1.26}_{-1.15}$	$6.02^{+1.04}_{-0.92}$
$M_{BH}(10^9 M_\odot)$	$1.19^{+0.23}_{-0.18}$	$1.13^{+0.23}_{-0.17}$	$1.27^{+0.29}_{-0.24}$	$1.43^{+0.19}_{-0.19}$	$1.32^{+0.29}_{-0.26}$	$1.07^{+0.24}_{-0.19}$
$R_{\rm diss}(10^{18}\ \mathrm{cm})$	$1.23^{+0.31}_{-0.19}$	$1.52^{+0.44}_{-0.28}$	$1.81^{+0.49}_{-0.29}$	$2.13^{+0.41}_{-0.31}$	$2.45^{+0.68}_{-0.43}$	$2.76^{+0.53}_{-0.41}$
$B(10^{-2}\ \mathrm{G})$	$7.89^{+0.12}_{-0.10}$	$6.69^{+0.13}_{-0.09}$	$4.13^{+0.74}_{-0.63}$	$2.22^{+0.45}_{-0.28}$	$1.94^{+0.35}_{-0.29}$	$2.94^{+0.59}_{-0.50}$
$L_{\rm disc}(10^{46}\ \mathrm{erg\ s}^{-1})$	$1.00^{+0.12}_{-0.12}$	$1.41^{+0.18}_{-0.18}$	$2.01^{+0.25}_{-0.24}$	$3.30^{+0.35}_{-0.32}$	$4.22^{+0.56}_{-0.57}$	$5.72^{+0.81}_{-0.63}$
$\Gamma(10^1)$	$2.00^{+0.22}_{-0.24}$	$1.89^{+0.24}_{-0.20}$	$1.56^{+0.12}_{-0.10}$	$1.33^{+0.12}_{-0.11}$	$1.32^{+0.13}_{-0.10}$	$1.48^{+0.15}_{-0.15}$

Table 4.1. The models were subjected to MCMC sampling. Specifically, the provided values correspond to the 16th, 50th, and 84th percentiles of samples within the marginalised distributions.

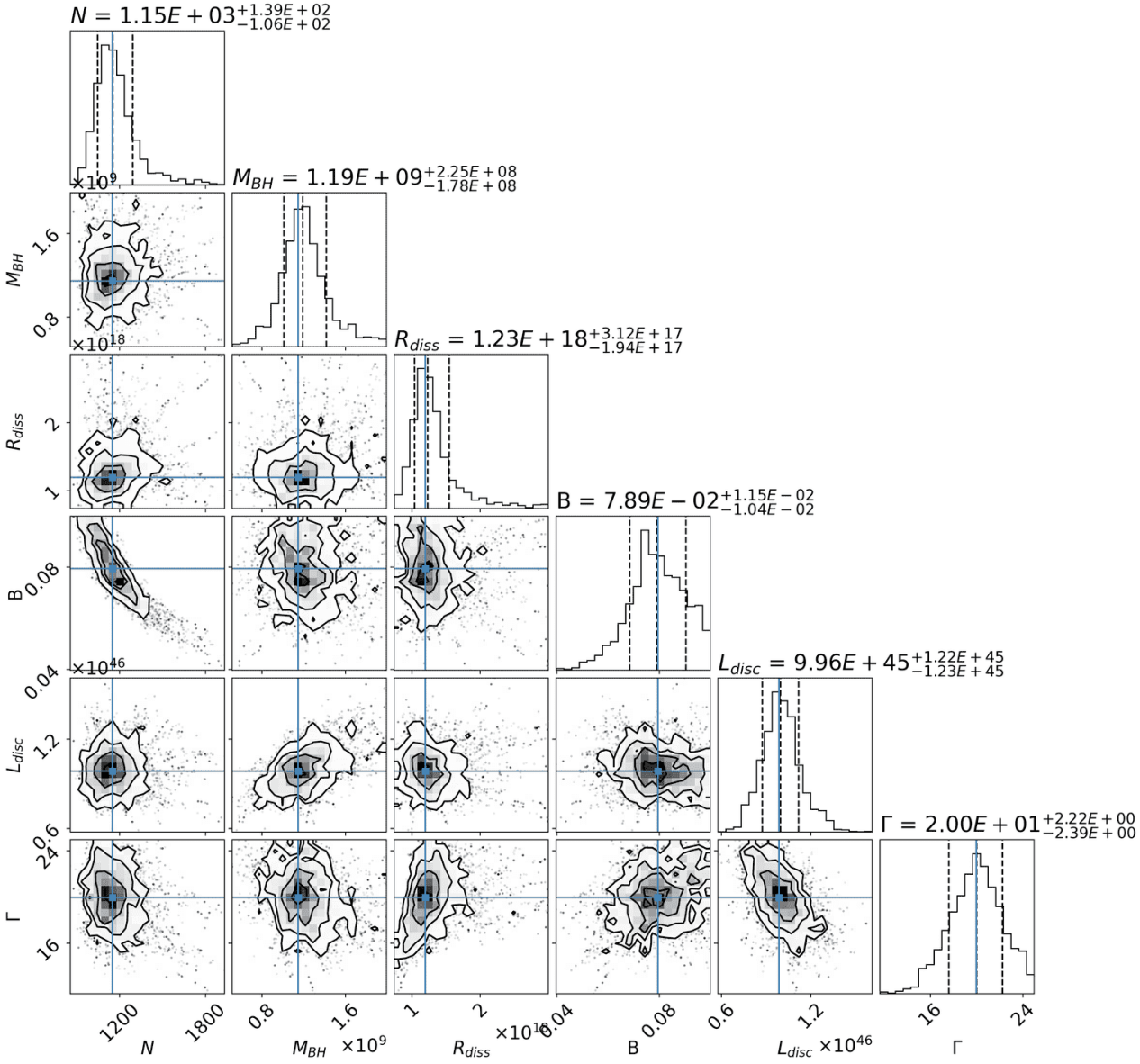

Figure 4.1. Corner plot for model with $\eta = 0.057$.

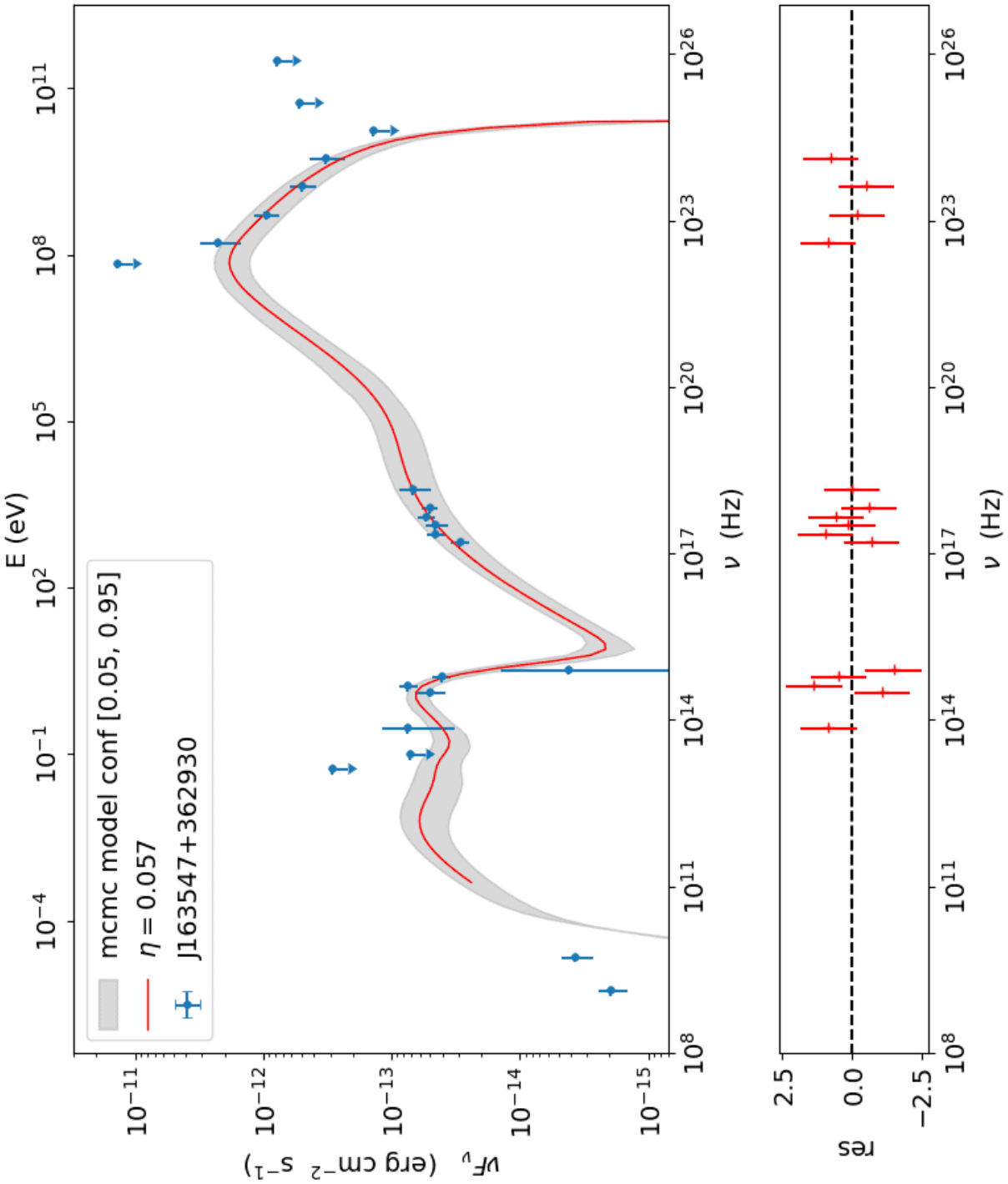

Figure 4.2. MCMC projection for model with $\eta = 0.057$.

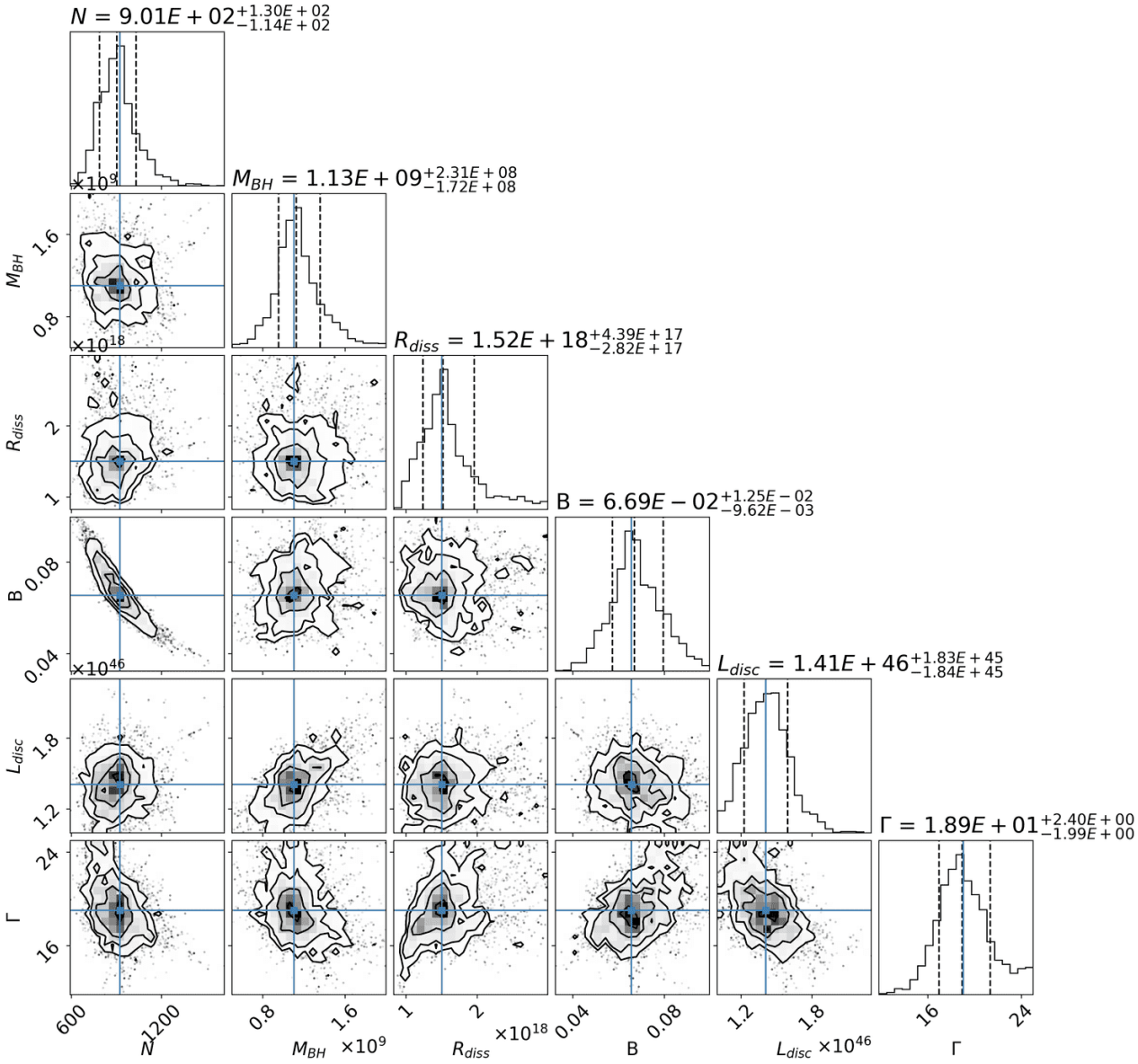

Figure 4.3. Corner plot for model with $\eta = 0.083$.

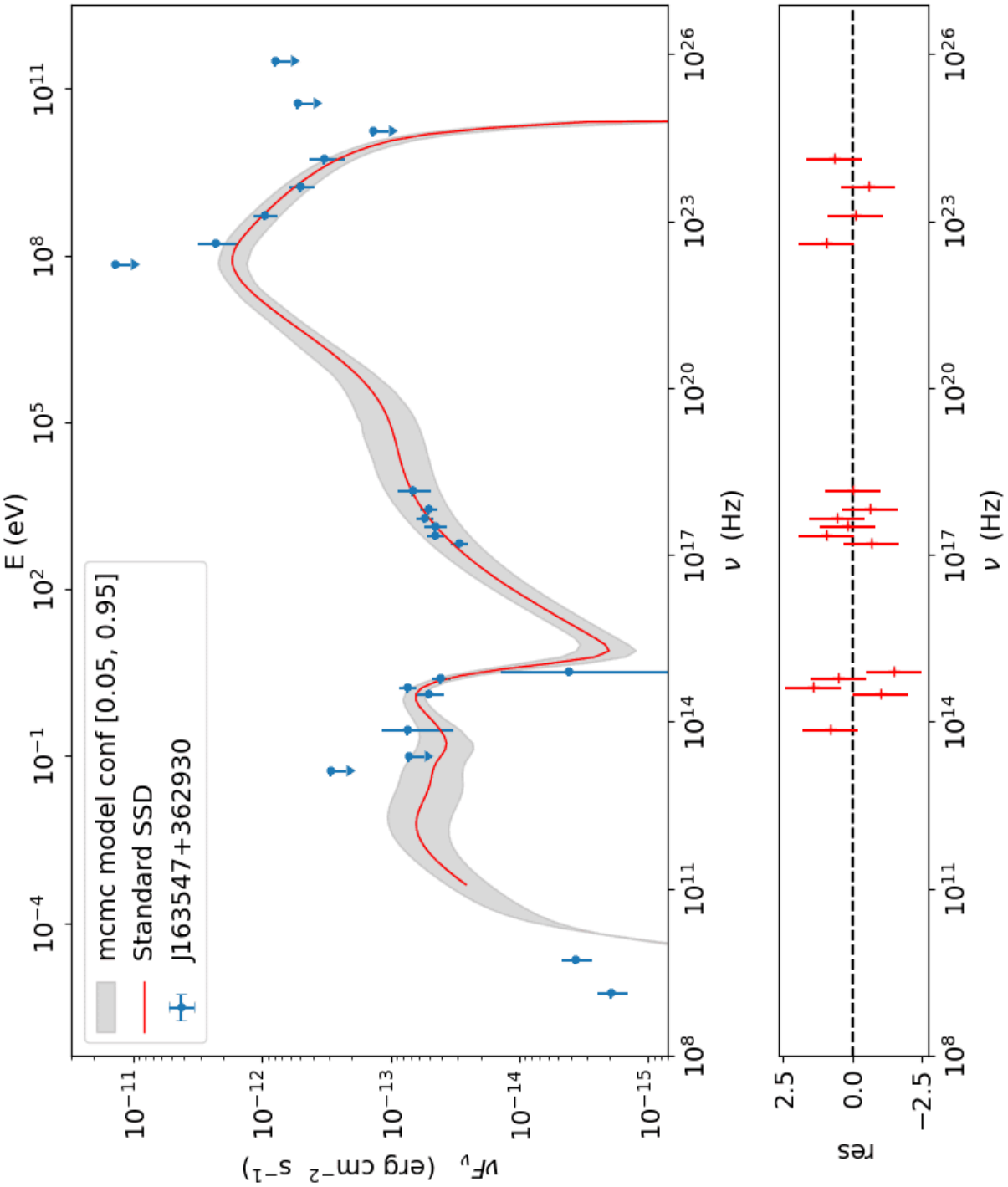

Figure 4.4. MCMC projection for model with $\eta = 0.083$.

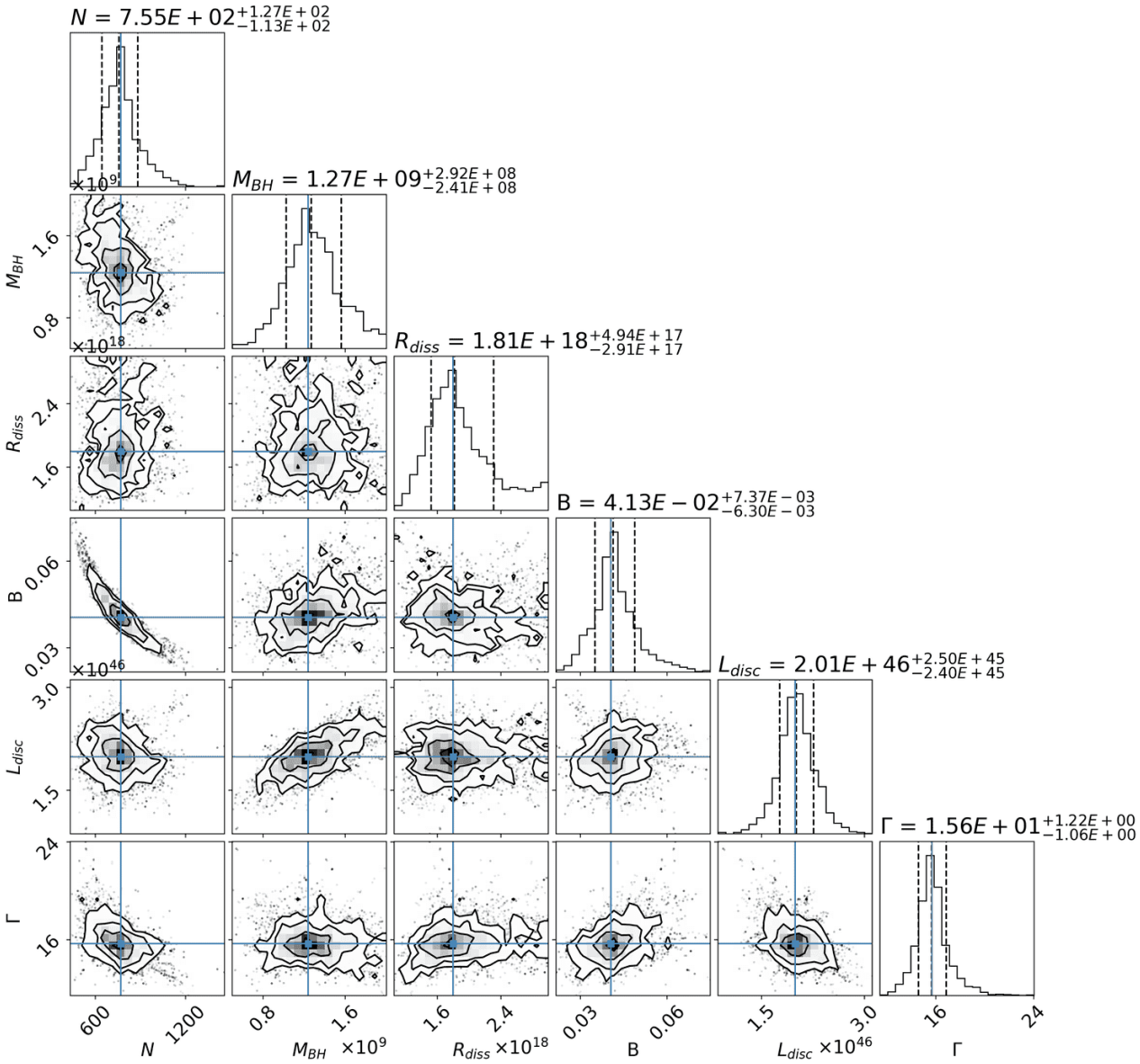

Figure 4.5. Corner plot for model with $\eta = 0.100$.

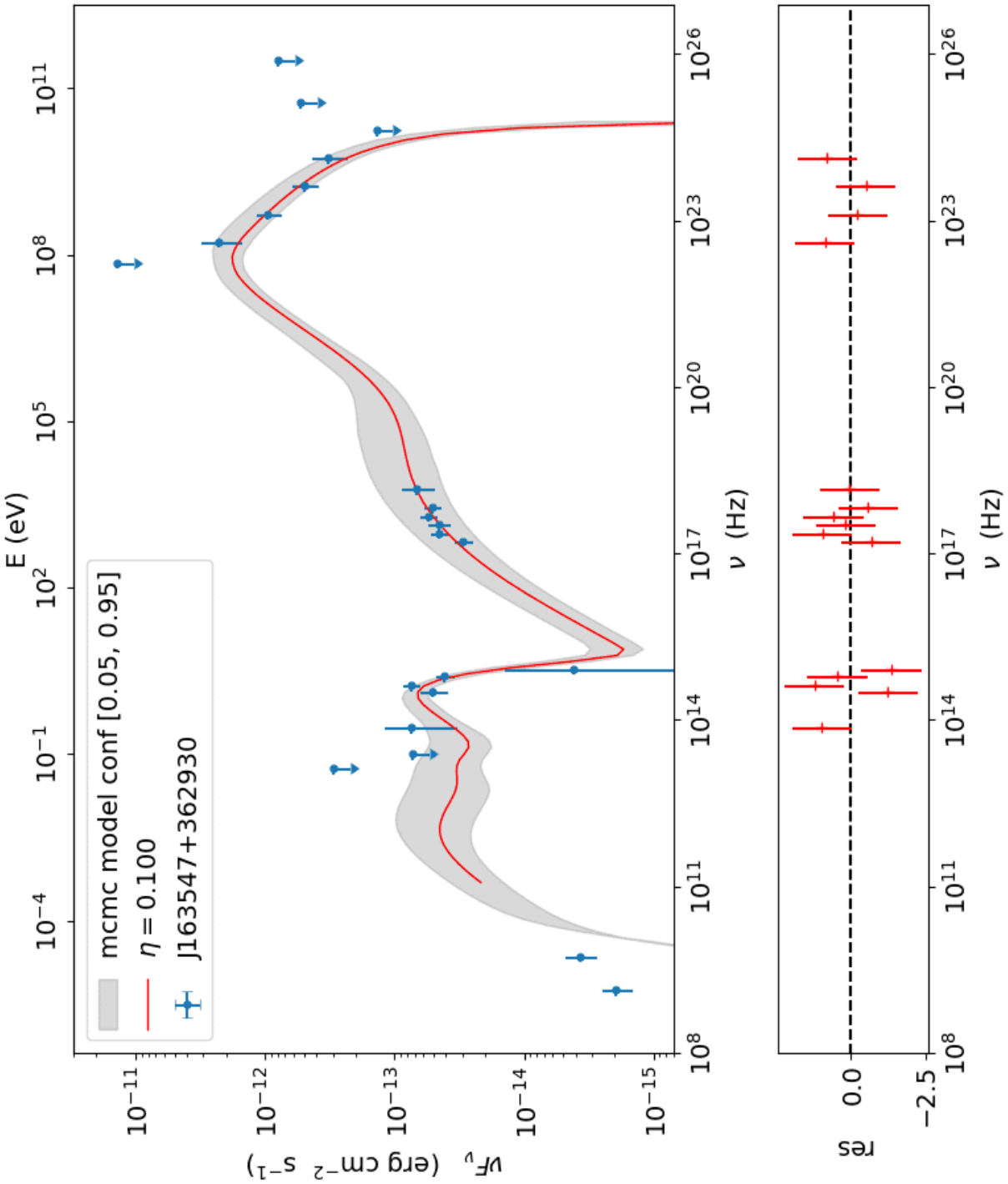

Figure 4.6. MCMC projection for model with $\eta = 0.100$.

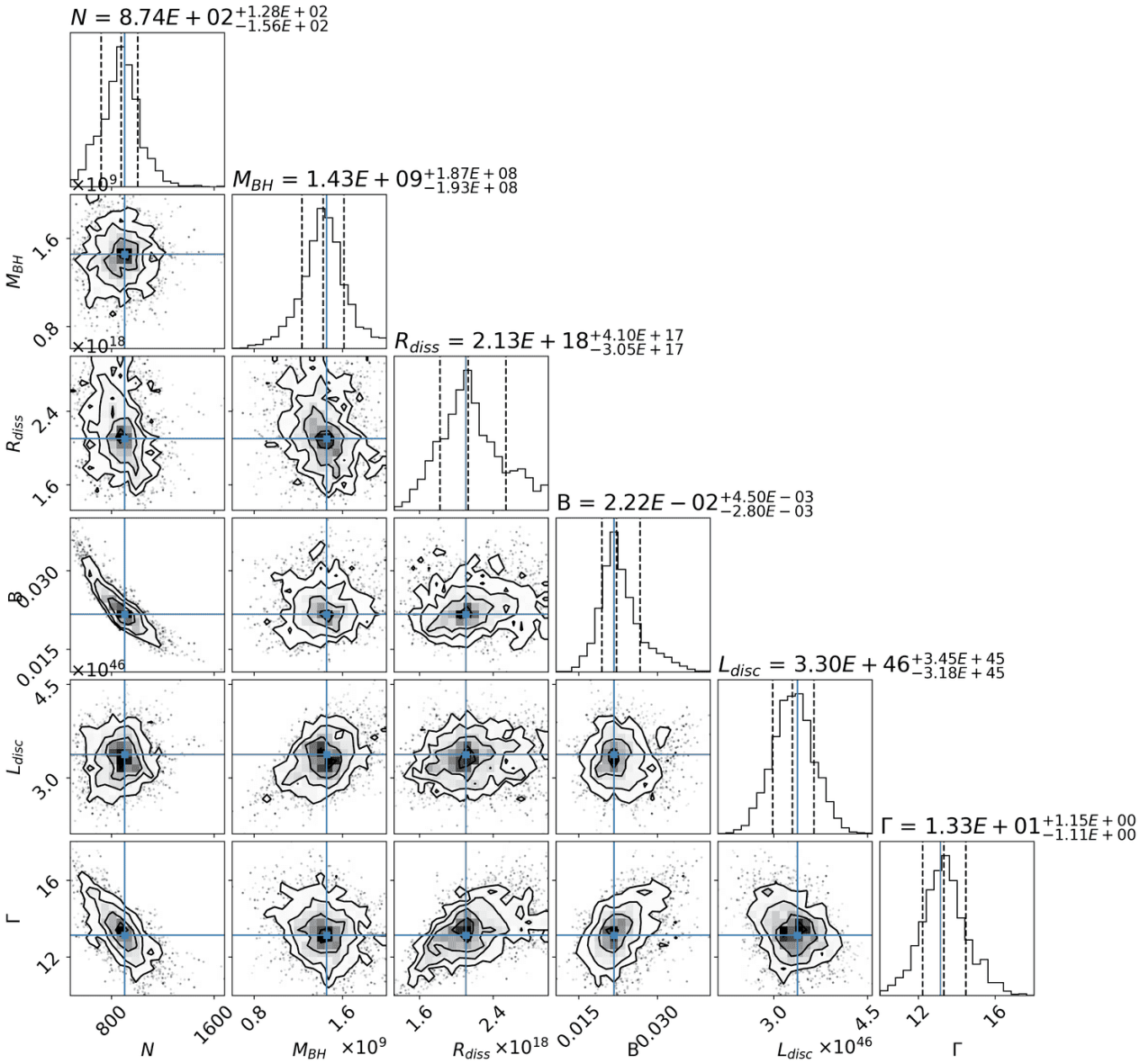

Figure 4.7. Corner plot for model with $\eta = 0.150$.

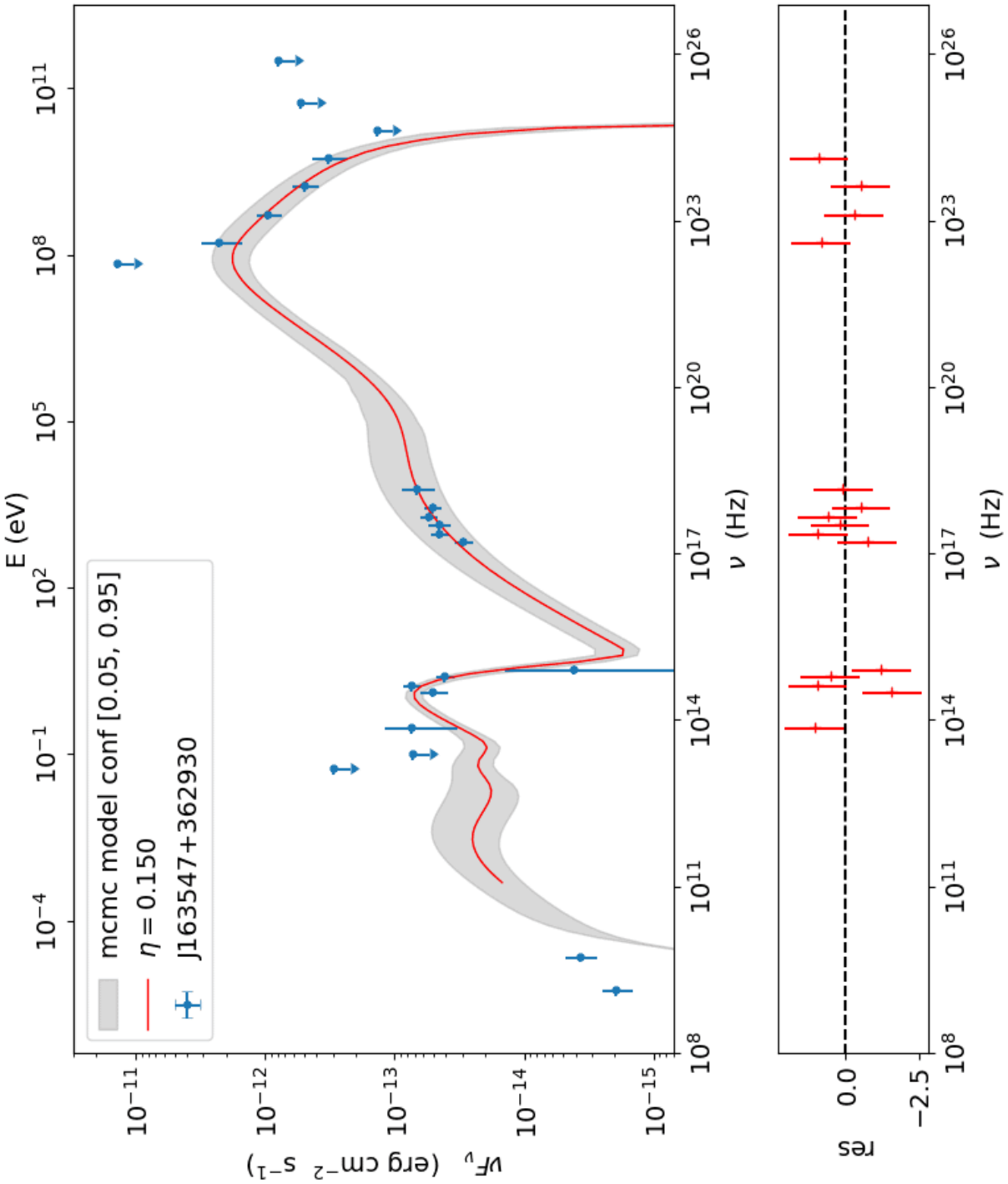

Figure 4.8. MCMC projection for model with $\eta = 0.150$.

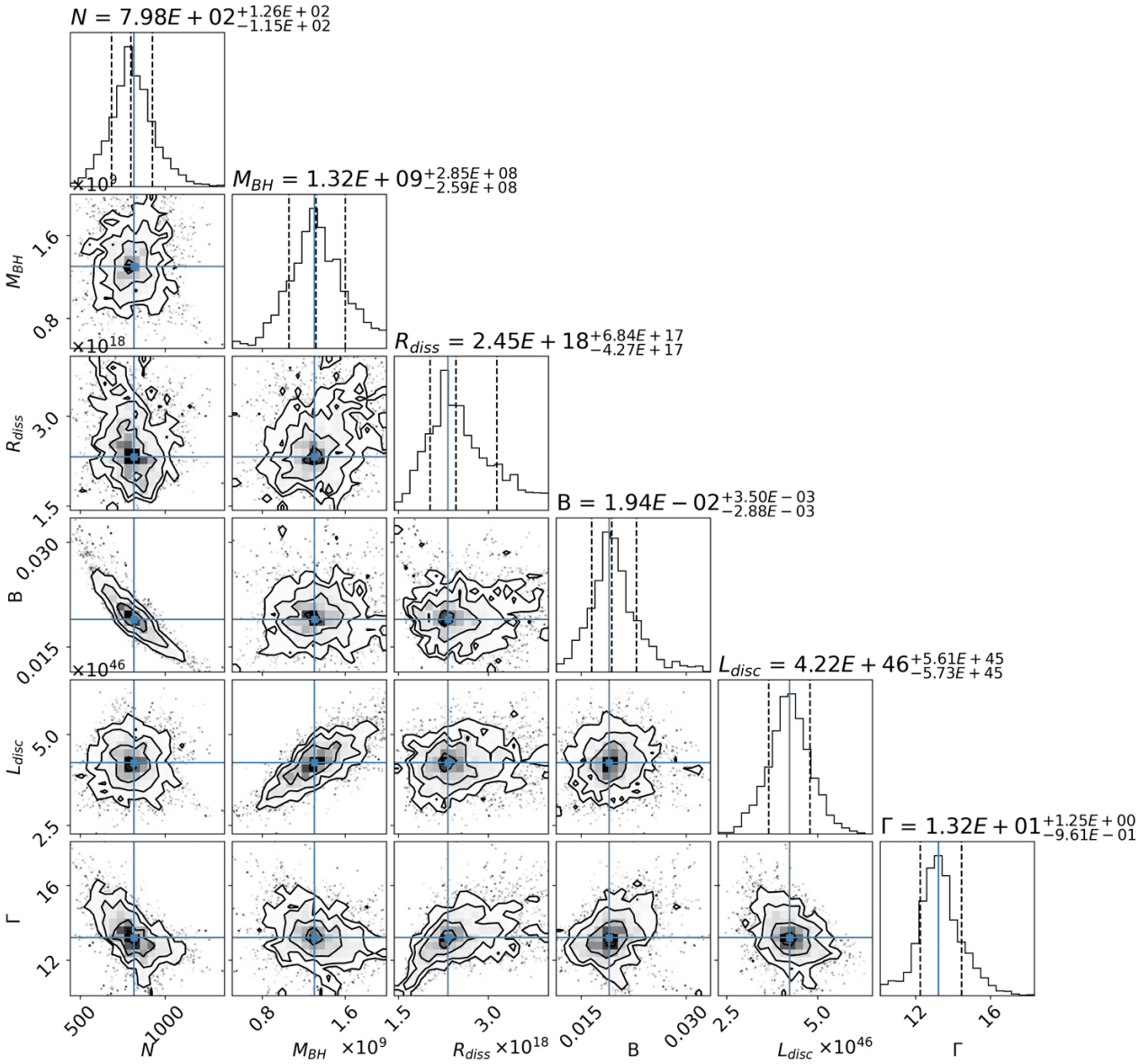

Figure 4.9. Corner plot for model with $\eta = 0.200$.

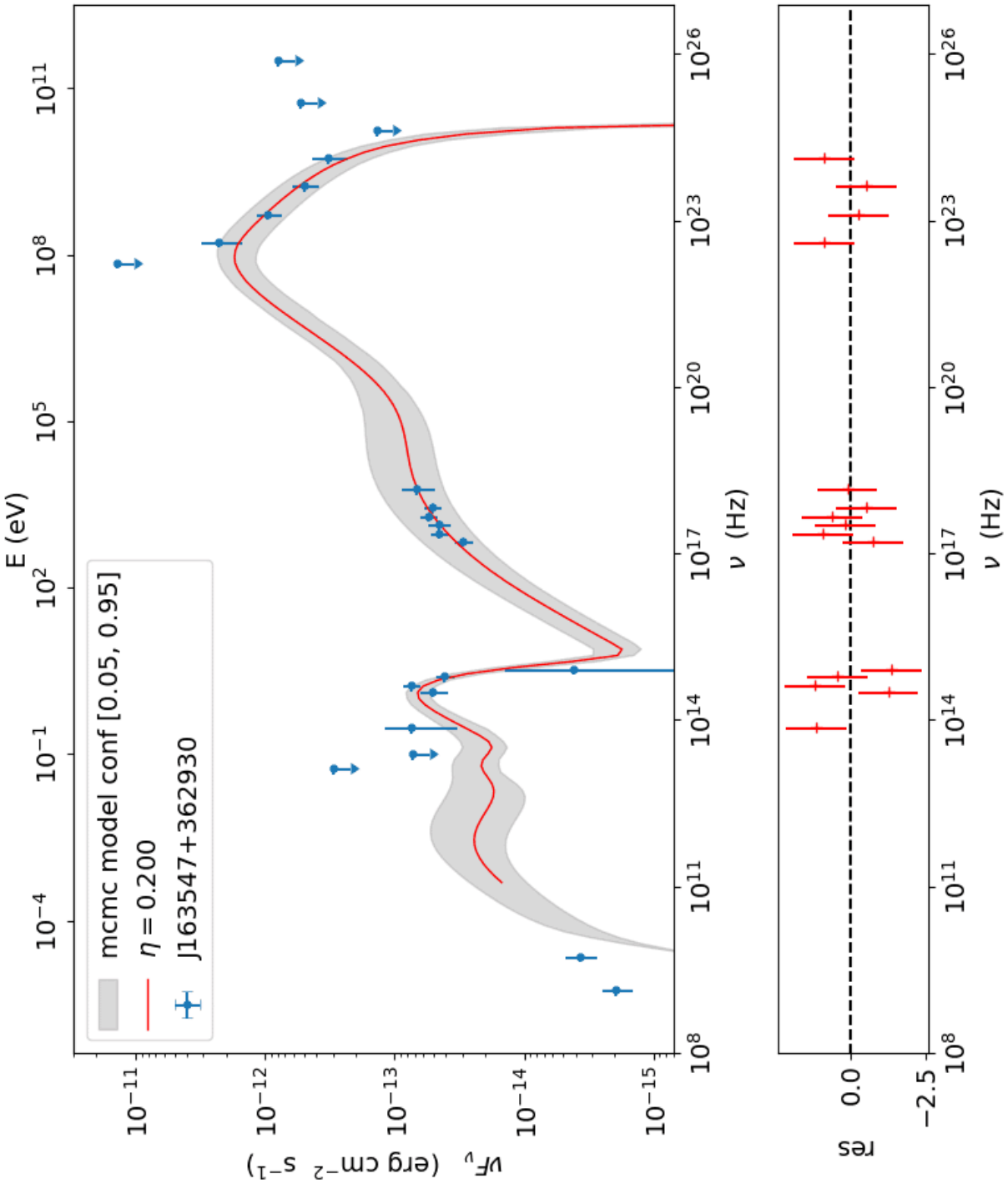

Figure 4.10. MCMC projection for model with $\eta = 0.200$.

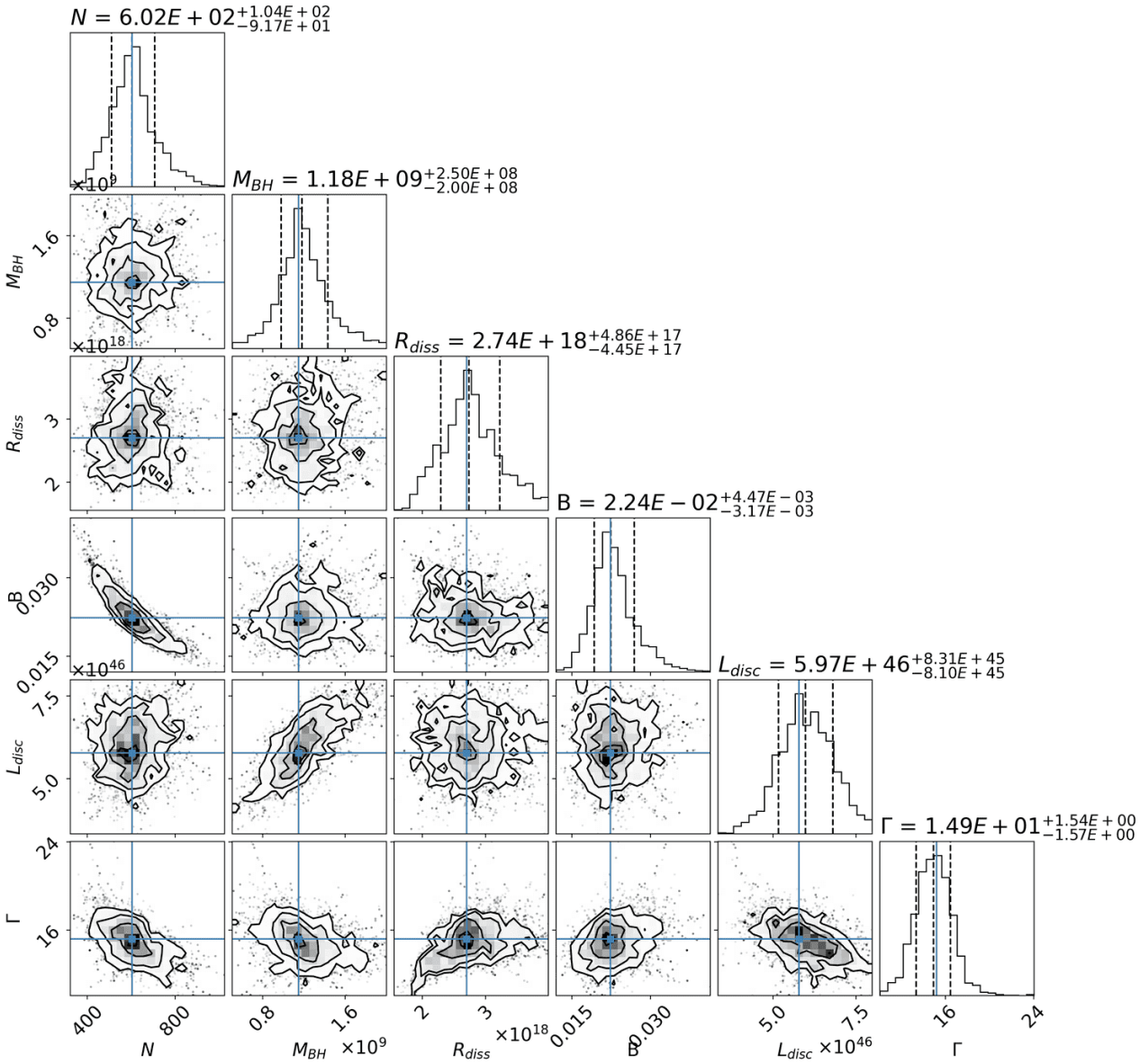

Figure 4.11. Corner plot for model with $\eta = 0.300$.

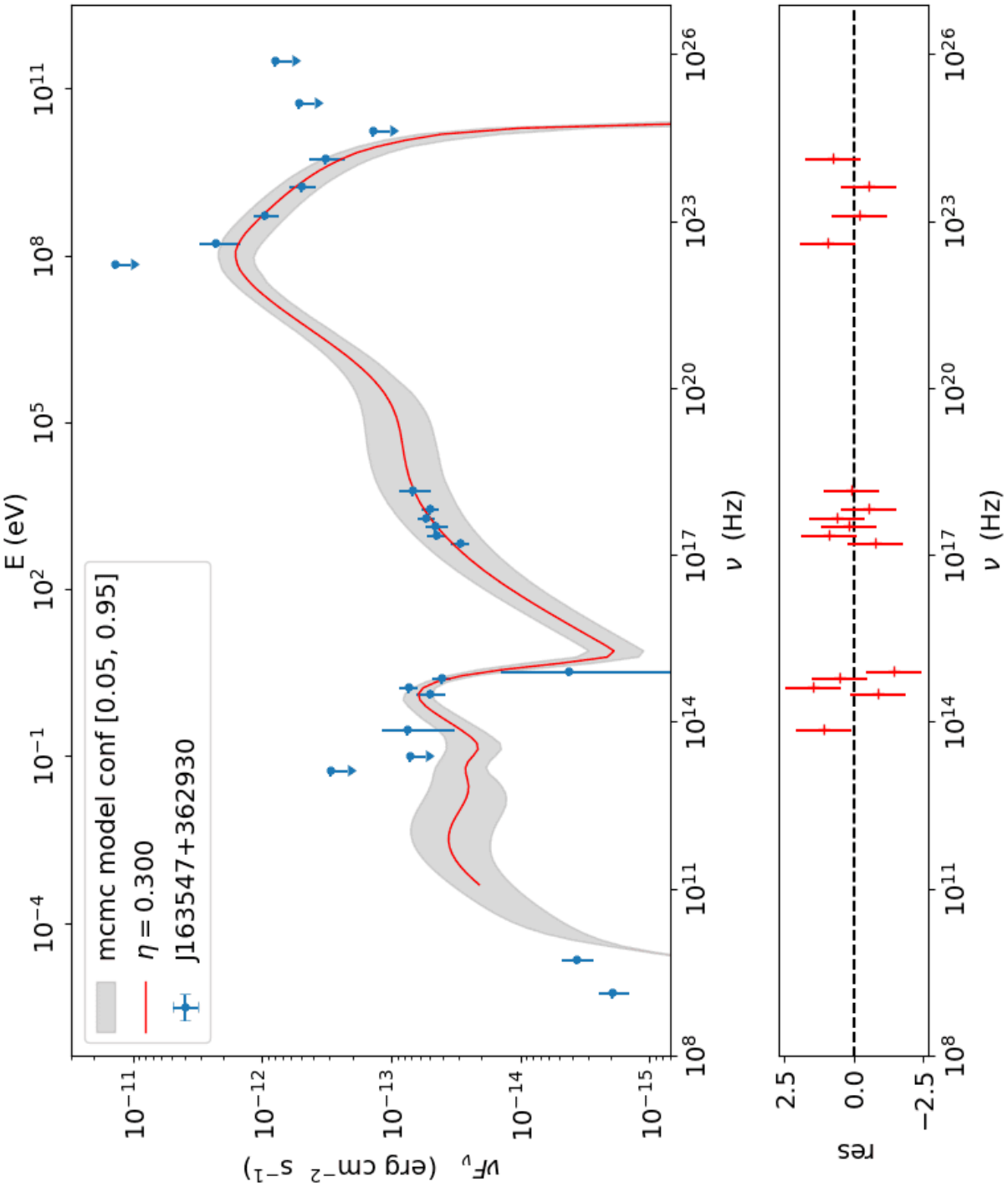

Figure 4.12. MCMC projection for model with $\eta = 0.300$.

4.2 The SMBH Evolution

Using the λCDM cosmological model described in § 3, for any of the different models obtained, the SMBH hosted in our blazar of study, must have formed within $t = 1.722$ billion years after the Big Bang. This prerequisite establishes a notable constraint on the mechanisms governing the origination and enlargement of black hole seeds during the early universe. We have already said that black holes grow by a combination of mergers and gas accretion, and it should be easy to think that the more massive the initial seed, the less time is required for it to grow to our estimated values. Now, with everything we have shown and discussed, it should be possible to set a basic model that describes the mass evolution for our study. This model was first proposed by Shapiro (2005) to study the evolution not only for the mass but also for the spin of the black hole, considering that the seed black holes are expected to possess rotation across all feasible formation scenarios. It is then asked the reader to review the literature for a more comprehensive treatment of the subject on this section.

We have already defined $L_{\rm acc}$ in Equation 2.92, and thus η as the efficiency of conversion of rest-mass energy to luminous energy by accretion. Also, in Equation 2.116, we defined $L_{\rm Edd}$ as the limit for which the radiation pressure is in balance with the gravitational force. We can provide additional details on the preceding equation by taking into account the average molecular weight per electron, denoted as μ_e, which is defined as follows:

$$\mu_e = \frac{1}{1 - Y/2} \approx \frac{8}{7} \tag{4.6}$$

Here, we make the assumption that the accreting plasma consists of zero-metallicity, primordial gas, while considering a helium abundance denoted as Y, with an approximate value of $Y \approx 0.25$ as noted by Cyburt et al. (2003). Now, considering that a black hole growth rate must account for the loss of accretion mass energy in the form of outgoing radiation according to

$$\frac{dM_{BH}}{dt} = \dot{M}_{BH} = (1 - \eta)\dot{M}_{BH,0} \tag{4.7}$$

where $\dot{M}_{BH,0}$ is the rate of rest-mass accretion, we can combine Equations 2.92, 2.116 & 4.7 to obtain the black hole growth rate

$$\dot{M}_{BH} = \frac{L_{\rm acc}}{L_{\rm Edd}} \frac{(1 - \eta)}{\eta} \frac{M_{BH}}{\tau_{\rm acc}} = \eta_{\rm Edd} \frac{(1 - \eta)}{\eta} \frac{M_{BH}}{\tau_{\rm acc}} \tag{4.8}$$

where $\eta_{\rm Edd}$ is the efficiency of accretion luminosity, and $\tau_{\rm acc}$ the characteristic accretion timescale. In particular, the latter is defined as

$$\tau_{\rm acc} \equiv \frac{M_{BH} c^2}{L_{\rm Edd}} \approx 0.45 \mu_e^{-1} \text{ Gyr} \tag{4.9}$$

which is independent of M_{BH}.

It is worth remembering that η is dependent on the spin of the black hole, while simultaneously the spin itself relies on M_{BH}. In other words, for a comprehensive understanding of the evolution of M_{BH}, one must also account for the spin evolution. However, this falls beyond the scope of this thesis, and thus we assume a constant spin, resulting in constant values for η and $\eta_{\rm acc}$. With this consideration in mind, we can now integrate Equation 4.8, yielding:

$$M_{BH}(t) = M_{BH}(t_0) \exp\left[\eta_{\rm Edd} \frac{1-\eta}{\eta} \frac{t-t_0}{\tau_{\rm acc}}\right] \tag{4.10}$$

Here, t_0 represents the initial time at which the black hole possesses a mass of $M_{BH}(t_0)$. It should be evident from this expression that under these assumptions, the evolution of the black hole is primarily governed by efficiencies, which are complex parameters to define.

Using this model, we can now project the potential evolution of the SMBH for the different values of M_{BH} within our models. To select our time frame, we opted to initiate the progression at $t_0 = 99.321$ Myr, corresponding to $z = 30$, and continue until $t = 1.722$ Gyr, which aligns with the redshift of our source considering the same cosmological model used in § 3.4.1. This specific time frame choice is grounded in the emergence of the earliest stars and galaxies at approximately $z \sim 30$, as indicated by previous studies (e.g., Bromm and Larson (2004) and Bromm and Yoshida (2011)). Furthermore, armed with this information, we can derive the value of $M_{BH}(t = t_0)$ under the assumptions we have outlined. In particular, in Figure 4.13 we have included a shaded region to represent conjectured values for the mass of seed black holes, denoted as $M_{\rm seed}$, taking into account only direct collapse models (e.g., M. A. Latif and Ferrara (2016)), where $M_{\rm seed}$ is estimated to be in the range of $10^4 - 10^6 M_\odot$. Figure 4.13 illustrates the projected developmental trajectory of these black holes according to this model using data from Table 4.2.

Line	η	$M_{BH}(10^9 M_\odot)$	$L_{\rm acc}(10^{46}$ erg/s)	$L_{\rm Edd}(10^{47}$ erg/s)	$\eta_{\rm Edd}$
Brown	0.057	1.19	1.99	1.71	12%
Orange	0.083	1.13	2.82	1.63	17%
Green	0.100	1.27	4.02	1.83	22%
Red	0.150	1.43	6.60	2.06	32%
Purple	0.200	1.32	8.44	1.90	44%
Pink	0.300	1.07	11.94	1.54	77%
Dashed	0.150	1.24	17.78	1.78	100%

Table 4.2. Parameters derived from the computed models are employed in conjunction with Equation 4.10 to depict the evolution of the SMBH in NVSS J16547+36293. The last row represents the average outcome for the calculated M_{BH} values, assuming efficiency values of 0.150 for η and 100% for $\eta_{\rm Edd}$. The evolution of the SMBH is represented in Figure 4.13.

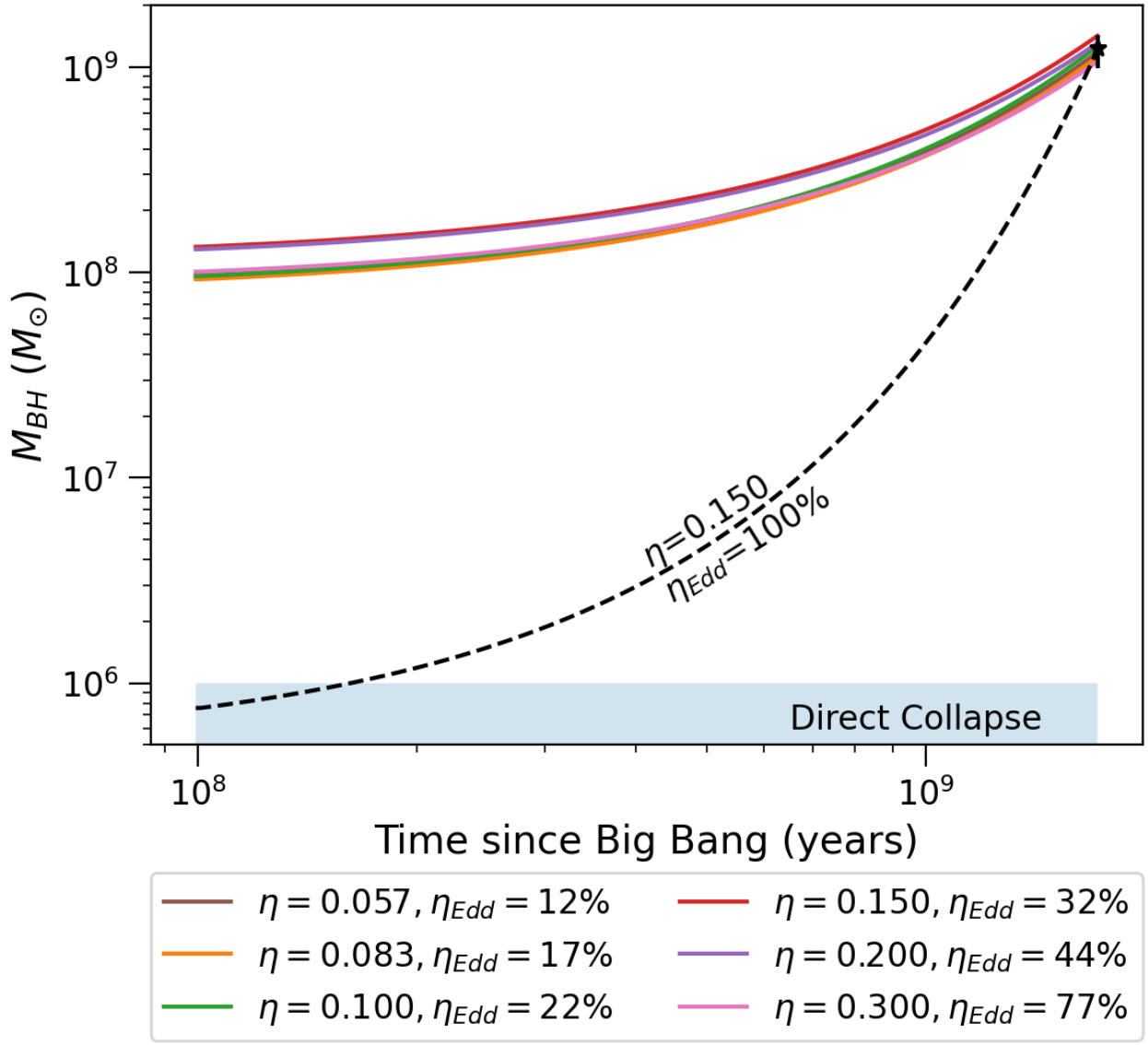

Figure 4.13. M_{BH} evolution for NVSS J16547+36293 since $t_0 = 99.321$ Myr ($z = 30$), to $t = 1.722$ Gyr ($z \approx 3.65$). Each colour line represents the evolution for different values obtained in the SED modelling for both the accretion efficiency η and the accretion luminosity efficiency $\eta_{\rm Edd}$. Meanwhile, the dashed line illustrates the trajectory for the specified values in relation to a black hole with $M_{BH} = 1.24^{+0.24}_{-0.20} \times 10^9 M_\odot$—representing the mean estimate for the obtained values of M_{BH} for the different models with an error based on the 16th, and 84th percentiles of the samples in the marginalised distributions obtained in the MCMC sampling. The shaded horizontal region correspond to the expected mass ranges direct collapse black holes ($M_{\rm seed} \sim 10^4 - 10^6 M_\odot$).

These findings are influenced by the underlying assumptions, encompassing factors such as the redshift of seed formation, η, and $\eta_{\rm Edd}$. It can be seen that the only scenario in which a SMBH with $M_{BH} \approx 10^9 M_\odot$ is consistent with those predicted by current theoretical models for $M_{\rm seed}$ is the case in which we consider a high value for $\eta_{\rm Edd}$, and, most importantly, a smaller value for the accretion efficiency than for a highly spinning black hole. These results support the scenario by which the SMBH in NVSS J163547+362930 evolves over cosmological time from a heavy seed rather than through highly efficient accretion.

At the moment of writing this thesis, recent advances in the comprehension of the formation and evolution of SMBHs during the early universe have emerged, thanks to contributions made by the *Chandra* X-ray observatory and the JWST. The recent identification of a quasar within the galaxy UHZ1 at a redshift of $z \approx 10$, facilitated by Chandra-JWST observations, discloses that the accreting SMBH hosted in UHZ1 had already established itself approximately 450 million years after the Big Bang (e.g., Bogdan et al. (2023)). Its estimated mass is around $4 \times 10^7 M_\odot$, assuming an Eddington ratio ($\eta_{\rm Edd}$) of 100%. These attributes closely align with preceding theoretical forecasts for a distinctive category of ephemeral, high-redshift entities known as Outsize Black Hole Galaxies (OBGs; e.g., Natarajan et al. (2017)), which house an initially substantial black hole seed formed likely through direct gas collapse rather than stemming from Population III stars. However, these recent theories can be integrated with the search of high-redshift blazars to achieve a more comprehensive understanding and visualisation of the evolution and formation of SMBHs. For further information on this particular study, please consult the work of Natarajan et al. (2023).

4.3 Jet Power and Accretion Relation

We have already discussed, as well as proof in previous analysis, that there exists an intrinsic relation between the jet power, the spin, and mass of the central black hole due to accreting material. In particular, the process driving the magnetic field within the jet is the rotational black hole resulting from the infalling material, which applies torque on it. Although evidence of this correlation exists through the examination of a variety of blazars at varying redshifts (e.g., Ghisellini, Tavecchio, et al. (2010), Ghisellini et al. (2014), Maraschi and Tavecchio (2003), and Rawlings and Saunders (1991)), our intention in this section is to observe this relationship considering the distinct assumptions about the black hole's spin.

In 2.7.2, we outlined the constituents that compose the total emitted jet power, denoted as $P_{\rm jet}$. These constituents include radiative emissions $P_{\rm rad}$, the power carried by electrons P_e and cold protons P_p, as well as the power carried by the magnetic field P_B. In particular, $P_{\rm rad}$, which can establish a lower limit for $P_{\rm jet}$ and is directly proportional to $L_{\rm disc}$, is estimated to

account for approximately 10% of $P_{\rm tot}$ (Ghisellini et al., 2009). Interestingly, this proportion has been observed to hold consistently, even in the case of Gamma-Ray Bursts (e.g., Nemmen et al. (2012)). This proportionality implies that $P_{\rm jet}$ must be larger than $L_{\rm acc}$, consequently, the process responsible for initiating and accelerating jets must exhibit remarkable efficiency, representing the most effective means of transferring energy from the vicinity of the black hole into the jets (Ghisellini et al., 2014).

Using the energetic report, which was computed by `JetSeT`, and despite the fact that a single source was used throughout the work, it was possible to verify such correlation between $P_{\rm jet}$ and $L_{\rm acc}$ for different accretion efficiencies supporting the conservation of energy. In our specific scenario, using the values shown in Table 4.3, the average ratio between the powers is approximately $P_{\rm rad}/P_{\rm jet} \sim 1\%$. In Figure 4.14 it can then be seen that, especially for lower values of η, $P_{\rm jet}$ is larger than $L_{\rm acc}$. This implies that the gravitational potential energy of the infalling material not only undergoes conversion into heat and radiation but also serves to amplify the magnetic field. This magnetic field amplification enables access to the substantial reservoir of rotational energy inherent to the black hole, leading to the conversion of a portion of it into mechanical power for the jet. On the other hand, we see that higher values of η produce $P_{jet} \sim L$acc, which means that energy conversion is rather inefficient, even though $P_{jet} \sim 10 P_{rad}$. Thus, considering the nature of the jet power, this test could work to accept or reject possible models that account for the SED modelling. In particular, for our case, we again find that high values of η are likely not realistic, supporting the view that the SMBH in NVSS J163547+362930 must be originated in the heavy seeds scenario.

η	0.057	0.083	0.100	0.150	0.200	0.300
$P_B(10^{43}$ erg s$^{-1})$	3.74	3.61	1.34	0.37	0.35	0.86
$P_e(10^{45}$ erg s$^{-1})$	7.37	7.85	7.71	9.49	10.60	11.89
$P_{p_{\rm cold}}(10^{46}$ erg s$^{-1})$	2.57	2.92	2.38	2.67	2.99	3.95
$P_{\rm rad}(10^{44}$ erg s$^{-1})$	9.53	8.08	5.98	5.08	4.9	5.24
$P_{\rm kin}(10^{46}$ erg s$^{-1})$	3.30	3.70	3.15	3.62	4.05	5.13
$P_{\rm jet}(10^{46}$ erg s$^{-1})$	3.40	3.79	3.21	3.68	4.10	5.19

Table 4.3. Luminosity components carried by the jet for the radiative components, the electrons, the magnetic fields, and for the cold protons in the jet for our different models. For calculating $P_{p_{\rm cold}}$, we are considering a ratio of cold protons to relativistic electrons of 0.10.

Furthermore, it is also important to mention that these quantities are not not intrinsically related to each other, even if the main radiation mechanism is the inverse Compton process from an external photons, which in turn we have showed in this work are proportional $L_{\rm disc}$, which is also proportional to $L_{\rm acc}$. This situation arises because of the

complete radiative cooling of the emitting electrons, resulting in the jet's generated luminosity becoming independent of the radiation energy density. In other words, within the fast-cooling scenario, the jet consistently releases all the energy carried by its relativistic electrons and cold protons, regardless of the accretion disc's luminosity (Ghisellini et al., 2011).

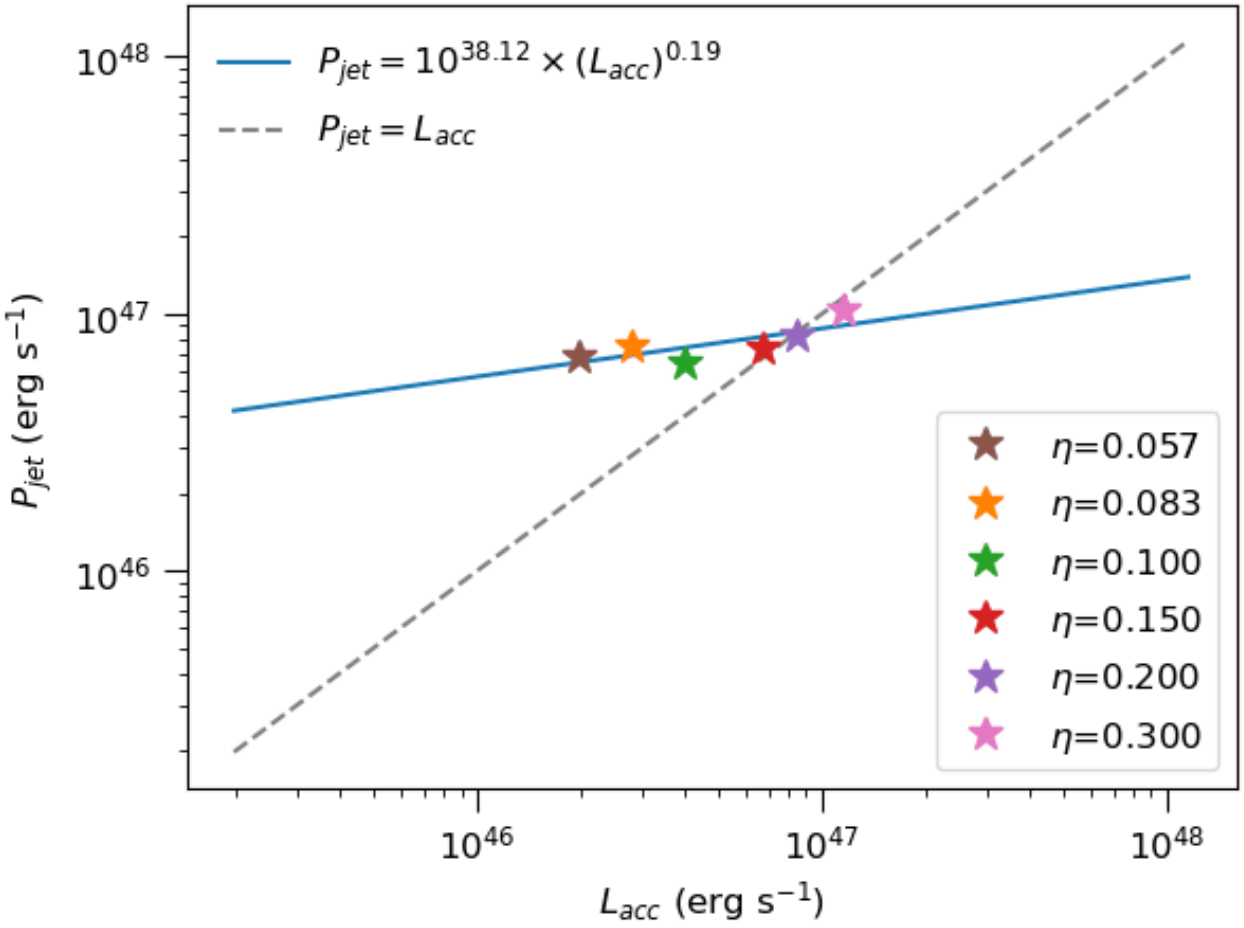

Figure 4.14. $P_{\rm jet}$ estimated through the `JetSeT` framework, assuming a ratio of cold protons to relativistic electrons of 0.10, against $L_{\rm acc}$ (see Table 4.2), using different models for η. The blue line is the best least square fit, while the yellow stripe is the equality line. The components for $P_{\rm jet}$ can be seen in Table 4.3.

4.4 Lyman-Limit: Redshift Estimation

To perform a consistency check in our SED modelling, we compare the redshift of the source measured by Pâris et al. (2018) ($z \approx 6.35$) and the redshifts that we can infer from the SED through a dropout technique, which relies on multiwavelength broadband photometric observations. This technique is grounded in the concept that neutral hydrogen in the path of light between the source and the observer, scattered across the hot intergalactic medium

(IGM; e.g., Gunn and Peterson (1965)), effectively absorbs photons with a rest-wavelength shorter than 912 and 1216 Å, which represent the Lyman-limit and the Lyman-α forest lines (see § 1.1.3). This implies that the energy emitted by high-redshift sources at wavelengths shorter than the Lyman-limit emission line gets significantly absorbed by the clouds along the line of sight. In particular, objects such as blazars will not be detected, or will "drop-out", when viewed through filters with spectral responses that extend prior to the red-shifted Lyman-limit at $(1+z)\times 912$ Å; in the case of the wavelength coverage for UVOT, this happens at $z \sim 0.8$. The relative strength of the two breaks in the spectrum depends on the redshift of the source, which means that this technique can also be used to measure the photometric redshift, denoted $z_{\rm phot}$, providing, in an independent approach, a reliable lower limit on the blazar redshift. The method has been extensively applied to estimate the redshift of *Fermi*-LAT blazars that do not display line features for which it would be difficult or even impossible to find the redshift (e.g., Rau et al. (2012)).

For our case of study, we knew in advance that it was possible to detect this absorption due to the data obtained from UVOT and *GAIA*. In fact, it is very clear from Figure 3.6 and absorption in the UV range for all the computed models. Thus, by using these different SED models obtained in § 3, it should be possible to estimate $z_{\rm phot}$. For this, we plot the luminosity obtained for each of our models against λ as shown in Figure 4.15 (upper panel). As we are performing a broadband modelling, we will not see any dominant emission lines, meaning it is possible to use a simple power-law to model the UV to optical emissions. Nevertheless, considering our discussion in § 1.1.3, and the beginning of this section, we will see a cut in the model at the Lyman-limit. Hence, in our case, it is a good approximation to use the break wavelength at this range to estimate the Lyman-limit, and with it obtain the lower limit for $z_{\rm phot}$. In particular, for the inflection point, we took the second derivative of the SED and solved for zero. The results of this analysis are reported in Table 4.4. Thus, taking the mean value of all the solutions found, we can report a lower limit for the redshift of the source of $z = 1.95^{0.06}_{0.06}$. In Figure 4.15, the upper plot shows the source's measured luminosity for the different models, while the lower plot shows both the DT and disc emissions. In both these graphs, vertical bands are displayed representing the rest-frame, observed, and lower limit for the Lyman-limit line.

In this analysis, we can verify and explain the relatively large error bar associated with the UVOT data point at 358.60 nm (equivalent to 8.36×10^{14} Hz). The presence of this point in close proximity to both the observed and the lower limit Lyman lines contributes to a significant uncertainty in the energy density. This finding serves to confirm our initial hypothesis regarding the source of this error. Furthermore, the lower redshift limit inferred through the SED is consistent with the actual measured redshift, thereby supporting the modelling of the source.

η	Break point (nm)	$z_{\rm phot}$
0.057	268.37	1.94
0.083	274.37	2.01
0.100	269.26	1.95
0.150	266.15	1.92
0.200	271.35	1.98
0.300	263.08	1.88
Mean	$268.66^{+5.58}_{-5.70}$	$1.95^{+0.06}_{-0.06}$

Table 4.4. Inflection point and z_{phot} for each model. As explained in § 4.4, it is possible to use this inflection point to set a lower limit for the redshift of the source. In particular, for our case, we can set a lower limit for the redshift of $z = 1.95^{+0.06}_{-0.06}$.

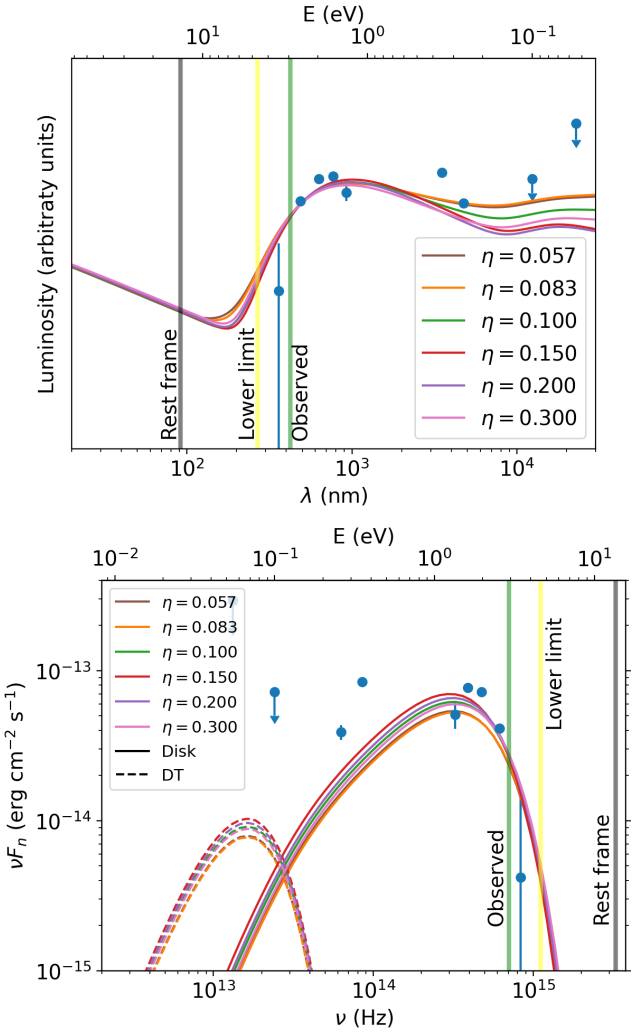

Figure 4.15. Photometric redshift estimation accounting for the different SED modelling. Left: energy density for both the DT and the disc against frequency; right: total source's emitted luminosity against wavelength. For both plots the black and yellow vertical lines represent the rest-frame and observed values for the Lyman-limit respectively.

4.5 Next Steps

For our work related to the SED modelling of our chosen blazar, we relied exclusively on a leptonic model. This choice has proven to be the most favourable, as it requires, for instance, smaller magnetic field strengths than when using a lepto-hadronic model. However, more information has emerged regarding the correlation between neutrino emissions and AGN, particularly blazars, in recent years (e.g., Buson et al. (2022)). This suggests that lepto-hadronic modelling should also be considered whenever employing a leptonic model alone, as neutrinos can only be generated through lepto-hadronic processes. In particular, we should note that this new approach could be carried out using the `JetSeT` framework, making it even more useful due to its other attributions.

A relevant mission in high energy astronomy is the Nuclear Spectroscopic Telescope Array Mission (*NuSTAR*; Harrison et al. (2013)). This mission operates in the X-ray spectrum and boasts the pioneering use of focussing optics for hard X-rays, specifically those above 10 keV. Launched on June 13, 2012, and positioned in a low-inclination low-Earth orbit, it was initially programmed for a two-year mission, but it continues to gather data. Covering an energy range of 3-79 keV and featuring a telescope with the capability to extend to a 10-meter focal length, it offers a combination of sensitivity, spatial, and spectral resolution factors that are 10 to 100 times improved compared to previous X-ray missions, particularly *XMM*-Newton. From June 1, 2023, to May 31, 2024, *NuSTAR* will embark on its ninth cycle. In this cycle, our designated source, NVSS J163547+362930, has been accepted and a guaranteed an observation time totalling 30 ks. Despite the relatively limited observation time, which may result in a somewhat modest signal-to-noise ratio, implying possible relatively large error margins for the observed emissions, these observations will hold considerable value, as they will contribute to a more precise constraint of the SED models within the X-ray energy band, complementing the *XMM* observations. In addition, the data could also be used to study possible X-ray variability, as well as to constrain the SMBH and its nuclear environment (e.g., Bottacini (2022)).

Another important analysis that can be done regarding the SED for our source is to study, although we said that it is not a highly variable source, the multi-epoch SED. This investigation serves as a potent means to comprehensively explain the observation of high-end TeV spectra flares, irrespective of the methodology employed. This observational evidence has persisted for some time, but current studies (e.g., Tramacere et al. (2022)) have suggested that the $\gamma-$ray emission might originate upstream within the jet, due to an adiabatic expansion of the emitting blob, resulting in the region becoming radio-transparent at larger scales. In our specific scenario, an in-depth analysis and modelling of the blob's expansion within the jet could potentially account for the upper limits measured by *Fermi* for our source. In

particular, it could enable us to make predictions about the SED whenever the UHE data become accessible for our source.

It was explained in § 1 that the SED can be affected by $\gamma - \gamma$ interactions with the so-called EBL. In fact, it was also mentioned that to properly constrain the emission processes contributing to the high-energy portion of the spectrum, it is crucial to consider EBL corrections when performing SED modelling. Therefore, the next step to take in the multiwavelength study of NVSS J163547+362930 is to use different EBL models (e.g., Dominguez et al. (2011), Finke et al. (2010), and Franceschini et al. (2008)), which will improve our understanding not only of the emission processes within our source but also of the EBL field and its interaction with other particles. The latter, as is the case with cosmic rays, UHE protons, or nuclei heavier than protons, interacting with the EBL and the CMB, may disintegrate into lighter nuclei, resulting in the so-called Greisen-Zatsepin-Kuzmin (GZK) cut-off (Greisen, 1966).

As a final comment, this study has highlighted a significant degree of uncertainty in the hard X-ray portion of the SED. Consequently, there is a pressing need for forthcoming missions equipped with adequate effective area telescope, especially for high-redshift sources, to investigate this specific wavelength range. Currently, there are no missions capable of conducting such observations, emphasising the potential utility of our results as templates for future missions seeking to detect sources similar to NVSS J163547+362930. This effort promises to provide us with the opportunity to refine our constraints and explanations regarding the evolution and formation of SMBHs in the early universe. Additionally, it opens up the possibility of better relating the dependencies between SMBHs and their nuclear environments.

4.6 Conclusions

At redshift $z = 3.65$, NVSS J163547+362930 stands out for its multifrequency coverage. This presents a unique opportunity to dive into and gain deeper insights into the underlying physical mechanisms governing SMBHs and their surrounding nuclear environment in the early universe. To embark on this endeavour, we undertook the following steps:

- We embarked on a comprehensive theoretical exploration of AGN, with a specific focus on blazars. Our journey through the realm of blazars encompassed an in-depth study of the primary radiative processes supporting their emissions. We delved into the details of the leptonic and lepto-hadronic scenarios, showing their key distinctions. Mainly, a key aspect of our investigation was centred around the role of broadband SED modelling, in particular for high-redshift sources. We highlighted its significance in constraining

critical parameters linked to the blazar's central engine and emission zone, shedding light on the complexities of these high-energy phenomena.

- Our research journey then transitioned into the realm of empirical data analysis, where we gathered data from various low- and high-energy missions, as well as radio catalogues. Through meticulous SED modelling, using the `JetSeT` framework, we probed the effects of varying the black hole spin, ranging from non-rotating Schwarzschild black holes to the extreme Kerr variety. With our models in hand, we employed MCMC sampling techniques to refine our understanding of the key parameters governing blazar emissions, having as a result better constrained values.

- A first insight obtained from our standard SSD model was the excellent fit for the γ-ray emissions found to be produced from EC processes, with the DT being the source of the external photons instead of originating in the BLR. At the same time, we find that the peak for the EC processes of the disc is located near the MeV band. With further explorations from different High Energy Astrophysics missions, this could explain potential contributions at this energy in the SED, allowing us to better constrain the accretion disc and, consequently, the SMBH.

- With the results obtained from our modelling, it was possible to trace the formation and evolution of the SMBH within NVSS J163547+362930 by using a simplistic model considering mainly the accretion efficiency and the accretion luminosity. Notably, our findings illuminated a cosmological evolution in which the SMBH evolved from a heavy seed, rather than through highly efficient accretion mechanisms, favouring moderate spin values of the SMBH. Additionally, we verify the intrinsic correlation between the jet power and the accretion luminosity, offering insights into the plausibility of high accretion efficiency values for high-luminosity accretion discs. Our results support the scenario in which the SMBH in NVSS J163547+362930 evolution with high values for the accretion efficiency, and in agreement with our previous findings, are likely not realistic. It was also discussed and explained, due to the nature and relation between the central engine's main components, that the relation between the jet power and the accretion luminosity can be used as a valuable tool to differentiate between physical and un-physical accretion efficiency values.

- Finally, in this thesis, we introduced a simple but accurate technique for determining a lower limit of the source's redshift by measuring the inflection point in the Optical-UV range. This approach proved particularly valuable for high-redshift AGN, as it allowed us to glean insights into the Lyman-limit drop within this range, thereby providing a measure of the line's wavelength even though using only a broadband spectrum.

Bibliography

Abbott, B. P., et al. (2016). Observation of Gravitational Waves from a Binary Black Hole Merger. *Phys. Rev. Lett.*, *116*, 061102.

Abdo, A., Ackermann, M., Agudo, I., Ajello, M., Aller, H., Aller, M., Angelakis, E., Arkharov, A., Axelsson, M., Bach, U., et al. (2010). The spectral energy distribution of Fermi bright blazars. *ApJ*, *716*, 30.

Abdollahi, S., Acero, F., Baldini, L., Ballet, J., Bastieri, D., Bellazzini, R., Berenji, B., Berretta, A., Bissaldi, E., Blandford, R. D., et al. (2022). Incremental fermi large area telescope fourth source catalog. *ApJ Supplement Series*, *260*, 53.

Acciari, V. A., et al. (2009). Multiwavelength Observations of a TeV-Flare from W Comae. *ApJ*, *707*, 612–620.

Ackermann, M., et al. (2017). Gamma-ray blazars within the first 2 billion years. *Astrophys. J. Lett.*, *837*, L5.

Ackermann, M., Anantua, R., Asano, K., Baldini, L., Barbiellini, G., Bastieri, D., Gonzalez, J. B., Bellazzini, R., Bissaldi, E., Blandford, R., et al. (2016). Minute-timescale¿ 100 MeV γ-ray variability during the giant outburst of quasar 3C 279 observed by Fermi-LAT in 2015 June. *ApJ Letters*, *824*, L20.

Aharonian, F., Akhperjanian, A., Bazer-Bachi, A., Behera, B., Beilicke, M., Benbow, W., Berge, D., Bernlöhr, K., Boisson, C., Bolz, O., et al. (2007). An exceptional very high energy Gamma-Ray flare of PKS 2155–304. *ApJ*, *664*, L71.

Alam, S., Albareti, F. D., Prieto, C. A., Anders, F., Anderson, S. F., Anderton, T., Andrews, B. H., Armengaud, E., Aubourg, É., Bailey, S., et al. (2015). The eleventh and twelfth data releases of the Sloan Digital Sky Survey: final data from SDSS-III. *ApJS*, *219*, 12.

Alexander, T., & Natarajan, P. (2014). Rapid growth of seed black holes in the early universe by supra-exponential accretion. *Science*, *345*, 1330–1333.

Alvarez, M. A., Wise, J. H., & Abel, T. (2009). Accretion onto the first stellar-mass black holes. *ApJ*, *701*, L133.

Antonucci, R. (1993). Unified models for active galactic nuclei and quasars. *Annu. Rev. Astron. Astr.*, *31*, 473–521.

Antonucci, R., & Miller, J. (1985). Spectropolarimetry and the nature of NGC 1068. *ApJ*, *297*, 621–632.

Asano, K., & Hayashida, M. (2018). Blazar spectra with hard-sphere-like acceleration of electrons. *ApJ*, *861*, 31.

Atwood, W., Abdo, A. A., Ackermann, M., Althouse, W., Anderson, B., Axelsson, M., Baldini, L., Ballet, J., Band, D., Barbiellini, G., et al. (2009). The large area telescope on the fermi gamma-ray space telescope mission. *ApJ*, *697*, 1071.

Becker, R. H., White, R. L., & Edwards, A. L. (1991). A new catalog of 53,522 4.85 GHz sources. *ApJ Supplement Series*, *75*, 1–229.

Becker, R. H., White, R. L., & Helfand, D. J. (1995). The FIRST survey: faint images of the radio sky at twenty centimeters. *ApJ*, *450*, 559.

Beckmann, V., & Shrader, C. (2012). *Active galactic nuclei*. John Wiley & Sons.

Begelman, M. C., Volonteri, M., & Rees, M. J. (2006). Formation of supermassive black holes by direct collapse in pre-galactic haloes. *MNRAS*, *370*, 289–298.

Belladitta, S., Caccianiga, A., Diana, A., Moretti, A., Severgnini, P., Pedani, M., Cassarà, L. P., Spingola, C., Ighina, L., Rossi, A., et al. (2022). Central engine of the highest redshift blazar. *A&A*, *660*, A74.

Berk, D. E. V., Richards, G. T., Bauer, A., Strauss, M. A., Schneider, D. P., Heckman, T. M., York, D. G., Hall, P. B., Fan, X., Knapp, G., et al. (2001). Composite quasar spectra from the sloan digital sky survey. *ApJ*, *122*, 549.

Berti, E. (2006). LISA observations of massive black hole mergers: event rates and issues in waveform modelling. *CQG*, *23*, S785.

Biteau, J. (2013). *A window on stochastic processes and gamma-ray cosmology through spectral and temporal studies of agn observed with hess* (Doctoral dissertation). Ecole Polytechnique X.

Blandford, R. D., & Payne, D. G. (1982). Hydromagnetic flows from accretion disks and the production of radio jets. *MNRAS*, *199*, 883–903.

Blandford, R. D., & Znajek, R. L. (1977). Electromagnetic extraction of energy from Kerr black holes. *MNRAS*, *179*, 433–456.

Błażejowski, M., Sikora, M., Moderski, R., & Madejski, G. (2000). Comptonization of infrared radiation from hot dust by relativistic jets in quasars. *ApJ*, *545*, 107.

Bloom, S. D., & Marscher, A. P. (1996). An analysis of the synchrotron self-compton model for the multi–wave band spectra of blazars. *ApJ*, *461*, 657.

Blumenthal, G. R., & Gould, R. J. (1970). Bremsstrahlung, synchrotron radiation, and compton scattering of high-energy electrons traversing dilute gases. *Reviews of modern Physics*, *42*, 237.

Boekholt, T. C., Schleicher, D., Fellhauer, M., Klessen, R., Reinoso, B., Stutz, A., & Haemmerlé, L. (2018). Formation of massive seed black holes via collisions and accretion. *MNRAS*, *476*, 366–380.

Boettcher, M. (2011). *Modeling the spectral energy distributions and variability of blazars* [Fermi & Jansky: Our Evolving Understanding of AGN].

Bogdan, A., Goulding, A., Natarajan, P., Kovacs, O., Tremblay, G., Chadayammuri, U., Volonteri, M., Kraft, R., Forman, W., Jones, C., et al. (2023). Detection of an X-ray quasar in a gravitationally-lensed $z = 10.3$ galaxy suggests that early supermassive black holes originate from heavy seeds. *arXiv:2305.15458*.

Bonnoli, G., Ghisellini, G., Foschini, L., Tavecchio, F., & Ghirlanda, G. (2011). The γ-ray brightest days of the blazar 3C 454.3. *MNRAS*, *410*, 368–380.

Bottacini, E. (2022). Hard X-Ray broadband spectroscopy of Mrk 876: characterizing its spectrum. *MNRAS*, *515*, 3174–3183.

Bottacini, E., Böttcher, M., Pian, E., & Collmar, W. (2016). 3C 279 in Outburst in 2015 June: a broadband SED study based on the INTEGRAL detection. *ApJ*, *832*, 17.

Bottacini, E., Ajello, M., Greiner, J., Pian, E., Rau, A., Palazzi, E., Covino, S., Ghisellini, G., Krühler, T., Küpcü Yoldas, A., Cappelluti, N., & Afonso, P. (2010). PKS 0537-286, carrying the information of the environment of SMBHs in the early Universe. *A&A*, *509*, A69.

Böttcher, M. (2007). Astrophysical jets of blazars and microquasars. *APSS*, *307*, 69–75.

Bowyer, C. S., Lampton, M., Mack, J., & de Mendonca, F. (1970). Detection of X-Ray Emission from 3C 273 and NGC 5128. *ApJ*, *161*, L1.

Bromm, V., & Larson, R. B. (2004). The first stars. *Annu. Rev. Astron. Astr.*, *42*, 79–118.

Bromm, V., & Yoshida, N. (2011). The first galaxies. *Annu. Rev. Astron. Astr.*, *49*, 373–407.

Brown, A., Vallenari, A., Prusti, T., De Bruijne, J., Babusiaux, C., Bailer-Jones, C., Biermann, M., Evans, D. W., Eyer, L., Jansen, F., et al. (2018). Gaia data release 2-summary of the contents and survey properties. *A&A*, *616*.

Burbidge, G. R. (1959). Estimates of the Total Energy in Particles and Magnetic Field in the Non-Thermal Radio Sources. *ApJ*, *129*, 849–852.

Buson, S., Tramacere, A., Pfeiffer, L., Oswald, L., de Menezes, R., Azzollini, A., & Ajello, M. (2022). Beginning a journey across the universe: The discovery of extragalactic neutrino factories. *ApJ Letters*, *933*, L43.

Cardelli, J. A., Clayton, G. C., & Mathis, J. S. (1989). The relationship between infrared, optical, and ultraviolet extinction. *ApJ*, *345*, 245–256.

Cerruti, M., et al. (2022). The blazar hadronic code comparison project [IUPAP]. *37th International Cosmic Ray Conference*, 979.

Cerruti, M., Zech, A., Boisson, C., & Inoue, S. (2015). A hadronic origin for ultra-high-frequency-peaked BL Lac objects. *MNRAS*, *448*, 910–927.

Cleary, K., Lawrence, C., Marshall, J., Hao, L., & Meier, D. (2007). Spitzer observations of 3C quasars and radio galaxies: mid-infrared properties of powerful radio sources. *ApJ*, *660*, 117.

Condon, J. J., Cotton, W., Greisen, E., Yin, Q., Perley, R. A., Taylor, G., & Broderick, J. (1998). The NRAO VLA sky survey. *ApJ*, *115*, 1693.

Costamante, L., Cutini, S., Tosti, G., Antolini, E., & Tramacere, A. (2018). On the origin of gamma-rays in fermi blazars: Beyondthe broad-line region. *MNRAS*, *477*, 4749–4767.

Cyburt, R. H., Fields, B. D., & Olive, K. A. (2003). Primordial nucleosynthesis in light of WMAP. *Phys. Lett. B*, *567*, 227–234.

De Angelis, A., & Pimenta, M. (2018). *Introduction to particle and astroparticle physics: Multimessenger astronomy and its particle physics foundations*. Springer.

Dermer, C. D., Schlickeiser, R., & Mastichiadis, A. (1992). High-energy gamma radiation from extragalactic radio sources. *A&A*, *256*, L27–L30.

Dermer, C. D., Finke, J. D., Krug, H., & Böttcher, M. (2009). Gamma-ray studies of blazars: Synchro-compton analysis of flat spectrum radio quasars. *ApJ*, *692*, 32.

Dermer, C. D., & Menon, G. (2009). *High energy radiation from black holes: Gamma rays, cosmic rays, and neutrinos* (Vol. 17). Princeton University Press.

Dermer, C. D., & Schlickeiser, R. (1993). Model for the high-energy emission from blazars. *Astrophysical Journal v. 416, p. 458*, *416*, 458.

Dermer, C. D., Sturner, S. J., & Schlickeiser, R. (1997). Nonthermal compton and synchrotron processes in the jets of active galactic nuclei. *ApJS*, *109*, 103.

Devecchi, B., & Volonteri, M. (2009). Formation of the first nuclear clusters and massive black holes at high redshift. *ApJ*, *694*, 302.

Dominguez, A., Primack, J. R., Rosario, D., Prada, F., Gilmore, R., Faber, S., Koo, D., Somerville, R., Pérez-Torres, M., Pérez-González, P., et al. (2011). Extragalactic background light inferred from AEGIS galaxy-SED-type fractions. *MNRAS*, *410*, 2556–2578.

Finke, J. D., Razzaque, S., & Dermer, C. D. (2010). Modeling the extragalactic background light from stars and dust. *ApJ*, *712*, 238.

Foreman-Mackey, D., Hogg, D. W., Lang, D., & Goodman, J. (2013). emcee: the MCMC hammer. *PASP*, *125*, 306.

Fossati, G., Maraschi, L., Celotti, A., Comastri, A., & Ghisellini, G. (1998). A unifying view of the spectral energy distributions of blazars. *MNRAS*, *299*, 433–448.

Franceschini, A., Rodighiero, G., & Vaccari, M. (2008). Extragalactic optical-infrared background radiation, its time evolution and the cosmic photon-photon opacity. *A&A*, *487*, 837–852.

Frank, J., King, A., & Raine, D. (2002). *Accretion power in astrophysics*. Cambridge university press.

Friedman, H., & Byram, E. (1967). X-rays from Sources 3C 273 and M87. *Science*, *158*, 257–259.

Gandhi, P. (2005). X-ray studies of active galactic nuclei. *Asian J. Ph.*, *13*, 90–107.

Georganopoulos, M., Kirk, J., & Mastichiadis, A. (2001). The Beaming Pattern and Spectrum of Radiation from Inverse Compton Scattering in Blazars. *ApJ*, *561*, 111. Corrected in Corrigenda. (2004). *ApJ*, *604*, 479.

Georganopoulos, M., & Kazanas, D. (2003). Decelerating flows in TeV blazars: a resolution to the BL Lacertae-FR I unification problem. *ApJ*, *594*, L27.

Ghisellini, G. (2013a). High redshift blazars. *Memorie della Societa Astronomica Italiana*, *84*, 719.

Ghisellini, G., Ceca, R. D., Volonteri, M., Ghirlanda, G., Tavecchio, F., Foschini, L., Tagliaferri, G., Haardt, F., Pareschi, G., & Grindlay, J. (2010). Chasing the heaviest black holes of jetted active galactic nuclei. *MNRAS*, *405*, 387–400.

Ghisellini, G., Tagliaferri, G., Foschini, L., Ghirlanda, G., Tavecchio, F., Ceca, R. D., Haardt, F., Volonteri, M., & Gehrels, N. (2011). High-redshift fermi blazars. *MNRAS*, *411*, 901–914.

Ghisellini, G., & Tavecchio, F. (2009). Canonical high-power blazars. *MNRAS*, *397*, 985–1002.

Ghisellini, G., Tavecchio, F., Foschini, L., Ghirlanda, G., Maraschi, L., & Celotti, A. (2010). General physical properties of bright fermi blazars. *MNRAS*, *402*, 497–518.

Ghisellini, G., Tavecchio, F., & Ghirlanda, G. (2009). Jet and accretion power in the most powerful fermi blazars. *MNRAS*, *399*, 2041–2054.

Ghisellini, G. (2013b). *Radiative processes in high energy astrophysics* (Vol. 873). Springer.

Ghisellini, G., & Madau, P. (1996). On the origin of the γ-ray emission in blazars. *MNRAS*, *280*, 67–76.

Ghisellini, G., Righi, C., Costamante, L., & Tavecchio, F. (2017). The fermi blazar sequence. *MNRAS*, *469*, 255–266.

Ghisellini, G., Tagliaferri, G., Sbarrato, T., & Gehrels, N. (2015). SDSS J013127. 34–032100.1: A candidate blazar with an 11 billion solar mass black hole at $z = 5.18$. *MNRAS Letters*, *450*, L34–L38.

Ghisellini, G., Tavecchio, F., Maraschi, L., Celotti, A., & Sbarrato, T. (2014). The power of relativistic jets is larger than the luminosity of their accretion disks. *Nature*, *515*, 376–378.

Gilmore, R. C., Somerville, R. S., Primack, J. R., & Dominguez, A. (2012). Semi-analytic modelling of the extragalactic background light and consequences for extragalactic gamma-ray spectra. *MNRAS*, *422*, 3189–3207.

Ginzburg, V. L., & Syrovatskii, S. I. (1965). Cosmic Magnetobremsstrahlung (synchrotron Radiation). *ARAA*, *3*, 297–345.

Giommi, P., Padovani, P., Polenta, G., Turriziani, S., D'Elia, V., & Piranomonte, S. (2012). A simplified view of blazars: Clearing the fog around long-standing selection effects. *MNRAS*, *420*, 2899–2911.

Gould, R. J., & Schréder, G. P. (1967). Pair production in photon-photon collisions. *Phys. Rev.*, *155*, 1404.

Greenstein, J. L. (1963). Red-shift of the unusual radio source: 3C 48. *Nature*, *197*, 1041–1042.

Gregory, P., & Condon, J. (1991). The 87GB catalog of radio sources covering $0^\circ < \delta < +75^\circ$ at 4.85 GHz. *ApJ Supplement Series*, *75*, 1011.

Gregory, P. (2005). *Bayesian logical data analysis for the physical sciences: A comparative approach with mathematica® support*. Cambridge University Press.

Greisen, K. (1966). End to the cosmic-ray spectrum? *PRL*, *16*, 748.

Griffith, M., Langston, G., Heflin, M., Conner, S., Lehar, J., & Burke, B. (1990). The third MIT-Green Bank 5 GHz survey. *ApJS*, *74*, 129–180.

Gunn, J. E., & Peterson, B. A. (1965). On the density of neutral hydrogen in intergalactic space. *ApJ*, *142*, 1633–1636.

Halzen, F., & Kheirandish, A. (2016). High-energy Neutrinos from Recent Blazar Flares. *ApJ*, *831*, 12.

Harrison, F. A., Craig, W. W., Christensen, F. E., Hailey, C. J., Zhang, W. W., Boggs, S. E., Stern, D., Cook, W. R., Forster, K., Giommi, P., et al. (2013). The nuclear spectroscopic telescope array (NuSTAR) high-energy X-ray mission. *ApJ*, *770*, 103.

Hazard, C., Mackey, M. B., & Shimmins, A. J. (1963). Investigation of the Radio Source 3C 273 By The Method of Lunar Occultations. *Nature*, *197*, 1037–1039.

Helmboldt, J., Taylor, G., Tremblay, S., Fassnacht, C., Walker, R., Myers, S., Sjouwerman, L., Pearson, T., Readhead, A., Weintraub, L., et al. (2007). The VLBA imaging and polarimetry survey at 5 GHz. *ApJ*, *658*, 203.

Hogg, D. W., Bovy, J., & Lang, D. (2010). Data analysis recipes: Fitting a model to data. *arXiv:1008.4686*.

Hoyle, F., & Fowler, W. A. (1963). Nature of strong radio sources. *Nature*, *197*, 533–535.

IceCube Collaboration. (2013). Evidence for high-energy extraterrestrial neutrinos at the icecube detector. *Science*, *342*, 1242856.

Jackson, J. D. (1977). *Classical electrodynamics*. Wiley New York.

James, F., & Roos, M. (1975). MINUIT: a system for function minimization and analysis of the parameter errors and corrections. *Comput. Phys. Commun.*, *10*, 343–367.

Jansen, F., Lumb, D., Altieri, B., Clavel, J., Ehle, M., Erd, C., Gabriel, C., Guainazzi, M., Gondoin, P., Much, R., et al. (2001). XMM-Newton observatory. *A & A*, *365*, L1–L6.

Jarrett, T., Cohen, M., Masci, F., Wright, E., Stern, D., Benford, D., Blain, A., Carey, S., Cutri, R., Eisenhardt, P., et al. (2011). The Spitzer–WISE Survey of the Ecliptic Poles. *ApJ*, *735*, 112.

Johnson, J. L., Whalen, D. J., Li, H., & Holz, D. E. (2013). Supermassive seeds for supermassive black holes. *Apj*, *771*, 116.

Jones, F. C. (1968). Calculated Spectrum of Inverse-Compton-Scattered Photons. *APS*, *167*, 1159–1169.

Kaspi, S., Brandt, W., Maoz, D., Netzer, H., Schneider, D. P., & Shemmer, O. (2007). Reverberation mapping of high-luminosity quasars: First results. *ApJ*, *659*, 997.

Kazanas, D., & Mastichiadis, A. (1999). Relativistic electrons in blazars: A hadronic origin? *ApJ*, *518*, L17.

Komberg, B. V., & Charugin, V. M. (1969). X-Ray Emission from Radio Galaxies and Quasars. *SvA*, *12*, 737.

Latif, M., & Schleicher, D. (2015). The formation of supermassive black holes in rapidly rotating disks. *A&A*, *578*, A118.

Latif, M. A., & Ferrara, A. (2016). Formation of supermassive black hole seeds. *PASA*, *33*, e051.

Li, S., Xia, Z.-Q., Liang, Y.-F., Liao, N.-H., & Fan, Y.-Z. (2018). Fast γ-Ray Variability in Blazars beyond Redshift 3. *ApJ*, *853*, 159–170.

Liu, Y., & Zhang, S. N. (2011). Dusty torus formation by anisotropic radiative pressure feedback of active galactic nuclei. *ApJ Letters*, *728*, L44.

Longair, M. S. (2011). *High energy astrophysics*. Cambridge University Press.

Lynden-Bell, D. (1969). Galactic nuclei as collapsed old quasars. *Nature*, *223*, 690–694.

MacKay, D. J. (2003). *Information theory, inference and learning algorithms* [Version 7.2]. Cambridge university press.

Madau, P., Haardt, F., & Dotti, M. (2014). Super-critical growth of massive black holes from stellar-mass seeds. *ApJ Letters*, *784*, L38.

Mannheim, K., & Biermann, P. (1989). Photomeson production in active galactic nuclei. *A&A*, *221*, 211–220.

Mannheim, K., & Biermann, P. (1992). Gamma-ray flaring of 3C 279-A proton-initiated cascade in the jet? *A&A*, *253*, L21–L24.

Mannheim, K. (1993). The proton blazar. *A&A*, *269*, 67–76.

Maraschi, L., Ghisellini, G., & Celotti, A. (1992). A jet model for the gamma-ray emitting blazar 3C 279. *ApJ*, *397*, L5–L9.

Maraschi, L., Grandi, P., Urry, C., Wehrle, A., Madejski, G., Fink, H., Ghisellini, G., Hartman, R., Koratkar, A., Von Montigny, C., et al. (1994). The 1993 multiwavelength campaign on 3C 279: The radio to gamma-ray energy distribution inlow state. *ApJ Letters*, *435*, L91–L95.

Maraschi, L., & Tavecchio, F. (2003). The jet-disk connection and blazar unification. *ApJ*, *593*, 667.

Marscher, A. P. (2016). Variability of Blazars and Blazar Models over 38 Years. *Galaxies*, *4*, 37.

Marscher, A. P., & Gear, W. K. (1985). Models for high-frequency radio outbursts in extragalactic sources, with application to the early 1983 millimeter-to-infrared flare of 3C 273. *ApJ*, *298*, 114–127.

Massaro, E., Perri, M., Giommi, P., Nesci, R., & Verrecchia, F. (2004). Log-parabolic spectra and particle acceleration in blazars. II. The BeppoSAX wide band X-ray spectra of Mkn 501. *A&A*, *422*, 103–111.

Massaro, E., Tramacere, A., Perri, M., Giommi, P., & Tosti, G. (2006). Log-parabolic spectra and particle acceleration in blazars. III. SSC emission in the TeV band from Mkn501. *A&A*, *448*, 861–871.

Massaro, F., & D'Abrusco, R. (2016). The infrared–gamma-ray connection: a WISE View of the Extragalactic Gamma-ray Sky. *ApJ*, *827*, 67.

Mastichiadis, A., & Kirk, J. G. (1996). Variability in the synchrotron self-Compton model of blazar emission. *A&A*, *320*, 19–25.

Mücke, A., & Protheroe, R. (2000). GeV-TeV Gamma Ray Astrophysics Workshop. *AIP Conf. Proc*, *515*, 149.

Natarajan, P., Pacucci, F., Ferrara, A., Agarwal, B., Ricarte, A., Zackrisson, E., & Cappelluti, N. (2017). Unveiling the first black holes with JWST: multi-wavelength spectral predictions. *ApJ*, *838*, 117.

Natarajan, P., Pacucci, F., Ricarte, A., Bogdan, A., Goulding, A. D., & Cappelluti, N. (2023). First Detection of an Over-Massive Black Hole Galaxy: UHZ1–Evidence for Heavy Black Hole Seeds From Direct Collapse? *arXiv:2308.02654*.

Nemmen, R. S., Georganopoulos, M., Guiriec, S., Meyer, E. T., Gehrels, N., & Sambruna, R. M. (2012). A universal scaling for the energetics of relativistic jets from black hole systems. *Science*, *338*, 1445–1448.

Oke, J. B. (1963). Absolute Energy Distribution in the Optical Spectrum of 3C 273. *Nature*, *197*, 1040–1041.

Padovani, P., Giommi, P., & Rau, A. (2012). The discovery of high-power high synchrotron peak blazars. *MNRAS Letters*, *422*, L48–L52.

Padovani, P., Perlman, E. S., Landt, H., Giommi, P., & Perri, M. (2003). What types of jets does nature make? a new population of radio quasars. *ApJ*, *588*, 128.

Paliya, V. S., Ajello, M., Cao, H.-M., Giroletti, M., Kaur, A., Madejski, G., Lott, B., & Hartmann, D. (2020). Blazars at the cosmic dawn. *ApJ*, *897*, 177.

Paliya, V. S., Cheung, C., Kocevski, D., & Angioni, R. (2018). Fermi-LAT detection of high gamma-ray activity from the $z = 3.6$ quasar NVSS J163547+ 362930. *The Astronomer's Telegram*, *11847*, 1.

Paliya, V. S., Parker, M., Fabian, A., & Stalin, C. (2016). Broadband observations of high redshift blazars. *ApJ*, *825*, 74.

Pâris et al. (2018). The Sloan Digital Sky Survey quasar catalog: fourteenth data release. *A&A*, *613*, A51.

Peterson, B. M. (1993). Reverberation mapping of active galactic nuclei. *PASP*, *105*, 247.

Petri, A., Ferrara, A., & Salvaterra, R. (2012). Supermassive black hole ancestors. *MNRAS*, *422*, 1690–1699.

Petrov, L., & Taylor, G. (2011). Precise absolute astrometry from the VLBA imaging and polarimetry survey at 5 GHz. *ApJ*, *142*, 89.

Planck Collaboration. (2016). Planck 2015 Results-XIII. Cosmological parameters. *A&A*, *594*, A13.

Plavin, A., Kovalev, Y., & Petrov, L. Y. (2019). Dissecting the AGN disk–Jet system with joint VLBI-Gaia analysis. *ApJ*, *871*, 143.

Plotkin, R. M., Anderson, S. F., Brandt, W., Markoff, S., Shemmer, O., & Wu, J. (2012). The lack of torus emission from BL Lacertae objects: An infrared view of unification with WISE. *ApJ Letters*, *745*, L27.

Poole, T., Breeveld, A., Page, M., Landsman, W., Holland, S., Roming, P., Kuin, N., Brown, P., Gronwall, C., Hunsberger, S., et al. (2008). Photometric calibration of the Swift Ultraviolet-Optical telescope. *MNRAS*, *383*, 627–645.

Prandini, E., & Ghisellini, G. (2022). The blazar sequence and its physical understanding. *Galaxies*, *10*, 35.

Prusti, T., De Bruijne, J., Brown, A. G., Vallenari, A., Babusiaux, C., Bailer-Jones, C., Bastian, U., Biermann, M., Evans, D. W., Eyer, L., et al. (2016). The gaia mission. *A&A*, *595*, A1.

Pudritz, R. E., Hardcastle, M. J., & Gabuzda, D. C. (2012). Magnetic fields in astrophysical jets: From launch to termination. *Space Sci. Rev.*, *169*, 27–72.

Rau, A., Schady, P., Greiner, J., Salvato, M., Ajello, M., Bottacini, E., Gehrels, N., Afonso, P., Elliott, J., Filgas, R., et al. (2012). BL Lacertae objects beyond redshift 1.3–UV-to-NIR photometry and photometric redshift for Fermi/LAT blazars. *A & A*, *538*, A26.

Rawlings, S., & Saunders, R. (1991). Evidence for a common central-engine mechanism in all extragalactic radio sources. *Nature*, *349*, 138–140.

Rees, M. J. (1978). Quasars. *The Observatory*, *98*, 210–223.

Rieger, F. M., & Duffy, P. (2004). Shear acceleration in relativistic astrophysical jets. *ApJ*, *617*, 155.

Roming, P. W., Kennedy, T. E., Mason, K. O., Nousek, J. A., Ahr, L., Bingham, R. E., Broos, P. S., Carter, M. J., Hancock, B. K., Huckle, H. E., et al. (2005). The Swift ultra-violet/optical telescope. *Space Sci. Rev.*, *120*, 95–142.

Rybicki, G. B., & Lightman, A. P. (1991). *Radiative processes in astrophysics*. John Wiley & Sons.

Sahakyan, N., Israyelyan, D., Harutyunyan, G., Khachatryan, M., & Gasparyan, S. (2020). Multiwavelength study of high-redshift blazars. *MNRAS*, *498*, 2594–2613.

Sawicki, M. (2012). SEDfit: Software for spectral energy distribution fitting of photometric data. *PASP*, *124*, 1208.

Scarpa, R., & Falomo, R. (1997). Are high polarization quasars and BL Lacertae objects really different? A study of the optical spectral properties. *A&A*, *325*, 109–123.

Schlegel, D. J., Finkbeiner, D. P., & Davis, M. (1998). Maps of dust infrared emission for use in estimation of reddening and cosmic microwave background radiation foregrounds. *ApJ*, *500*, 525.

Schmidt, M. (1963). 3C 273 : A Star-Like Object with Large Red-Shift. *Nature*, *197*, 1040.

Shakura, N. I., & Sunyaev, R. A. (1973). Black holes in binary systems. Observational appearance. *A&A*, *24*, 337–355.

Shapiro, S. L. (2005). Spin, accretion, and the cosmological growth of supermassive black holes. *ApJ*, *620*, 59.

Sikora, M., Begelman, M. C., Madejski, G. M., & Lasota, J.-P. (2005). Are quasar jets dominated by poynting flux? *ApJ*, *625*, 72.

Sikora, M., Begelman, M. C., & Rees, M. J. (1994). Comptonization of diffuse ambient radiation by a relativistic jet: The source of gamma rays from blazars? *ApJ*, *421*, 153–162.

Sokolov, A., Marscher, A. P., & McHardy, I. M. (2004). Synchrotron self-compton model for rapid nonthermal flares in blazars with frequency-dependent time lags. *ApJ*, *613*, 725.

Spada, M., Ghisellini, G., Lazzati, D., & Celotti, A. (2001). Internal shocks in the jets of radio-loud quasars. *MNRAS*, *325*, 1559–1570.

Stecker, F., De Jager, O., & Salamon, M. (1992). TeV gamma rays from 3C 279-A possible probe of origin and intergalactic infrared radiation fields. *ApJ*, *390*, L49–L52.

Stickel, M., Padovani, P., Urry, C., Fried, J., & Kuehr, H. (1991). The complete sample of 1 Jansky BL Lacertae objects. I-Summary properties. *ApJ*, *374*, 431–439.

Tanaka, T., & Haiman, Z. (2009). The assembly of supermassive black holes at high redshifts. *ApJ*, *696*, 1798.

Tavecchio, F., Maraschi, L., Pian, E., Chiappetti, L., Celotti, A., Fossati, G., Ghisellini, G., Palazzi, E., Raiteri, C., Sambruna, R., et al. (2001). Theoretical implications from the spectral evolution of Markarian 501 observed with BeppoSAX. *ApJ*, *554*, 725.

Tavecchio, F., Ghisellini, G., & Guetta, D. (2014). Structured jets in BL Lac objects: efficient PeV neutrino factories? *ApJ*, *793*, L18.

Tavecchio, F., Maraschi, L., Sambruna, R. M., & Urry, C. M. (2000). The X-ray jet of PKS 0637–752: inverse compton radiation from the cosmic microwave background? *ApJ*, *544*, L23.

Thorne, K. S. (1974). Disk-accretion onto a black hole. II. Evolution of the hole. *ApJ*, *191*, 507–520.

Tramacere, A., Giommi, P., Perri, M., Verrecchia, F., & Tosti, G. (2009). Swift observations of the very intense flaring activity of Mrk 421 during 2006. I. Phenomenological picture of electron acceleration and predictions for MeV/GeV emission. *A&A*, *501*, 879–898.

Tramacere, A. (2020). JetSeT: Numerical modeling and SED fitting tool for relativistic jets. *ASCL*, ascl–2009.

Tramacere, A., Massaro, E., & Taylor, A. (2011). Stochastic acceleration and the evolution of spectral distributions in synchro-self-compton sources: A self-consistent modeling of blazars'flares. *ApJ*, *739*, 66.

Tramacere, A., Sliusar, V., Walter, R., Jurysek, J., & Balbo, M. (2022). Radio-γ-ray response in blazars as a signature of adiabatic blob expansion. *A & A*, *658*, A173.

Urry, C. M., & Padovani, P. (1995). Unified Schemes for Radio-Loud Active Galactic Nuclei. *PASP*, *107*, 803–845.

Vallenari, A., Brown, A., Prusti, T., de Bruijne, J., Arenou, F., Babusiaux, C., Biermann, M., Creevey, O., Ducourant, C., Evans, D., et al. (2023). Gaia data release 3-summary of the content and survey properties. *A&A*, *674*.

Vestergaard, M., & Peterson, B. M. (2006). Determining central black hole masses in distant active galaxies and quasars. II. Improved optical and UV scaling relationships. *ApJ*, *641*, 689.

Volonteri, M. (2010). Formation of supermassive black holes. *A&A Rev.*, *18*, 279–315.

Volonteri, M. (2012). The formation and evolution of massive black holes. *Science*, *337*, 544–547.

Wang, F., Yang, J., Fan, X., Hennawi, J. F., Barth, A. J., Banados, E., Bian, F., Boutsia, K., Connor, T., Davies, F. B., et al. (2021). A luminous quasar at redshift 7.642. *ApJ Letters*, *907*, L1.

Weidinger, M., Rüger, M., & Spanier, F. (2010). Modelling the steady state spectral energy distribution of the BL-Lac Object PKS 2155-304 using a selfconsistent SSC model. *Astrophys. Space Sci. Trans.*, *6*, 8.

White, R. L., & Becker, R. H. (1992). A new catalog of 30,239 1.4 GHz sources. *ApJ Supplement Series*, *79*, 331–467.

Wright, E. L. (2006). A cosmology calculator for the world wide web. *PASP*, *118*, 1711.

Wright, E. L., Eisenhardt, P. R., Mainzer, A. K., Ressler, M. E., Cutri, R. M., Jarrett, T., Kirkpatrick, J. D., Padgett, D., McMillan, R. S., Skrutskie, M., et al. (2010). The Wide-field Infrared Survey Explorer (WISE): mission description and initial on-orbit performance. *ApJ*, *140*, 1868.

Zeng, H., Petrosian, V., & Yi, T. (2021). Cosmological evolution of fermi large area telescope gamma-ray blazars using novel nonparametric methods. *ApJ*, *913*, 120.

Zhang, J., Sun, X.-N., Liang, E.-W., Lu, R.-J., Lu, Y., & Zhang, S.-N. (2014). Relativistic Jet Properties Of Gev–Tev Blazars And Possible Implications For The Jet Formation, Composition, And Cavity Kinematics. *ApJ*, *788*, 104.

Zheng, Y., Yang, C., & Kang, S. (2016). Bethe-Heitler cascades as a plausible origin of hard spectra in distant TeV blazars. *A&A*, *585*, A8.

Agradecimientos

Vorrei innanzitutto esprimere la mia gratitudine ai miei supervisori, poiché questo progetto non sarebbe stato possibile senza la loro supervisione. Vorrei riconoscere la guida e l'attenzione fornite dal mio supervisore Prof. Bottacini. Desidero inoltre ringraziare il co-supervisore di questo lavoro, Dr. Tramacere. Sono grato per tutti i suoi commenti, per le domande a cui mi ha aiutato a rispondere e per la sua costante attenzione al mio lavoro. Grazie di cuore

También deseo expresar mi profundo agradecimiento al lector, sin importar si ha leído todo el texto o no. El hecho de que estés leyendo estas palabras indica que eres un amigo en quien confío plenamente y que ha jugado un papel crucial a lo largo de estos dos años de estudio y aprendizaje. No puedo agradecer lo suficiente por todo el apoyo y cariño que me has brindado. En especial, quiero mencionar y agradecer a aquellos con quienes compartí momentos de alegría y lágrimas durante los exámenes: Ruth, Anny, Jessie, Irma, Mahmoud, Niccolo, Francesco; con quienes compartí mi hogar: Alessandro, Gabrinho, Emilio, Alessio, Mateo, Gainluca, Michelle, Chiwa; y a mis compatriotas: Freddy, Andrea, Esteban y Javier. A todos ustedes, muchas gracias.

Quiero también agradecer a mi familia por todo el respaldo y cariño que me brindaron a lo largo de este programa, sobre todo considerando el kilometraje de dsitancia que nos separaba. Simplemente sin ustedes no hubiera terminado este trabajo. Gracias por todo el apoyo, consuelo, amor y cariño que me brindan incondiscionalmente; los quiero mucho.

Manifiesto mi profunda gratitud hacia la Universidad de Padua, la provincia de Padua, la región del Veneto, el gobierno italiano y a cada uno de sus ciudadanos. Italia, indudablemente, será un hito imborrable en mi carrera y en mi vida.

Egli è scritto in lingua matematica, e i caratteri son triangoli, cerchi, ed altre figure Geometriche, senza i quali mezi è impossibile a intenderne vmanamente parola; senza questi è vn'aggirarsi vanamente per vn'oscuro laberinto.

(G. Galilei, *Il Saggiatore*)